

Linköping Studies in Science and Technology. Theses.
No. 993

Computation of Thermal Development in Injection Mould Filling, based on the Distance Model

Per-Åke Andersson



INSTITUTE OF TECHNOLOGY
LINKÖPINGS UNIVERSITET

Department of Mathematics
Linköpings universitet, SE-581 83 Linköping, Sweden

Linköping 2002

**Computation of Thermal Development in Injection Mould Filling,
based on the Distance Model**

© 2002 Per-Åke Andersson

Matematiska institutionen
Linköpings universitet
SE-581 83 Linköping, Sweden
peand@mai.liu.se

LiU-TEK-LIC-2002:66
ISBN 91-7373-563-9
ISSN 0280-7971

Printed by UniTryck, Linköping 2002

Contents

	Abstract	v
	Acknowledgements	vi
1	Introduction	1
1.1	<i>Purpose and limitations</i>	1
1.2	<i>Method principles</i>	2
1.3	<i>Structure of the thesis</i>	4
2	Injection moulding and temperature modelling	5
2.1	<i>Modes of heat transfer</i>	5
2.2	<i>Temperature dependent material properties</i>	6
2.2.1	Heat capacity and latent heat	6
2.2.2	Density and thermal conductivity	7
2.2.3	Viscosity	8
2.2.4	Dimensionless groups and asymptotic temperature profiles	9
2.2.5	Assumptions	10
2.3	<i>The governing equations</i>	11
2.3.1	General notation	11
2.3.2	Mass and momentum balance	11
2.3.3	Energy balance	13
2.4	<i>Boundary conditions</i>	13
2.4.1	Symmetry, points of injection and mould walls	13
2.4.2	Flow front	14
3	Model and method	15
3.1	<i>Analytical sub-models</i>	15
3.1.1	Vertical velocity profile	15
3.1.2	Pressure distribution	17
3.1.3	Freezing layer	18
3.1.4	Fountain flow	20
3.2	<i>PDEs and solution method</i>	22
3.2.1	General and regional melt PDEs	22
3.2.2	Time marching and pseudo-radial marching	25
3.2.3	Outer iteration: Surface of frozen layer	25
3.2.4	Inner iteration: Vertical temperature profile	26
3.2.5	Cooling PDE and its series solution	27
	Flowchart 3.1 Data processing	30
	Flowchart 3.2 Solution routine for active flow. Radial symmetry	31
	Flowchart 3.3 Solution routine for passive flow	31
3.3	<i>FD scheme</i>	32
3.3.1	Control volume approach and truncation error	32
3.3.2	Convergence of inner iterations	37

4	Application: Circular plate	41
4.1	<i>Special modelling: Radial flow</i>	41
4.2	<i>Materials data</i>	42
4.3	<i>Comparison runs</i>	45
4.3.1	Pressure distribution	45
4.3.2	Temperature distribution	47
4.4	<i>Variation of physical model</i>	53
4.4.1	Latent heat of crystallization	53
4.4.2	Heat conductivity	53
4.4.3	Viscosity dependence of pressure	53
4.5	<i>Method performance</i>	55
4.5.1	Relations to the number of vertical levels (control volumes)	55
4.5.2	Wall series solution	56
4.5.3	Control volume at the frozen layer	56
5	Application: Triangular plate	59
5.1	<i>Special modelling: Geometry</i>	59
5.2	<i>Materials data</i>	61
5.3	<i>Comparison runs</i>	63
5.3.1	Average temperature	63
5.3.2	Temperature profiles	71
5.4	<i>Method performance</i>	72
5.4.1	Square-root parameter	72
5.4.2	Iteration statistics	72
5.4.3	Velocity profiles and residence time	72
6	Conclusions	75
7	References	77
Appendix 1	Vertical velocity profiles	79
Appendix 2	Further comments on the Stefan problem	80
A2.1	<i>Freezing layer in the presence of particular heat generation</i>	80
A2.2	<i>Initial front temperatures by the square-root model</i>	82
Appendix 3	Solid melt: a series solution	83
Appendix 4	Comments on the PDE and its well-posedness	85
Appendix 5	Stability of linearized FD scheme	87

Abstract

The heat transfer in the filling phase of injection moulding is studied, based on Gunnar Aronsson's distance model for flow expansion ([Aronsson], 1996).

The choice of a thermoplastic materials model is motivated by general physical properties, admitting temperature and pressure dependence. Two-phase, per-phase-incompressible, power-law fluids are considered. The shear rate expression takes into account pseudo-radial flow from a point inlet.

Instead of using a finite element (FEM) solver for the momentum equations a general analytical viscosity expression is used, adjusted to current axial temperature profiles and yielding expressions for axial velocity profile, pressure distribution, frozen layer expansion and special front convection.

The nonlinear energy partial differential equation is transformed into its conservative form, expressed by the internal energy, and is solved differently in the regions of streaming and stagnant flow, respectively. A finite difference (FD) scheme is chosen using control volume discretization to keep truncation errors small in the presence of non-uniform axial node spacing. Time and pseudo-radial marching is used. A local system of nonlinear FD equations is solved. In an outer iterative procedure the position of the boundary between the "solid" and "liquid" fluid cavity parts is determined. The uniqueness of the solution is claimed. In an inner iterative procedure the axial node temperatures are found. For all physically realistic material properties the convergence is proved. In particular the assumptions needed for the Newton-Mysovskii theorem are secured. The metal mould PDE is locally solved by a series expansion. For particular material properties the same technique can be applied to the "solid" fluid.

In the circular plate application, comparisons with the commercial FEM-FD program Moldflow (Mfl) are made, on two Mfl-database materials, for which model parameters are estimated/adjusted. The resulting time evolutions of pressures and temperatures are analysed, as well as the radial and axial profiles of temperature and frozen layer. The greatest differences occur at the flow front, where Mfl neglects axial heat convection. The effects of using more and more complex material models are also investigated. Our method performance is reported.

In the polygonal star-shaped plate application a geometric cavity model is developed. Comparison runs with the commercial FEM-FD program Cadmould (Cmd) are performed, on two Cmd-database materials, in an equilateral triangular mould cavity, and materials model parameters are estimated/adjusted. The resulting average temperatures at the end of filling are compared, on rays of different angular deviation from the closest corner ray and on different concentric circles, using angular and axial (cavity-halves) symmetry. The greatest differences occur in narrow flow sectors, fatal for our 2D model for a material with non-realistic viscosity model. We present some colour plots, e.g. for the residence time.

The classical square-root increase by time of the frozen layer is used for extrapolation. It may also be part of the front model in the initial collision with the cold metal mould. An extension of the model is found which describes the radial profile of the frozen layer in the circular plate application accurately also close to the inlet.

The well-posedness of the corresponding linearized problem is studied, as well as the stability of the linearized FD-scheme.

Acknowledgements

I am most grateful to the Swedish Council of Science, the Department of Mathematics at Linköping University, especially my supervisor professor Gunnar Aronsson and the Section of Applied Mathematics, and the Departments of Technology and Science at Örebro University, especially the Section of Mathematics (where I am a member of staff), for their confidence by awarding me, a "55+", the privilege of education and research, and for financially and morally supporting me.

I respectfully acknowledge the unsponsored work performed by Mari Valtonen, Tampere University of Technology, and Lars-Åke Nilsson, PolyInvent AB, on FEM-FD simulation runs.

I express my sincere gratitude to Tommy Elfving and Gunnar Aronsson for many valuable comments on my writing.

I am much obliged to Lena.

1 Introduction

1.1 Purpose and limitations

One of the main reasons for studying temperature in injection moulding is the need for judging the risk of such local freezing that may lead to an incomplete filling of the mould cavity. The typical cavity domain is characterized by a small extension in one – gap – direction, i.e. the filling is “essentially” a 2D process.

In commercial FEM-FD (finite elements method, finite differences) programs the expansion flow and the temperature of the molten plastic are computed simultaneously.

This thesis is based upon the distance model, which asymptotically (i.e. for power-law fluids of small index values, see [Aronsson]) describes how a polymer melt expands from an injection point and fills the mould cavity, without consideration of temperatures. Our separate temperature model becomes a consistency check, and may also act as a correction tool, if necessary.

The study is limited to the filling of the mould cavity. This means that the packing and cooling phases of the process are omitted, and the varying influence of the inlet and cooling channels on temperatures is ignored.

The cooling phase of the process gives the main reduction of temperatures, by 100 °C or more during several tens of seconds. The objective for considering the shorter filling phase – of magnitude 1-3 seconds – becomes e.g. to correctly identify situations where local freezing of streaming fluid exceeds some critical limit, e.g. a prescribed proportion of the mould gap at some mould positions, rather than to accurately describe the temperature distribution over the gap or even the average temperature. Temperature effects can also be crucial for warpage, poor welds (flow marks), burning, brittleness and parts flashing ([Becker et al.], p.203, and [Berins], p.161).

The flow front velocities that are generated by the distance model, combined with a simple viscosity based model, act as inputs to an energy equation; which makes the temperature computation much simpler than when coupled with the traditional Navier-Stokes equations. However, there is a need for additional assumptions:

- the local flow direction is steady,
- the pseudo-circles, that describe the flow front expansion (see [Aronsson], p.428), define isobars until local stagnation,
- the cavity parts that share flow history are equivalent as to temperature evolution.

The general aim for the temperature model and its computational method is to match the simplicity of the distance model and the fastness of the corresponding shortest route method, hopefully making a later integration possible.

For comparison purposes several materials are studied, with data easily available and chosen to reflect different properties of viscosity and latent heat.

1.2 Method principles

The work is theoretical and no practical evaluation on real moulding data has been performed. The developed computer program is basically a numerical FD scheme, and simulation comparisons are made with two commercial FEM-FD programs.

To be strictly consistent with the assumptions of the distance model, the fluid viscosity should be independent of temperature – the isothermal case. In the standalone FD program this is a special case of a more general material model.

The FD simulations are performed on a PC computer, using C++ for computational purposes and Matlab (® The MathWorks, Inc.) for graphics.

1.2 Method principles

We consider two kinds of applications: disk- and polygonal star-shaped cavities, with one “point” of injection. Our simplifying assumption is that the main flow is radial, an “essentially” 1D process, i.e. that any angular flow and heat exchange can be neglected. During the filling phase of a triangular cavity the flow situation may look like in **Figure 1.1a**.

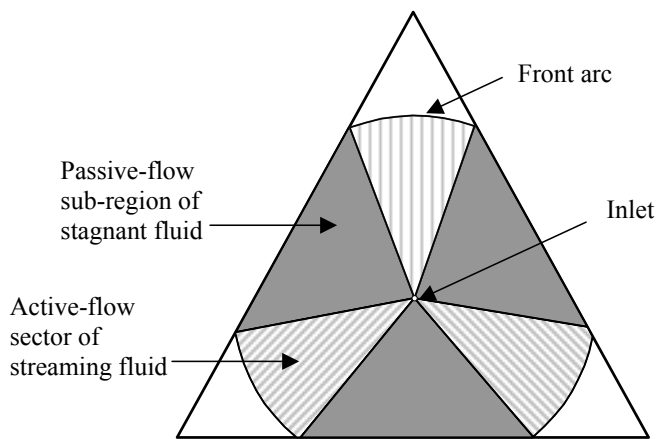


Figure 1.1 a Regions of streaming and stagnant fluid during filling. Radial flow.

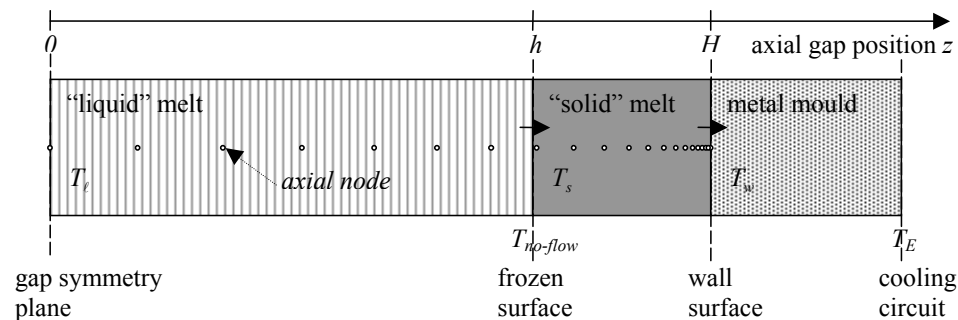


Figure 1.1 b Computational quantities in axial section, for given radial and angular position.

In **Fig. 1.1a** we identify three active-flow sectors (sub-regions), with one circular front arc each, and three passive-flow sub-regions. These two types of regions are handled separately:

- In the active-flow sub-regions the resulting PDE is solved by time-marching, i.e. we discretize the time from start to end of the filling phase in discrete time steps $k = 1, \dots, K$. For each time step k we practice radial marching in radial steps $i = 1, \dots, k$ from inlet to front, i.e. we approximate the PDE by a system of FD equations for the current temperature distribution at (k, i) . Because of the radial symmetry, all nodes that are concentrically placed relative to the inlet (common i) share flow history and are treated as one common node group. In both the disk- and polygonal star-shaped applications one ray of maximum length, i.e. an arbitrary disk ray and one polygonal corner ray, respectively, is sufficient to characterize the whole active-flow process.
- In the passive-flow sub-regions we have to distinguish more node groups, since **Fig. 1.1a** shows that both the radial position and the time of stagnation, i.e. when the flow hits the wall along the stream ray through the node, have to coincide to define equivalent flow history. For each node group i of common flow history we perform time-marching by steps k from the time of stagnation to the end of filling. The start temperatures of the stagnant ray in focus are received from the active-flow evolution, the snapshot taken at the time of ray stagnation (wall hit).

The solution method is the same in both types of flow regions, for every given time step k and node group i . In **Figure 1.1b** the basic symbols are shown. The gap-wise direction z is drawn from the centre symmetry plane $z = 0$ to the nominal wall surface $z = H$. The local effective gap width h , that separates streaming fluid from “frozen” melt, is defined by the no-flow temperature $T_{no-flow}$. In each phase of state, “liquid” and “solid”, a system of nonlinear FD-equations is solved for the temperatures T_ℓ, T_s at the given axial node positions z_j , $j = 0, 1, \dots, J$ (with $J = 20$ in **Fig. 1.1b**). This is made in an inner iterative procedure for fixed h , primarily by the damped Newton-Raphson method. The correct local position of h is determined in an outer iterative procedure, taking into account the heat flow between the two melt phases. The interaction with the metal mould is managed by a series expansion solution for the wall temperatures T_w , reducing the computation of local heat exchange mould - cavity to a mere analytical updating. Our strategy involves solving two small systems of altogether $J+1$ nonlinear FD-equations many times, once for each trial h -value of each (k, i) -combination. The axial node positions are chosen to balance two conflicting aims: capturing the steep temperature change at the frozen layer and reducing the truncation errors.

1.3 Structure of the thesis

In **Chapter 2** we describe the major elements of our temperature model for the filling phase of injection moulding – the modes of heat transfer, the relevant materials properties, and the basic model assumptions, equations and boundary conditions.

In **Chapter 3** our model and method are presented, for (pseudo-)radial expansion flow. The basic energy model is extended by some analytical submodels – one replacing the absent pressure-momentum equations, one extrapolating the expansion of the frozen layer, and two variants handling the flow front energy. A numerical FD-scheme and a positioning principle for the axial nodes are derived. The general method (cf. **Sec. 1.2**) is fully described and its expected behaviour is analysed.

Our method is implemented for two different applications. The first type, studied in **Ch. 4**, is disk shaped cavities. Two commodity materials, an amorphous polycarbonate (PC) and a semi-crystalline polyethylene (HDPE) are modelled. Four comparison simulation runs of the FEM-FD-program Moldflow (of Moldflow Corp.) and our FD-program are evaluated. The influence of our more extended material models upon the resulting temperature and frozen layer profiles is studied. Some aspects of our method performance are documented.

In **Ch. 5** we treat the second application type, polygonal star-shaped cavities (relative to the inlet), of constant gap width (cf. **Fig. 1.1a**). The special geometry modelling is described. Two commodity thermoplastics, an amorphous polystyrene (PS) and a semi-crystalline polyoxymethylene (POM), are studied. Two, out of four intended, comparison simulation runs of the FEM-FD-program Cadmould (of Simcon) and our FD-program are documented. Apart from the comparison figures, some of our internal FD-model and method results are reported, partly as colour plots. These include the calculated times of injection.

Our main conclusions are presented in **Ch. 6**.

In **Appendices 1 – 5** some results related to the implemented routine are collected. We give examples from the assumed class of velocity profiles and the corresponding temperature profiles, derive a class of square-root solutions characterizing the expansion of the frozen layer in radial flow, present a series expansion solution for the temperatures in the frozen sub-regions, and treat the well-posedness of the linearized PDE as well as the stability of the linearized FD-scheme for given frozen layer profiles.

2 Injection moulding and temperature modelling

In this chapter we describe the basic elements of our temperature model for the filling phase of injection moulding. The conductive and convective heat transfer modes are identified in **Sec. 2.1**. By using the practical concept of a no-flow temperature, which subdivides the fluid into an essentially immobile (“solid”, “frozen”) and a mobile (“liquid”) phase of state, we can treat both semi-crystalline thermoplastics and amorphous materials in **Sec. 2.2**. For the main material properties – heat capacity, latent heat of crystallization, density, heat conductivity and viscosity – we judge whether constant or simple linear or nonlinear functions of temperature and/or pressure are needed to capture the main variations. We argue that the non-asymptotic character and the dynamics of the filling process would make a model based upon dimensionless quantities, like the Cameron number, of less value. In **Sec. 2.3** the underlying assumptions of the distance model, for flow expansion and pressure field, are listed. The basic equations are formulated, with focus on the energy PDE. Due to the temperature dependent fluid properties, the energy equation becomes nonlinear. A temperature dependent viscosity makes the momentum/pressure field equations depend upon the temperature solution of the energy PDE, while shear rate, convection velocity and pressure provide a link in the opposite direction. Finally in **Sec. 2.4** the boundary conditions are listed. The special difficulties of the moving flow front are noticed.

2.1 Modes of heat transfer

From an inlet “point” (gate) where the thermoplastic is injected into the mould cavity, the expansion of the hot polymer melt means a thermal convection that is essentially radial. In the filled cavity parts heat is transferred by conduction mainly in the gap-wise (z -)direction to the metallic walls, where cooling channels transport heat out of the mould.

Near the cavity walls streaming melt is subject to high shear rates, which tends to increase the temperature through viscous dissipation. A frozen layer of cooled, stagnant melt is built up at the walls, to some extent acting as an insulation layer between the streaming fluid and the cold walls.

Since most polymers are non-opaque to infrared light, some radiation energy hits the metallic wall surface.

In the absence of sharp cavity corners, laminar flow dominates the filling process except at the flow front, where heat is transferred straight to the walls by convection across the gap. The corresponding orientation of the polymer chains – normal at the very wall surface and tangential in the laminar zone (see, e.g., [Tadmor & Gogos], p.608) – affects conduction.

For the filling phase, the fluid properties normally identify one temperature of dramatic changes, the practical concept $T_{no-flow}$. (In **Sec. 2.2** it can be identified as T_M or T_G .)

2.2 Temperature dependent material properties

2.2.1 Heat capacity and latent heat

In a process where the material density ρ is almost fixed, the constant-pressure heat capacity c_p nearly coincides with the constant-volume heat capacity (the difference is around 10% for polymers, see [Rao], p.37). For amorphous polymers, c_p increases continuously and slowly with increasing temperature except at a point of discontinuity – the glass transition temperature T_G – where the polymer from a colder glassy state becomes more easily deformable – rubbery – and the c_p -curve has a step-up jump.

For semi-crystalline polymers, ordered crystalline regions are surrounded by a matrix of less ordered, rubbery amorphous material, making the polymer tough and leathery above T_G , and brittle through a glassy amorphous matrix below T_G ([Morton-Jones], p.14). At the temperature where the crystalline structure is lost, the c_p -curve shows a narrow peak, where the position of the maximum defines the melting point T_M . By cooling such a material the latent heat of solidification (crystallisation) L_M is released. Realistic modelling is complicated by such phenomena as sub-cooling and slow crystallisation.

For practical purposes, c_p can be considered as pressure independent ([Tadmor & Gogos], p.139).

As for the physical state of injection moulded thermoplastics at room temperature, PP, HDPE and POM are semi-crystalline between T_G and T_M , and PA 6 is below T_G , while the materials ABS, PVC, PMMA, PC and PS are examples of amorphous polymers below T_G (e.g. [Becker et al.], p.20).

When data are unavailable, [Van Krevelen], p.116 recommends the following linear, empirical expressions, referring c_p at T (in °C) to (extrapolated) values at room temperature:

$$c_{P,s}(T) = c_{P,s}(25\text{ °C}) \cdot [1 + 0.003 \cdot (T - 25)], \quad (2.1)$$

$$c_{P,\ell}(T) = c_{P,\ell}(25\text{ °C}) \cdot [1 + 0.0012 \cdot (T - 25)]. \quad (2.2)$$

Here (2.1) is valid for s = “solid” state, i.e. both semi-crystalline polymers with $T < T_M$ and amorphous thermoplastics with $T < T_G$; otherwise (2.2) applies – for ℓ = “liquid” state.

As an alternative, constant levels are used in the solid and liquid states, respectively. The error of such an approximation can be evaluated by (2.1) and (2.2), where the c_p -values change by 30% and 12%, respectively, over a 100 °C interval.

At constant pressure, the cumulative heat capacity of a material is its enthalpy. As a function of temperature, the enthalpy curve shows a steep increase (discontinuity) at the melting point, while the glass transition temperature corresponds to a discontinuity in its derivative only. The heat of crystallisation L_M is of magnitude ([Van Krevelen])

$L_M \approx 0.55 \cdot c_{P,\ell}(25\text{ °C}) \cdot (T_M - T_G)$, e.g. $L_M \approx 100$ kJ/kg for PS, and is proportional to the degree of crystallinity.

2.2.2 Density and thermal conductivity

[Van Krevelen], p.90, presents one way to estimate the density $\rho(T)$, by use of the MTE-model (the Molar Thermal Expansion model of polymers), based upon a concept of Simha & Boyer:

The molar volume V is the product of specific volume ρ^{-1} and molar weight M , i.e. $V = M / \rho$. All necessary polymer properties are referred to the Van der Waals volume V_W , the volume enclosed by the electron clouds of the molecules. Extrapolation of data for amorphous polymers in their rubbery (r) and glassy (g) states, respectively, gives

$$V_r(20^\circ\text{C}) = 1.60 \cdot V_W, \quad V_g(20^\circ\text{C}) \approx 1.6 \cdot V_W.$$

The molar thermal expansivity E is defined by $E := \left(\frac{\partial V}{\partial T} \right)_P$.

According to the Simha & Boyer model and to experimental data

$$E_r = 1 \cdot 10^{-3} V_W, \quad E_g = 0.45 \cdot 10^{-3} V_W.$$

Consider, e.g., PVC with $\rho(20^\circ\text{C}) = 1.38 \text{ kg/dm}^3$, $T_G = 80^\circ\text{C}$, $M = 0.0625 \text{ kg/mol}$ and $V_W = 0.0293 \text{ dm}^3/\text{mol}$, i.e. $M / V_W = 2.133 \text{ kg/dm}^3$. At $T = 200^\circ\text{C}$, we get

$$V_r(T) = V_g(20^\circ\text{C}) + E_g \cdot (T_G - 20) + E_r \cdot (T - T_G) = 1.747 \cdot V_W$$

$$\rho(200^\circ\text{C}) = \frac{M}{V_r(200^\circ\text{C})} = \frac{M / V_W}{1.747} = 1.22 \text{ (kg/dm}^3\text{)}$$

i.e. the density is around 12% less than at room temperature. By modelling two constant levels, above and below T_G , respectively, the error becomes less than 4% for PVC.

Van Krevelen's suggested method for semi-crystalline materials is to weigh the molar volumes of the pure states, crystalline and amorphous, according to the degree of crystallinity, and to use

$$V_c(20^\circ\text{C}) = 1.435 \cdot V_W, \quad V_\ell(20^\circ\text{C}) = V_r(20^\circ\text{C}),$$

$$E_c \approx E_g, \quad E_\ell \approx E_r$$

as well as the melting expansion

$$\Delta V_M = V_\ell(T_M) - V_c(T_M).$$

A simpler model is to apply two constant levels of density, above and below T_M , respectively.

The isothermal compression of a thermoplastic from normal air pressure to the operating pressure p (in kbar) can be estimated by the Tait-relation ([Van Krevelen], p.101)

$$\frac{V(1 \text{ bar}) - V(p)}{V(1 \text{ bar})} = 0.0894 \cdot \ln \left[1 + \frac{p}{0.06 \cdot B} e^{0.0045 \cdot T} \right], \quad (2.3)$$

where T (in $^\circ\text{C}$) is the operating temperature and B (in kbar) is the bulk modulus, i.e. the hydrostatic pressure divided by the volume change per unit volume.

As a rule, models for the filling process phase are based upon incompressibility (contrary to the succeeding packing phase of material compression). To judge such an assumption, consider, for example, PVC with temperature 200°C at the mould entrance and injection

2.2 Temperature dependent material properties

pressure 100 MPa = 1 kbar. Formula (2.3) predicts the shrinkage $\Delta V/V = 0.047$, i.e. around 5%.

Thermal conductivity λ across an area A in the normal direction x of a body is defined by the heat transfer rate q and the corresponding temperature (directional) derivative $\frac{\partial T}{\partial x}$ as

([Holman], p.2) $\lambda := -q / A \frac{\partial T}{\partial x}$. In theory ([Tadmor & Gogos], p.129), thermal conductivity

of a plastic is anisotropic – heat is transmitted easier along the primary chemical bonds than between the polymer chains. Near the mould walls a high degree of orientation is expected. These effects on heat transfer are possibly greater than the temperature induced conductivity variations, the latter of order 30-40% for injection moulding. However there is a general lack of data ([Kennedy], p.19).

If λ is plotted against T/T_G for different materials, amorphous polymers and polymer melts show similar $\lambda(T/T_G)$ -curves ([Van Krevelen], p.529), increasing slowly up to $T/T_G = 1$ and then levelling out or decreasing slowly linearly. Replacing such a curve by a constant conductivity means an error of around 5% in the operating interval $T/T_G \in (0.6, 1.5)$. Below T_G , $\lambda / \rho c_p$ is expected to be proportional to the sound velocity u ([Van Krevelen]). Since ρ and u vary slowly, λ is nearly proportional to c_p in the glassy state (cf. **Appendix 3**).

For a semi-crystalline polymer, at $T < T_M$, information about the pure crystalline and amorphous states, respectively, can be weighed according to the degree of crystallinity. For the pure crystalline state, the Leibfried-Schloemann formula $\lambda \propto 1/T$ applies ([Perepechko], p.51), since typical moulding conditions are above the Debye temperature. [Van Krevelen], p.528 refers to results of Eiermann: $\lambda \approx 210/T$ (W/m² K). Thus for PP, e.g., with melting point $T_M = 165$ °C the crystalline conductivity is reduced by 1/3 from room temperature up to T_M . By a linear approximation the error becomes less than 3% for PP.

The thermal conductivity increases only slightly with the pressure, less than 5% from atmospheric conditions up to 25 MPa ([Rao], p.39).

2.2.3 Viscosity

Let $\eta = \eta(T, p, \dot{\gamma})$ denote the fluid viscosity at temperature T , pressure p and shear rate $\dot{\gamma}$. The distance model is derived from a power-law assumption, which for pure shear flow (τ denotes the shear stress and n the power-law index) is

$$\tau = -\eta \cdot \dot{\gamma}, \quad \eta = \eta_0(T, p) \cdot \dot{\gamma}^{n-1};$$

where η_0 is the temperature-pressure dependent “normed” viscosity (for $\dot{\gamma} = 1$). For high melt temperatures an Arrhenius-type model (see, e.g., [Agassant et al.], p.366) is expected:

$$\eta_0(T, p) = K_0 \cdot e^{B/T} \cdot e^{\beta p}.$$

For thermoplastics, pressure coefficient data $\beta \approx 2 - 6 \cdot 10^{-8} \text{ Pa}^{-1}$ are reported ([ibid.], p.366). With $p \approx 100 \text{ MPa}$, say close to a point of injection, the normed viscosity for $\beta = 3.3 \cdot 10^{-8} \text{ Pa}^{-1}$ becomes around 27 times greater than at the free flow front; which should be taken into account ([Rao], p.18). This recommendation seems unheard of in commercial

programs: despite its six parameters, the Moldflow 2nd order viscosity model ([Kennedy], p.11) neglects the pressure influence.

According to the WLF equation (Williams, Landel & Ferry 1955; see e.g., [Van Krevelen], p.466), the extra free volume created from thermal expansion accounts for the rapid viscosity drop between temperatures T_G and $T_G + 100$. The average reduction is of magnitude $10^6 : 1$ from T_G to $1.2T_G$. The combined temperature-pressure dependence is here described by seven parameters. However, for the filling phase, where the main flow occurs at an essentially uniform temperature, the simpler Arrhenius-type model might do ([Isayev], p.22). [Bicerano], p.298, describes the possibility to combine Van Krevelen's universal curve for $T \in [T_G, 1.2T_G]$ with an Arrhenius-type model for $T \geq 1.2T_G$. As a compromise we implement the two-parameter temperature dependence $e^{B/(T-T_B)}$, which permits rapid changes immediately above T_G (for $T_B \approx T_G$) and turns into an Arrhenius-behaviour for $T \gg T_B$.

The power-law index n is essentially independent of temperature ([Baird & Collias], p.97). However, at fixed temperature, the fitted n -value may be halved when the shear rate $\dot{\gamma}$ is 10^2 -fold increased (see [Van Krevelen], p.475). Such a span ($10^2 : 1$) is standard across the mould gap, since according to [Agassant et al.], p.142, $\dot{\gamma} \approx C(r) \cdot z^{1/n}$ at the relative position z in a disk-shaped mould (with $z = 0$ at the centre plane and $z = 1$ at the wall surface), i.e. the shear rate ratio between the outer $x\%$ and the inner $x\%$ of the flow, will satisfy $\left(\frac{100-x}{x}\right)^{1/n} = 10^2$, e.g. for $n = 0.3$ (or less) involving (the inner + outer) $2x = 40\%$ of the flow.

The viscosity η is expected to show a general decrease by increasing shear rates from a constant level of Newton-like fluid ($n \approx 1$) for low $\dot{\gamma}$ -values to the asymptotic power-law shear-thinning property for high $\dot{\gamma}$ -values ($n \approx 0.2$, cf. [Agassant et al.], p.351). This behaviour is captured by the two-parameter Carreau-Yasuda law models (e.g., [Sigüner et al.], p.945), with $\eta/\eta_0 = (1 + \theta\dot{\gamma})^{n-1}$ as a particular choice. As a compromise we implement the power-law model but will choose the exponent n to reflect the operating conditions rather than the asymptotic value. This leaves us with the five-parameter (K_0, B, T_B, β, n) viscosity model

$$\eta = K_0 \cdot e^{B/(T-T_B)} \cdot e^{\beta p} \cdot \dot{\gamma}^{n-1}. \quad (2.4)$$

In divergent flow, like a centre-gated disk, the radially diverging streamlines cause stretching in the tangential direction, notably in the centre plane (see [Pearson], p.610).

2.2.4 Dimensionless groups and asymptotic temperature profiles

The Reynolds number Re (see, e.g., [Holman], p.221) characterises laminar and turbulent flow:

$$Re := \frac{\rho \bar{v}_r H}{\eta}.$$

For injection moulding typical values are of magnitude

$\rho = 10^3 \text{ kg/m}^3$, $\bar{v}_r = 10^{-1} \text{ m/s}$, $H = 10^{-3} \text{ m}$, $\eta = 10^4/10^2 \text{ kg/m} \cdot \text{s} \Rightarrow Re \leq 10^{-3}$
i.e. creeping flow ($Re \ll 1$) is expected.

2.2 Temperature dependent material properties

The Cameron number Ca (see, e.g. [Agassant et al.], p.83) is the inverse of the Graetz number Gz and describes how well developed the temperature distribution is:

$$Ca := \frac{\kappa \cdot r}{\bar{v}_r H^2}.$$

Here κ is the diffusivity, i.e. a material characteristic measuring how fast temperature differences are reduced by conduction. Characteristic values are

$$r = 10^{-1} - 10^0 \text{ m}, \quad \kappa := \frac{\lambda}{\rho c_p} = 10^{-7} \text{ m}^2/\text{s} \Rightarrow Ca = 10^{-1} - 10^0$$

which means a transition flow regime ($10^{-2} < Ca < 10^0$), i.e. a developing temperature profile; except at the very entrance where adiabatic conditions ($Ca < 10^{-2}$) are expected.

The Brinkman number Br (see [ibid.], p.86) relates the viscous dissipation and heat conduction:

$$Br := \frac{\eta \bar{v}_r^2}{\lambda \Delta T}.$$

Characteristic values are

$$\lambda = 10^{-1} \text{ W/m}^\circ\text{C}, \quad \Delta T = 10^2 \text{ }^\circ\text{C} \Rightarrow Br = 10^{-1} - 10^1.$$

This means that both viscous dissipation and conduction influence the temperature profile.

The Péclet number Pe (e.g., [Rao], p.58) is the ratio of convective heat transfer to conduction:

$$Pe := \frac{\bar{v}_r H}{\kappa}.$$

A typical value is $Pe = 10^3$ ($Pe \gg 1$), which characterises a “thin cold thermal boundary layer” (of frozen melt) “surrounding a hot core region” (of streaming fluid; [Isayev], p.25). However, Ca (or Gz) is preferred when heat conduction is in transverse flow direction ([Tucker], p.86).

The Pearson number Pn (see, e.g., [Tucker], p.120) describes how much the temperature dependent exponent of the viscosity varies. If an Arrhenius-type exponent is used ([Van Krevelen], p.342), then the temperature variation of many liquids (index ℓ) corresponds to $Pn_\ell = 10^0$. A small Pn , and $Br \approx 1$, means that the momentum equations decouple from the energy equation – an isothermal flow. Injection moulding is a borderline case ([Pearson], p.120).

Asymptotic results on temperature profiles (e.g., [Tucker], p.121) presume extreme ($\gg 1$ or $\ll 1$) Ca and/or Pn values, and are therefore not generally applicable in typical moulding situations. Moreover, the dynamic nature of the filling process – local fluid velocities varying due to, e.g., complex cavity geometry – makes a classification by dimensionless quantities uncertain.

2.2.5 Assumptions

In each thermoplastic phase of state, i.e. below and above T_M (or $T_{no-flow}$ denoting a characteristic “no-flow” temperature), respectively, ρ is assumed constant but λ, c_p may be linear functions of temperature. Furthermore, L_M is considered and (2.4) is applied with fixed n . These assumptions will be examined in **Ch. 4** and briefly commented in **Ch. 6**.

2.3 The governing equations

2.3.1 General notation

Consider a mass point at \mathbf{x} in physical space, at time t . Notations:

$\rho(\mathbf{x}, t)$, $\mathbf{v}(\mathbf{x}, t)$ density and velocity, respectively

$\beta := \frac{1}{\rho} \cdot \left(-\frac{\partial \rho}{\partial T} \right)_p$ coefficient of thermal expansion (notation in this **Sec.** only)

$\mathbf{T}(\mathbf{x}, t)$ Cauchy's stress tensor (notation in this **Sec.** only)

$\mathbf{g}(\mathbf{x}, t)$ body force per unit mass, e.g. gravity (notation in this **Sec.** only)

$p := -\frac{1}{3} \text{tr}(\mathbf{T})$ thermodynamic, isotropic pressure; where $\text{tr}(\mathbf{A}) := \sum_i A_{ii}$

$\mathbf{D} := \frac{1}{2} (\nabla \mathbf{v} + (\nabla \mathbf{v})^T)$ rate of strain (rate of deformation) tensor (notat. in this **Sec.** only)

$\dot{\gamma} := \sqrt{2\mathbf{D} : \mathbf{D}}$ shear rate; where $\mathbf{A} : \mathbf{B} := \sum_{i,j} A_{ij} B_{ij} (= \text{tr}(\mathbf{A}^* \mathbf{B}))$, \mathbf{A}^* is the conjugate-

transpose of \mathbf{A}

$U(\mathbf{x}, t)$ internal energy per unit mass

$\mathbf{q}(\mathbf{x}, t)$ heat flux vector, e.g. conduction and radiation

λ second-rank tensor form of the thermal conductivity for non-isotropic materials (e.g., [Baehr & Stephan], p.280), cf. **Sec. 2.2.2**.

2.3.2 Mass and momentum balance

Equation of continuity (conservation of mass):

$$\frac{\partial \rho}{\partial t} + \text{div}(\rho \mathbf{v}) = 0.$$

Equation of motion, Cauchy's law (conservation of linear momentum):

$$\rho \frac{D\mathbf{v}}{Dt} - \text{div}(\mathbf{T}) - \rho \mathbf{g} = \mathbf{0}.$$

Here the material derivative is defined as $\frac{D\mathbf{v}}{Dt} := \frac{\partial \mathbf{v}}{\partial t} + \nabla \mathbf{v} \bullet \mathbf{v}$, where $(\nabla \mathbf{v})_{ij} := \frac{\partial v_i}{\partial x_j}$

and \bullet denotes tensor (here a matrix-vector) product.

Conservation of angular momentum: \mathbf{T} is symmetric.

Constitutive equations:

Incompressible fluid: $\rho = \text{const}$, or a thermodynamic PVT-equation of state: $\rho = \rho(p, T)$.

Generalised Newtonian fluid: $\mathbf{T} = -p\mathbf{I} + 2\eta\mathbf{D}$, power-law fluid: $\eta := \eta_0 \dot{\gamma}^{n-1}$, $\eta_0 = \eta_0(p, T)$.

Apart from a small n -value, the basic assumptions of the distance model ([Aronsson]) are essentially the Hele-Shaw flow ([Hieber & Shen]) and lubrication approximations (e.g., [Tucker], p.90):

- The fluid is incompressible and generalised Newtonian.
- The flow is fully developed and laminar.
- The flow is isothermal, or rather: η is a function of $\dot{\gamma}$ only.

2.3 The governing equations

- The viscosity is of power-law type (with constant n).
- Inertial and body forces are negligible compared to viscous forces and pressure differences.
- The gap width (defining the z -direction of a plate cavity), denoted $2H(x, y)$, is much smaller than other (x - y) dimensions.
- The gap width is constant or varies slowly.
- There is no slip at the (horizontal) walls.
- The z -component of viscosity forces is negligible.
- The x - y velocities vary much slower in the x - y directions than in the z -direction.

The pressure is seen to be independent of z , i.e. $p = p(x, y, t)$, and obeys the mass conservation law

$$\operatorname{div}\left(H(x, y)^{2+\frac{1}{n}}|\nabla p|^{\frac{1}{n}-1}\nabla p\right)=0.$$

If H is constant, this turns into the elliptic $(\frac{1}{n} + 1)$ -harmonic equation, for $n = 1$ written $\Delta p = 0$.

The main principle of the distance model is the pseudo-circle principle ([Aronsson], p.428):

For small n -values, the fluid region of the mould expands approximately like a family of pseudo-circles with respect to the metric $H(x, y)^{-1}ds$, where s is arc length, each having its centre at the injection point.

An examination of the order of magnitude in the Hele-Shaw approximation (e.g., [Advani], p.422) simplifies the momentum equations. In Cartesian coordinates, $\mathbf{v} = (v_x, v_y, v_z)$:

$$\begin{cases} \frac{\partial p}{\partial x} = \frac{\partial}{\partial z} \left(\eta \frac{\partial v_x}{\partial z} \right), \\ \frac{\partial p}{\partial y} = \frac{\partial}{\partial z} \left(\eta \frac{\partial v_y}{\partial z} \right), \\ \frac{\partial p}{\partial z} = 0. \end{cases} \quad (2.5)$$

Assuming no-slip at the wall surface $z = \pm H$ and symmetry $\partial v_x / \partial z = 0, \partial v_y / \partial z = 0$ at the gap centre plane, the local velocities are retrieved from the pressure gradient by integration over the gap (e.g., [Siginer et al.], p.952). From a given time evolution of the inlet pressure or the inflow rate, the gap-wise average velocities $\bar{v}_x(\mathbf{x}, t), \bar{v}_y(\mathbf{x}, t)$ are determined for every (\mathbf{x}, t) according to the distance model (by efficient shortest-route calculations, even in complex geometries, see e.g. [Johansson]). By use of the fluidity ([Siginer et al.]), the pressure field gradient, and hence the local velocities, can be determined.

2.3.3 Energy balance

Assume that there is no internal heat generation, except for viscous dissipation.

Thermal energy equation, 1st law of thermodynamics (conservation of energy):

$$\rho \frac{DU}{Dt} + \text{div}(\mathbf{q}) - \mathbf{T} : \nabla \mathbf{v} = 0.$$

A temperature formulation is obtained by relating internal energy and temperature according to thermodynamic relations and the equation of continuity ([Kennedy], p.54):

$$\rho \frac{DU}{Dt} = \rho c_p \frac{DT}{Dt} - \beta T \frac{Dp}{Dt} - p \cdot \text{div}(\mathbf{v}).$$

Constitutive equation:

Fourier's law for conductive flux: $\mathbf{q}_{cond} = -\boldsymbol{\lambda} \cdot \nabla T$ or $q_{cond} = -\lambda \cdot \nabla T$ (isotropic).

For a generalised Newtonian (incompressible) fluid, the energy equation becomes

$$\rho c_p \frac{DT}{Dt} + \text{div}(\mathbf{q}) - \eta \dot{\gamma}^2 - \beta T \frac{Dp}{Dt} = 0.$$

If radiation is omitted and conduction is isotropic, then a dimensional analysis (cf. [Kennedy], p.69) shows that the energy equation for the filling phase can be simplified to

$$\rho c_p \left(\frac{\partial T}{\partial t} + v_x \frac{\partial T}{\partial x} + v_y \frac{\partial T}{\partial y} + v_z \frac{\partial T}{\partial z} \right) - \frac{\partial}{\partial z} \left(\lambda \frac{\partial T}{\partial z} \right) - \eta \dot{\gamma}^2 = 0. \quad (2.6)$$

The gap-wise convection term is relevant at the melt front and for tapered channel flow.

The momentum/pressure field equations and the energy equation are linked, if viscosity depends upon temperature.

In [Kennedy], p.71, the shear rate is approximated by $\dot{\gamma} \approx \sqrt{\left(\frac{\partial v_x}{\partial z} \right)^2 + \left(\frac{\partial v_y}{\partial z} \right)^2}$. Motivated by

our intended applications, with fluid streaming radially from an inlet point (v_r is the radial \mathbf{v} -component), but angular flow and angular shear (not stretching) being neglected, we extend this (cf. [Tadmor & Gogos], p.121) to

$$\dot{\gamma} = \sqrt{\left(\frac{\partial v_r}{\partial z} + \frac{\partial v_z}{\partial r} \right)^2 + 2 \left[\left(\frac{\partial v_r}{\partial r} \right)^2 + \left(\frac{v_r}{r} \right)^2 + \left(\frac{\partial v_z}{\partial z} \right)^2 \right]} \approx \sqrt{\left(\frac{\partial v_r}{\partial z} \right)^2 + \left(\frac{2v_r}{r} \right)^2}. \quad (2.7)$$

For strongly tapered flow the remaining terms should also be considered.

2.4 Boundary conditions

2.4.1 Symmetry, points of injection and mould walls

At the ("horizontal") centre plane of the mould cavity, $\partial v_x / \partial z = \partial v_y / \partial z = 0$ and $\partial T / \partial z = 0$.

The (majority of the) filling phase is controlled by a prescribed inflow rate function $Q = Q_I(t)$ at time t , possibly limited by an upper pressure bound p_I at the inlet. The inlet temperature is either uniform (implemented) or has a prescribed gap-wise profile $T = T_I(z)$,

2.4 Boundary conditions

characterized by the runner and gate systems; via the viscosity also specifying an initial fully-developed velocity profile $v_{x,I}$, $v_{y,I}$ by the equations in **Sec. 2.3**.

The lubrication approximation does not apply at the “vertical” cavity wall surfaces. Here the normal pressure gradient vanishes, $\partial p / \partial n = 0$. At the horizontal cavity walls the no-slip condition means $v_x = v_y = 0$. The vertical component v_z is adjusted to the variation by time and space of the (effective) cavity height. In case the whole injection cycle was to be modelled, the temperature variations within the metal mould (cavity walls) should be considered ([Rao], p.124). Unlike, e.g., glass forming ([Storck]) the temperature of the mould surface is here much closer to ambient temperature and we therefore ignore the radiation losses from the mould. Apart from the melt and cavity properties, the mould temperature variations are related to the conductive and convective properties of the cooling (and runner) systems. If the walls are not part of the model, then the temperature at the wall surface may be assumed constant $T = T_E$ or obey Newton’s law of cooling $(\lambda \cdot \partial T / \partial z)_{fluid} = \alpha \cdot (T - T_E)_{wall}$. The heat transfer coefficient α can be calculated for various cooling system layouts, as $\alpha = \lambda_{wall} / d$, where d denotes the thermal thickness, e.g. the normal distance from the wall surface to the cooling channels of temperature T_E (e.g., [Advani], p.427). A special case is an adiabatic regime, sometimes assumed close to the inlet ([Agassant et al.], p.64), whence the conduction through the walls can be neglected, $\partial T / \partial z = 0$. We have implemented a specific model of the horizontal mould walls – cf. **Sec. 3.2.5** below. The heat flux through the vertical walls is neglected, i.e. the (small) surfaces are assumed insulated.

2.4.2 Flow front

At the moving free melt front surface, pressure is atmospheric, $p = 0$, or controlled, $p = p_R$, provided there is no built-up air pressure due to inadequate venting of the mould. To keep the front profile intact as the front passes a horizontal position (x, y) , fluid elements on all vertical levels must have one and the same velocity in the flow direction r , i.e. $v_r(x, y, z) = \bar{v}_r(x, y)$. We will take the front to be flat and thus to advance uniformly according to the average flow expansion rate (cf. [Isayev], p.27).

The heat transferred in the radial direction to the air may be part of the PDE ([Tadmor & Gogos], p.597). Our special handling of the flow front – cf. **Sec. 3.1.4** – neglects this, i.e. the (small) surface is assumed insulated.

When two melt fronts collide and coalesce, forming a weld line, the boundary conditions state that both the pressure and the normal velocity are continuous across the weld line ([Isayev], p.48, and [Baird & Collias], p.281). These situations have not been implemented.

By formulating a thermal penetration length inside the mould wall, [Siginer et al.], p.963, use thermal shock theory to describe the initial temperatures of wall surface and liquid fluid at the front (to overcome the discontinuity $T_I \neq T_E$). We use a similar model, but also include a developing layer of immobile, “solid” fluid – see **Sec 3.1.3**.

3 Model and method

3.1 Analytical sub-models

In this **Chapter** our model and method are presented, for (pseudo-)radial expansion flow. Since the distance model ([Aronsson]) prescribes the average radial velocities only, it has to be supplied with a description of the velocity distributions. With focus on the energy equation we want to consider the links with the momentum equations in a simple way. The material in this **Section** is based upon an assumption of a special viscosity representation, corresponding to an extension of the isothermal case. In **Sec. 3.1.1** we obtain a series expansion for the vertical profile of the radial velocity. The concept is illustrated in **Appendix 1**. In **Sec. 3.1.2** the radial pressure distribution is treated. In the simplest case of a pressure dependent viscosity a logarithmic form is derived. In **Sec. 3.1.3**, motivated by our special interest in freezing risk, we study the expansion of the frozen layer (melt below the no-flow temperature). A minor extension of the classical square-root increase by time is formulated, to be used as initial guesses in our numerical FD routine. A further extension, a particular form of heat generation, is treated in **Appendix 2**. We also express the axial velocity (v_z -)distribution, related both to the radial variations of the (non-frozen) gap width and to the packing effect of solidification. The laminar radial flow implies fast-moving hot fluid at the centre plane ($z = 0$) of the mould cavity. The overall heat balance requires a special treatment of the moving front. Two options are given in **Sec. 3.1.4**, an extension of the traditional fountain effect and a convective sub-model, both based upon the underlying series expression for the z -factor of the (r, z) -separated viscosity form.

3.1.1 Vertical velocity profile

The distance model presumes isothermal viscosity. In a disk-shaped mould, with cavity gap $z \in [-H, H]$, axis-symmetry and purely radial flow, the isothermal velocity profile (e.g., [Agassant et al.], p.142) is

$$v_r(r, z) = \frac{\text{const}}{r} \cdot \left(H^{1+\frac{1}{n}} - |z|^{1+\frac{1}{n}} \right),$$

where n denotes the power-law index and the constant is related to a prescribed flow rate. By adopting such a universal velocity profile we would completely avoid the links with the momentum equations of **Sec. 2.3.2**. On the other hand, some consideration of temperature and pressure distributions for the local viscosity is conceivable – see (2.4). A radial-flow based model extension of the isothermal case is implemented. It is applied explicitly: after the local energy equations (for fixed time t) have been solved for $T(r, z)$, with a fixed velocity profile, a new universal velocity profile is fitted, for use in the next FD time step.

Instead of using a full FEM model we will limit our ambitions to a simple separation solution of the momentum equations. To accomplish that we will make an ansatz: let $h(r)$ be the unfrozen cavity height at radial position r , $h(r) \leq H$, and let \tilde{z} denote the relative vertical (axial) position at r , $\tilde{z} := z/h(r)$. Consider the flow situation for fixed time, and assume that the temperature-dependent factor K of the viscosity $\eta(r, z) := K(T) \cdot e^{\beta p} \dot{\gamma}^{n-1}$ satisfies

$$K^{-\frac{1}{n}}(T) = f(r) \cdot g(\tilde{z}) \quad (3.1)$$

3.1 Analytical sub-models

with g analytic, $g(\tilde{z}) = \sum_{m=0}^{\infty} b_m \tilde{z}^m$, and $f(r) := \overline{K^{-\frac{1}{n}}}(T(r, \tilde{z}))$ is the vertical average.

In particular for (2.4), $K(T) := K_0 \cdot e^{\frac{B}{T-T_B}}$, the implicit temperature profile is

$$T(r, \tilde{z}) = T_B - \frac{B}{\ln K_0 + n \cdot \ln f(r) + n \cdot \ln g(\tilde{z})}. \quad (3.2)$$

Although this “by-product” of our ansatz might be the base of an analytic solution – for an illustration see **Appendix 1** – we will (as promised) solve an energy PDE numerically.

In this **Section** let $h(r) \equiv h$, constant. For radial flow the equation of continuity becomes

$$\frac{1}{r} \cdot \frac{\partial}{\partial r} (r v_r) = 0.$$

This equation has a solution of the form $v_r(r, z) = \frac{\text{const}}{r} \cdot V(z)$, where the constant is chosen

such that $\bar{V} := \frac{1}{h} \cdot \int_0^h V(z) dz = 1$, i.e. $\bar{v}_r(r) := \frac{1}{h} \cdot \int_0^h v_r(r, z) dz = \frac{\text{const}}{r}$ is the vertical average.

Following [ibid.], p.142, we have $\dot{\gamma} \approx |\partial v_r / \partial z| = -\bar{v}_r(r) \cdot V'(z)$.

By dimensional analysis the momentum equations – cf. (2.5) – turn into

$$\begin{cases} \frac{\partial p}{\partial r} = \frac{\partial}{\partial z} \left(\eta \frac{\partial v_r}{\partial z} \right), \\ \frac{\partial p}{\partial z} = 0. \end{cases}$$

The special ansatz (3.1) makes it possible to write the first of these equations as

$$\frac{p'(r) f^n(r)}{\bar{v}_r^n(r) \cdot e^{\beta p(r)}} = -\frac{d}{dz} \left(g(\tilde{z})^{-n} [-V'(z)]^n \right) = \frac{-c}{h^{n+1}}. \quad (3.3)$$

Integration and use of the symmetry condition $V'(0) = 0$ gives

$$V'(z) = \frac{-(cz)^{\frac{1}{n}} g(\tilde{z})}{h^{\frac{1}{n} + 1}} = \frac{-c^{\frac{1}{n}}}{h} \left(\frac{z}{h} \right)^{\frac{1}{n}} \cdot \sum_{m=0}^{\infty} b_m \cdot \left(\frac{z}{h} \right)^m.$$

If the series is term-wise integrable and a no-flow condition is applied at $z = h$, then

$$V(z) = c^{\frac{1}{n}} \cdot \sum_{m=0}^{\infty} \frac{b_m}{1 + \frac{1}{n} + m} \cdot \left[1 - \left(\frac{z}{h} \right)^{1 + \frac{1}{n} + m} \right] =: \tilde{V} \left(\frac{z}{h} \right), \quad (3.4)$$

$$\bar{V} = c^{\frac{1}{n}} \cdot \sum_{m=0}^{\infty} \frac{b_m}{2 + \frac{1}{n} + m},$$

where $\bar{V} = 1$ determines c and the velocity profile $\tilde{V}(\tilde{z})$.

By letting $c_m := \frac{c^{\frac{1}{n}} b_m}{1 + \frac{1}{n} + m}$, $\bar{V} = 1$ corresponds to $\sum_m c_m \cdot \frac{1 + 1/n + m}{2 + 1/n + m} = 1$ and the profile is

$$\tilde{V}(\tilde{z}) = \sum_{m=0}^{\infty} c_m \cdot \left[1 - \tilde{z}^{1 + \frac{1}{n} + m} \right]. \quad (3.5)$$

The isothermal velocity profile corresponds to the leading term only, i.e. $g(z) = b_0$, constant. Since partial differentiation of (3.1), with $T = T(r, \tilde{z})$, formally yields

$$\frac{\partial T}{\partial z} = - \frac{n \cdot K(T) \cdot \sum m b_m \tilde{z}^{m-1}}{K'(T) \cdot hg(\tilde{z})}$$

the symmetry condition at $z=0$ implies $b_1 = 0$. In **Appendix 1** the profiles for one, two and three leading terms are illustrated.

The implemented velocity profiles admit 0 – 2 extra terms, apart from the isothermal case. The best powers m_1, m_2 of the additional terms are estimated to

$$\text{minimise}_{m_1, m_2} \sum_{i,j} w_j \cdot |K^{-\frac{1}{n}}(T_{ij}) - f_i \cdot [b_0 + b_{m_1} \cdot (\tilde{z}_j)^{m_1} + b_{m_2} \cdot (\tilde{z}_j)^{m_2}]|,$$

where w_j is the (control volume) weight of vertical position j and $f_i := f(r_i)$ is chosen as the vertical (j -)weighted average $f_i = \overline{K^{-\frac{1}{n}}}(T_{i\bullet})$. For fixed m_1, m_2 the coefficients b_0, b_{m_1}, b_{m_2} are computed by weighted least-squares (2 extra terms) or by fitting the average viscosity at the central plane and at the frozen layer surface (1 extra term).

An advantage of (3.4) is to admit also non-isothermal profiles. However, to define a solution of the equation of continuity, the coefficients $(b_m)_{m=0}^\infty$ should be global (i.e. common to all radial positions), and so should the temperature profile, by (3.2). In reality, velocity profiles change shapes (cf., e.g., [Manzione], p.258, and [Agassant et al.], p.146). An obvious alternative would be to estimate the coefficients locally, i.e. for fixed radius (and time). But we want to avoid solving systems of equations for velocities and pressure. In doing so, a drawback would be a negligence of restrictions – single fluid elements subject to the laminar flow movement and pressure of horizontally nearby elements – and the local impact upon the general flow pattern at the current time – especially near the front. Our implemented compromise is to use the global coefficients (3.4), but to account for local incompressibility (**Section 3.1.3**), front effects (**Section 3.1.4**) and inlet viscosity ((2.7)) – departures from the Hele-Shaw assumptions in **Sec. 2.3.2**. But any separation ansatz $v_r(r, z) = \bar{v}_r(r) \cdot V(z)$ – including the isothermal case – is compatible with (cf. **Sec. 2.4.2**) BC $v_r(r, z) = \bar{v}_r(r)$ at the front, only if the front zone is separately handled.

3.1.2 Pressure distribution

The pressure is needed for viscosity calculations and for satisfying processing conditions. In the isothermal case ([Agassant et al.], p.143) the radial profile, for prescribed rest pressure

$p(R) = p_R$ at the front $r = R$, becomes

$$p(r) = p_R + \text{const} \cdot (R^{1-n} - r^{1-n}).$$

In our more general setting, integration of the first (radial) formula in (3.3) for $\beta \neq 0$ gives

$$e^{-\beta p} = e^{-\beta p_R} - \beta \cdot \int_r^R D(r') dr', \quad D := \left(\frac{c^{\frac{1}{n}} \bar{v}_r(r')}{f(r') h(r')^{1+\frac{1}{n}}} \right)^n.$$

Here the radial variation of f reflects that of the average temperature. Hence in a first approximation f and h are constant. If the inflow rate Q is prescribed, then $\bar{v}_r(r) = \frac{Q}{2\varphi_{act} r h}$, where

φ_{act} is the active flow angle. Since c is determined by (3.4) and $\bar{V} = 1$, the profile becomes

3.1 Analytical sub-models

logarithmic

$$p(r) = -\frac{1}{\beta} \cdot \ln \left[e^{-\beta p_r} - \frac{\beta c}{1-n} \cdot \left(\frac{Q}{2\varphi_{act} f h^{2+\frac{1}{n}}} \right)^n (R^{1-n} - r^{1-n}) \right]. \quad (3.6)$$

If, instead, the inlet pressure p_0 is given at $r = r_0$, then \bar{v}_r and Q are settled by that condition.

For $\beta = 0$, with prescribed front pressure $p(R) = p_R$, we get

$$p(r) = p_R + \int_r^R D(r') dr'.$$

To cover the cases of non-constant f and/or h , the integrals for $\beta \neq 0$ and $\beta = 0$ are discretized by the trapezoidal rule to yield

$$p(r_i) = p(r_{i+1}) + e^{\beta p(r_{i+1})} \cdot \frac{\Delta r}{2} \cdot [D(r_i) + D(r_{i+1})].$$

Here $\Delta r := r_{i+1} - r_i$, the distance between consecutive radial node levels.

3.1.3 Freezing layer

As the polymer temperature drops towards the cold mould wall, the viscosity increases rapidly and the flow eventually ceases. For a semi-crystalline material the melting point T_M is a natural temperature limit for a ceasing flow. Also for an amorphous polymer a practical no-flow temperature $T_{no-flow}$, here written T_M , can be defined (e.g., [Kennedy], p.14), at the glass transition temperature T_G or (slightly) above. The growth of the frozen layer, characterised by $T < T_M$, at the cavity wall now becomes decisive for the possibility of filling the whole mould.

The Stefan problem, initially formulated for the thickness of polar ice, is to determine the moving surface of separation between two phases. If convection is omitted and the mould gap is considered as a 1-dimensional, semi-infinite medium of phase-specific properties, with fixed temperature T_l at infinity, then a characteristic square-root increase by time of the frozen layer thickness $\delta := H - h$ is obtained. By using a property index notation $i=s$ (solid), ℓ (liquid), w (wall) for conductivity λ_i , density ρ_i , specific heat $c_{P,i}$ and diffusivity

$\kappa_i := \lambda_i / \rho_i c_{P,i}$, the position of the moving surface can be written $\delta(t) = 2\varepsilon \sqrt{\kappa_s t}$, where t denotes the time of contact and ε is a constant yet to be determined: a square-root model. If the wall surface is kept constant at temperature T_E , and the change of volume on solidification is taken into account as the surface advances, then ε satisfies ([Carslaw & Jaeger], p.291)

$$\frac{\exp(-\varepsilon^2)}{\operatorname{erf}(\varepsilon)} - \frac{c_1(T_l - T_M)}{T_M - T_E} \cdot \frac{\exp(-(c_2\varepsilon)^2)}{1 - \operatorname{erf}(c_2\varepsilon)} = \frac{L_M \sqrt{\pi}}{c_{P,s}(T_M - T_E)} \varepsilon, \quad (3.7)$$

where L_M denotes the latent heat of crystallization, $\exp(a) \equiv e^a$, erf is the error function (e.g. [ibid.], .482), and

$$c_1 := \frac{\lambda_\ell \sqrt{\kappa_s}}{\lambda_s \sqrt{\kappa_\ell}}, \quad c_2 := \frac{\rho_s \sqrt{\kappa_s}}{\rho_\ell \sqrt{\kappa_\ell}}.$$

If, instead, the wall too is assumed to be a semi-infinite medium, with fixed temperature T_E at

minus infinity and the change of volume by solidification is taken into account, then ε can easily be shown to satisfy (cf. [ibid.], p.288, where that effect is neglected)

$$\frac{\exp(-\varepsilon^2)}{c_0 + \operatorname{erf}(\varepsilon)} - \frac{c_1(T_I - T_M)}{T_M - T_E} \cdot \frac{\exp(-(c_2\varepsilon)^2)}{1 - \operatorname{erf}(c_2\varepsilon)} = \frac{L_M \sqrt{\pi}}{c_{P,s}(T_M - T_E)} \varepsilon, \quad (3.8)$$

where

$$c_0 := \frac{\lambda_s \sqrt{\kappa_w}}{\lambda_w \sqrt{\kappa_s}}.$$

In injection moulding the square-root models have to be local, with $t = 0$ corresponding to the front passage (local activation time). Although the BC at infinity, $T = T_I$, imitates the strong inflow of heat near the centre plane of the mould cavity, some convective flow and all viscous heat generation are ignored, and therefore the δ -formulas above, applied at the end of the filling phase, overestimate the risk of total freezing. Furthermore, close to the injection point a region of adiabatic flow regime leads to a steady δ -decrease towards the inlet (L  v  que solution, [Pearson], p.579, and [Tucker], p.131): the Stefan problem is 2D, at least. If convection and viscous heat are included, only asymptotic results (e.g., [Tucker], p.132, and [Pearson], p.600) exist.

In **Appendix A1.2** we extend the square-root models (3.7) - (3.8) to include a special form of heat generation, to imitate the local net inflow of hot fluid and dissipation of viscous energy. Although the result is a less crude estimate of the freezing risk, it has not been implemented and evaluated. Instead, the general square-root behaviour is used to provide initial guesses for the local freezing layer position, in the iterative numerical FD routine described below. The temperature of the wall surface is accordingly initiated as

$$T_{surf} := T_E + \frac{T_M - T_E}{1 + \operatorname{erf}(\varepsilon)/c_0},$$

with ε given by (3.8).

Behind the front the \sqrt{t} -coefficient is estimated by exponential smoothing, i.e. a weighted average of the previous average and the current $\delta(t)/\sqrt{t}$ -value.

Since the focus is on freezing risk, the position of the frozen layer is subject to a special model below. First we consider the fluid shrinkage rate due to solidification ($\rho_s > \rho_\ell$), a pressure-dependent effect of order 10-20 % for typical semi-crystalline materials. The local movement of the liquid zone surface $h = h(\mathbf{x}, t)$, $\mathbf{x} := (x, y)$, $h = H - \delta$, generates a convection term along the z -direction: during time dt , when the zone surface advances a distance $dh (< 0)$, i.e. opposite the z -direction, the formed mass of solid per unit area $\rho_s \cdot |dh|$ has been formed from liquid of thickness $\rho_s \cdot |dh|/\rho_\ell$. Thus the liquid moves along the z -axis

with velocity $v_z = \left(\frac{\rho_s}{\rho_\ell} - 1 \right) \cdot \frac{-dh}{dt}$ at the surface ([Carslaw & Jaeger], p.291). Writing v_z in

this way we admit shrinking frozen layers as well – cf., e.g., **Fig. 5.11b** below.

Apart from dependency on t , $h = h(\mathbf{x}, t)$ is also spatially dependent. Horizontal variations of the effective height h , by non-uniform freezing or tapering flow, contribute to a vertical velocity component. Here we focus on the radial case, $h = h(r)$. According to (3.5), the radial velocity is

3.1 Analytical sub-models

$$v_r(r, z) = \bar{v}_r(r) \cdot \tilde{V}\left(\frac{z}{h(r)}\right), \quad \tilde{V}\left(\frac{z}{h}\right) = \sum_m c_m \cdot \left[1 - \left(\frac{z}{h}\right)^{1+1/n+m}\right].$$

Assuming $\bar{v}_r(r) = \frac{\text{const}}{r \cdot h(r)}$, forming $\frac{\partial v_r}{\partial r}$ and applying the equation of continuity

$$\text{div } \mathbf{v} \equiv \frac{\partial v_r}{\partial r} + \frac{v_r}{r} + \frac{\partial v_z}{\partial z} = 0,$$

we get the vertical acceleration

$$\frac{\partial v_z}{\partial z} = \bar{v}_r(r) \cdot \frac{h'(r)}{h(r)} \cdot \sum_m c_m \cdot \left[1 - (2 + 1/n + m) \cdot \left(\frac{z}{h}\right)^{1+1/n+m}\right].$$

From the symmetry condition $v_z = 0$ at $z = 0$ the velocity becomes

$$v_z(r, z) = \bar{v}_r(r) \cdot h'(r) \cdot \frac{z}{h(r)} \cdot \tilde{V}\left(\frac{z}{h(r)}\right),$$

going to zero also at the effective boundary $z = h(r)$, as it should.

We next consider the influence of $\frac{\partial h}{\partial t}$. Let

$$\tilde{U}(\tilde{z}) := \frac{1}{h} \cdot \int_0^{\tilde{z}} \tilde{V}\left(\frac{z'}{h}\right) dz' = \int_0^{\tilde{z}} \tilde{V}(\tilde{z}') d\tilde{z}' = \tilde{z} \cdot \sum_m c_m \cdot \left[1 - \frac{\tilde{z}^{2+1/n+m}}{2+1/n+m}\right], \quad (3.9)$$

where $\sum_m c_m \cdot \frac{1+1/n+m}{2+1/n+m} = 1$ implies $\tilde{U}(1) = 1$.

By assuming a vertical profile $v_z = -a \cdot \tilde{U}\left(\frac{z}{h}\right)$, $a := \left(\frac{\rho_s}{\rho_\ell} - 1\right) \cdot \frac{\partial h}{\partial t}$, a correct behaviour at

$z = h$ and at $z = 0$ is guaranteed. Moreover, the ansatz $v_r(r, z) = b(r) \cdot \frac{1}{h} \cdot \tilde{V}\left(\frac{z}{h}\right)$ solves the

corresponding equation of continuity $b'(r) + \frac{1}{r} \cdot b(r) = a$. (For constant a the general solution

is $b(r) = \frac{\text{const}}{r} + \frac{a}{2} \cdot r$.) Thus the influence upon v_r of $\partial h / \partial t$ becomes limited to the r -

dependent factor \bar{v}_r . In the numerical routine – cf. **Sec. 4.1.1** below – this is implemented as a successive correction of \bar{v}_r for the actual frozen layer.

In summary, the effect of a varying frozen layer (and tapering flow) is modelled as

$$v_z(r, z) = \bar{v}_r \cdot \frac{\partial h}{\partial r} \cdot \frac{z}{h} \cdot \tilde{V}\left(\frac{z}{h}\right) - \left(\frac{\rho_s}{\rho_\ell} - 1\right) \cdot \frac{\partial h}{\partial t} \cdot \tilde{U}\left(\frac{z}{h}\right). \quad (3.10)$$

3.1.4 Fountain flow

At the flow front the no-flow BC at the mould wall is associated with a special form of vertical convection – the fountain effect (e.g., [Tadmor & Gogos], p.600). We assume a vertical front surface, kept by a continuous transport of fast moving particles from the centre towards the wall. The neutral layer z_{neut} ([Advani], p.435) is defined by $V(z_{\text{neut}}) = \bar{V} (= 1)$.

For the isothermal velocity profile, $\tilde{z}_{neut} = (2 + \frac{1}{n})^{-1/(1+\frac{1}{n})}$. For the profile (3.5) the neutral layer satisfies

$$\sum_m c_m \tilde{z}^{1+\frac{1}{n}+m} = \sum_m \frac{c_m}{2 + \frac{1}{n} + m}.$$

Following ([Advani]) the fountain effect means that the material order on the vertical front is completely reversed for fluid elements moving faster than average at the front. A particle at initial position $z_1 (< z_{neut})$ ends up at $z_2 (> z_{neut})$, in general determined by the volume balance

$$\int_0^{z_1} [V(z) - \bar{V}] dz = \int_{z_2}^H [\bar{V} - V(z)] dz,$$

and for (3.5) specifically

$$\tilde{z}_1 \cdot \sum_m \frac{c_m}{2 + \frac{1}{n} + m} \cdot (1 - \tilde{z}_1^{1+\frac{1}{n}+m}) = \tilde{z}_2 \cdot \sum_m \frac{c_m}{2 + \frac{1}{n} + m} \cdot (1 - \tilde{z}_2^{1+\frac{1}{n}+m}).$$

At the wall surface, the maximum residence times are found close to the inlet – contrary to the particle history below the neutral layer. In the isothermal case, a proportion

$$\frac{1}{\bar{v}_r \cdot h} \int_0^{z_{neut}} [v_r(z) - \bar{v}_r] dz = (2 + \frac{1}{n})^{-(2+\frac{1}{n})/(1+\frac{1}{n})}$$

of all fluid is subject to fountain convection, i.e. around 19% for a Newtonian liquid and a vanishing percentage if $n \rightarrow 0$.

In the implementation, the front nodes that are reached during a time step are treated in two sub-steps. In the first sub-step, the fountain effect is modelled for every layer $z_2 (> z_{neut})$, accomplishing a temperature mixture with its mirror layer $z_1 (< z_{neut})$. In the second sub-step, modelled as a fixed percentage of the nominal time step, a succeeding standard conduction-convection FD-equation is solved.

As an alternative to the reversing fountain effect, we consider a more conventional convection upwards from the centre plane, but assumed to occur only at the front. To keep the front straight (cf. **Sec. 2.4.2**) the net volume that is transported vertically at level z must be proportional to the accumulated radial velocity surplus

$$\int_0^z [v_r(z') - \bar{v}_r] dz' = \bar{v}_r \cdot h \cdot [\tilde{U}(\tilde{z}) - \tilde{z}],$$

where $\tilde{z} := \frac{z}{h}$ and \tilde{U} is defined by (3.9). Thus

$$\tilde{W}(\tilde{z}) := \tilde{U}(\tilde{z}) - \tilde{z} = \tilde{z} \cdot \sum_m \frac{c_m}{2 + \frac{1}{n} + m} \cdot (1 - \tilde{z}^{1+\frac{1}{n}+m})$$

determines the vertical velocity at the front as

$$v_z(z) = \frac{1}{\Delta r} \cdot \int_0^z [v_r(z') - \bar{v}_r] dz' = \frac{h}{\Delta t} \cdot \tilde{W}(\tilde{z}).$$

3.2 PDEs and solution method

This **Section** includes a discussion of the energy PDE and the solution method. We express the problem by a system of PDEs for (U, h) , where U is the internal energy and h is the non-frozen cavity height. Apart from the angular subdivision into the two types of flow regions in **Fig. 1.1a** we make an axial subdivision between fluid above and below the no-flow temperature, and because of drastic simplification, the PDE is specially designed for all fluid below the no-flow temperature and for stagnant fluid also above. Another argument, given in **Sec 3.2.1**, for such a subdivision into regional PDEs is the discontinuity that the no-flow temperature (melting point) makes for semi-crystalline materials, and the link between temperatures and velocities (through h) for all thermoplastics. The well-posedness of the basic PDE, linearized, in a fixed region of streaming flow, and its implications for the nonlinear problem, is discussed in **Appendix 4**. In **Sec. 3.2.2** the main solution strategy, time marching and pseudo-radial marching, is described. In **Sec 3.2.3** the outer iterative procedure is in focus, for the position of the no-flow temperature, i.e. the frozen layer surface h . The equation to solve, $f(h, t) = 0$, is a nonlinear differential relation for h . We argue that, for fixed $t = t_k$, all the $f(h, t_k)$ -terms are expected to decrease by h , and that the extreme cases $h = H$ (no frozen layer at all) and $h = 0$ (complete freezing, i.e. a case of incomplete filling) can easily be identified. In **Sec. 3.2.4** we are treating the inner iterative procedure, for the vertical (axial) temperature profile $T(h, t_k)$, given h . The discrete version will result in a local 1D-system of nonlinear FD-equations to be solved. The main solution technique is the Newton-Raphson (NR) method, supplied by a Goldstein-Armijo type of step length routine. An overall objective function is used. Apart from an input-output data flow chart, two iteration flow charts, for the active and passive flow regions of the cavity, are presented. In **Sec. 3.2.5**, finally, the special handling of the cooling PDE is described. By a linearization of the temperature evolution at the cavity wall surface during a time step, a series solution makes it possible to update the interaction directly with the fluid equations. The discontinuity that occurs when the hot front meets the cold wall is reduced, by shorter time steps at the front. A further improvement is described in **Appendix 2**. If a particular form of heat capacity and conductivity might do, the solid phase as well would benefit from a series solution, as treated in **Appendix 3**.

3.2.1 General and regional melt PDEs

We shall formulate and solve an initial-boundary-value problem (IBVP), concerning the heat balance during the filling phase, time $t \in (0, t_{fill}]$, in a given centre-gated, plate-shaped cavity domain X , of centre-plane extent $\mathbf{r} \equiv (x, y) \in X$ and of constant gap width $z \in [-H, H]$.

Let $\mathbf{x} \equiv (\mathbf{r}, z)$ and let v_r be the local (pseudo-radial) flow directional component. Since (see **Sec. 3.1**) we will adjust v_r , v_z , $\dot{\gamma}$ for changes in effective flow gap $h = h(\mathbf{r}, t)$ and since (see (2.4)) η depends on $T = T(\mathbf{x}, t)$ and on $\dot{\gamma}$, our model in its present form (cf. (2.6)) is described by the PDE

$$\rho c_p(T) \left(\frac{\partial T}{\partial t} + v_r(h, \mathbf{x}, t) \cdot \frac{\partial T}{\partial r} + v_z(h, \mathbf{x}, t) \cdot \frac{\partial T}{\partial z} \right) = \frac{\partial}{\partial z} \left(\lambda(T) \cdot \frac{\partial T}{\partial z} \right) + \eta(T, h, \mathbf{x}, t) \cdot \dot{\gamma}^2(h, \mathbf{x}, t). \quad (3.11)$$

Here $(z =) h$ is determined by the condition $T(\mathbf{r}, h, t) = T_M$. By the assumptions in **Sec. 2.2.5** the coefficients $c_p(T)$, $\lambda(T)$ depend linearly on temperature T . The viscosity η depends nonlinearly on T , and on h , as do the velocities and the shear rate.

The PDE is quasi-linear (e.g., [Renardy & Rogers], p.45) and parabolic as defined by [Renardy & Rogers], p.40, but not according to [Gustafsson et al.], p.273 – since 1D conduction is assumed (i.e. one 2nd order derivative is missing = neglected). By the transformation ([Ames], p.358)

$$V := \int_{T_E}^T \lambda(\tau) d\tau,$$

the quasi-linear PDE can be transformed into a semi-linear PDE

$$\frac{1}{\kappa(T)} \cdot \left(\frac{\partial V}{\partial t} + v_r(h, \mathbf{x}, t) \cdot \frac{\partial V}{\partial r} + v_z(h, \mathbf{x}, t) \cdot \frac{\partial V}{\partial z} \right) = \frac{\partial^2 V}{\partial z^2} + \eta(T, h, \mathbf{x}, t) \cdot \dot{\gamma}^2(h, \mathbf{x}, t),$$

where $\kappa := \lambda/\rho c_p$ is the diffusivity and $T = T(V)$ is uniquely determined, since $V'(T) = \lambda(T) > 0$. We perform such a substitution of variables in a special case only – see

App. 3. But in **Sec. 3.3.1** below we will transform (3.11) into its conservative form

$$\frac{\partial U}{\partial t} + \frac{1}{r} \frac{\partial}{\partial r} (r v_r U) + \frac{\partial}{\partial z} (v_z U) = \frac{\partial}{\partial z} \left(\kappa \frac{\partial U}{\partial z} \right) + \eta \dot{\gamma}^2, \quad (3.12)$$

where $U(T) := \int_0^T \rho c_p(T') dT'$ – which of course can be interpreted as a PDE for the internal

energy U . Anyhow, $T = T(U)$ is uniquely determined, since $U'(T) = \rho c_p(T) > 0$.

The cavity centre plane $z = 0$ is considered as a symmetry plane, with BC $\frac{\partial T}{\partial z} = 0$, and only $z \geq 0$ is explicitly modelled. At the wall surface $z = H$, in common with a separate cooling model for the metallic mould (cavity wall) – see **Section 3.2.5** below – we require continuous local surface temperature and heat flux. At the internal moving boundary $z = h(\mathbf{r}, t)$, $h \leq H$, which separates frozen (“solid” s) and liquid (ℓ) melt, we impose conditions (BCs) on fixed (no-flow) temperature $T = T_M$ and on balanced heat flux, including latent heat of solidification. At the front a special treatment of the fountain effect (see **Sec. 3.1.4**) replaces the free boundary BC. At the inlet $\mathbf{r} = \mathbf{0}$ a fixed temperature $T = T_l$ is assumed (cf. **Sec. 2.4**). As initial condition (IC), an empty mould cavity, with $T = T_l$ at the inlet, is assumed.

The nonlinearity of (3.11) is most severe at the frozen layer surface $z = h$, in fact representing a discontinuity of the coefficients c_p, L_M, v_z and $\dot{\gamma}$. Moreover, v_r, v_z and $\dot{\gamma}$ depend on $h(\mathbf{r}, t)$. Furthermore, the uniformity of (3.11) is illusory:

The flow front evolution is essentially given, since it is determined by the flow rates and by the distance model. Both the local activation (front passage) time $t_{act}(\mathbf{r})$ and the local stagnation (flow stop) time $t_{stag}(\mathbf{r}) (> t_{act}(\mathbf{r}))$ are considered known. At each time t the plane domain X is partitioned into three (disjoint) sets, corresponding to the flow conditions. One set defines the points ahead of the flow front, the others are the active-flow set $A(t)$ and the passive-flow set $B(t)$:

$$A(t) := \{\mathbf{r} \in X \mid t \in [t_{act}(\mathbf{r}), t_{stag}(\mathbf{r}))\}, \quad B(t) := \{\mathbf{r} \in X \mid t \geq t_{stag}(\mathbf{r})\}.$$

3.2 PDEs and solution method

For any $\mathbf{r} \in X$, the time interval $[t_{act}(\mathbf{r}), t_{stag}(\mathbf{r})]$ is the local streaming period and $[t_{stag}(\mathbf{r}), t_{fill}]$ is the local stagnant period. Although equation (3.11) is generally applicable, it can be substantially simplified for cavity regions of stagnant fluid and/or solid melt:

- The PDE for the temperatures in the frozen layer (phase s) is reduced to mere 1D heat conduction, for $t \geq t_{act}(\mathbf{r})$ at every $\mathbf{r} \in X$, since horizontal heat conduction is considered negligible.
- In the stagnant period, i.e. for $t \geq t_{stag}(\mathbf{r})$ at every $\mathbf{r} \in X$, the PDE for the temperatures of the liquid phase (ℓ) is also reduced to mere 1D heat conduction.

These simplifications will lead to obviously simplified FD schemes – which are not explicitly shown. Another simplification would occur if we were content with constant parameters $\lambda_s, c_{P,s}$ in the solid phase or, more generally, if $\lambda_s(T)$ were proportional to $c_{P,s}(T)$, since then the frozen layer might be handled by a series solution – see **Appendix 3**.

All these circumstances point at a reformulation of the problem: We consider the frozen surface $h = h(\mathbf{r}, t)$ as a “primary” dependent variable, like $T = T(\mathbf{x}, t)$, and end up with a system of linked regional IBVPs, one for each phase of state (s, ℓ) and for each of two flow sets (active, passive). The regional energy equations are linked through h and the interface condition

$$\lambda_s(T_M) \cdot \left(\frac{\partial T}{\partial z} \right)_{s, z=h} - \lambda_\ell(T_M) \cdot \left(\frac{\partial T}{\partial z} \right)_{\ell, z=h} = L_M \rho_s \cdot \frac{\partial h}{\partial t} \quad (\mathbf{r}, t) \in X \times (0, t_{fill}]. \quad (3.13)$$

The additional IC is $h(\mathbf{r}, t_{act}(\mathbf{r})) = H$ and the BC is $h(\mathbf{0}, t) = H$.

Let $A_2 := \{(\mathbf{r}, t) \mid 0 < t \leq t_{fill}, \mathbf{r} \in A(t)\}$, $A_3 := \{(\mathbf{r}, z, t) \mid 0 < t \leq t_{fill}, \mathbf{r} \in A(t), 0 \leq z \leq h(\mathbf{r}, t)\}$.

The most general regional IBVP becomes the one that describes the heat balance in the liquid phase of the active-flow set:

$$\begin{aligned} \rho_\ell c_{P,\ell} \cdot \left(\frac{\partial T}{\partial t} + v_r \frac{\partial T}{\partial r} + v_z \frac{\partial T}{\partial z} \right) - \frac{\partial}{\partial z} \left(\lambda_\ell \frac{\partial T}{\partial z} \right) - \eta \dot{\gamma}^2 &= 0 & (\mathbf{r}, z, t) \in A_3, \\ T &= T_I & \mathbf{r} = \mathbf{0}, (z, t) \in [0, H] \times [0, t_{fill}], \\ \frac{\partial T}{\partial z} &= 0 & z = 0, (\mathbf{r}, t) \in A_2, \\ T &= T_M & z = h, (\mathbf{r}, t) \in A_2. \end{aligned} \quad (3.14)$$

Both (3.14) and the discussion above presume that the no-flow temperature is attained in the cavity gap. Otherwise, e.g. close to the inlet, an alternative BC of direct heat exchange with the cavity wall has to be formulated at the wall surface – see the cooling model in **Sec. 3.2.5** (also cf. **App. 3**). The other regional IBVPs (for passive ℓ and for s) are (weakly, i.e. at most quadratically) nonlinear 1D true parabolic heat conduction PDEs.

3.2.2 Time marching and pseudo-radial marching

The distance model provides information about the average flow velocity \bar{v}_r at each position $\mathbf{r} = (x, y) \in X$ and time t , and implies a steady flow direction for the whole streaming period of the filling. This means that the pseudo-circles, that describe the expanding flow front according to the distance model, become isobars, i.e. of common pressure, during the whole streaming period. At a given time the node points in our FD-routine should be treated in logical flow-order, by starting from the inlet and ending up at the front. Now, even in an application where the gap width varies, the front pseudo-circles (and isobars) define such a steady partial (flow-) order, by the pseudo-radii r , for every $(x, y) \in X$. We assume that all transverse (angular) flow interaction – including any energy exchange – can be neglected so that the flow can be considered 2D in space during the streaming period. The 2D energy principle is a good approximation as long as the temperature varies slowly transversely. But for a boundary stream line, i.e. close to a wall or a cavity region of stagnant fluid, the implicit adiabatic condition is an undisputable simplification – although the boundary area is small, as a rule. An alternative would be to solve a full 3D problem – and lose the inherited simplicity of the distance model. In our implementation we treat the horizontal positions in time-order (time marching) and spatial pseudo-circle-order (r -marching from inlet to front). The system of FD equations that requires solution is then confined to the problems at the vertical (axial) node levels, one 1D sub-problem for each fixed (x, y, t) .

For the FD discretization we will distinguish pseudo-circles separated by a constant pseudo-radial step Δr . In an application where the gap width varies, node points (x, y) are identified as the intersection between the pseudo-circles and a set of stream lines (fluid trajectories). The unique predecessor node of a nodal point is the point lying on the previous pseudo-circle and on the same stream line. In case the gap width is constant and the cavity is star-shaped, the flow front becomes circular and the stream lines become flow rays from the inlet.

3.2.3 Outer iteration: Surface of frozen layer

In **Sec. 3.2.1** we could see that a natural approach is to solve the regional IBVPs, e.g. (3.14), for $T = T(\mathbf{x}, t)$ with a prescribed (provisional) non-frozen height $h = h(\mathbf{r}, t)$. The choice of h , to match (3.13), is then an outer problem. The implemented time and radial marching means that we treat one time step k and pseudo-radial level i pair (k, i) at a time.

Formally the computation of h is performed in an outer iterative procedure. We consider the heat balance for the movement of the layer surface h by solving (3.13), written as $f(h, t) = 0$, with

$$f(h, t) := \lambda_s(T_M) \left(\frac{\partial T}{\partial z} \right)_{s, z=h} - \lambda_\ell(T_M) \left(\frac{\partial T}{\partial z} \right)_{\ell, z=h} - L_M \rho_s \frac{\partial h}{\partial t}.$$

Through the local vertical temperature profile $T = T(h, t)$, this is a nonlinear differential equation for h . In time step k , of length $\Delta t_k = t_k - t_{k-1}$, at $\mathbf{r} = \mathbf{r}_i$, the IC is $h(\mathbf{r}_i, t_{k-1}) = h_i^{k-1}$.

In the discrete FD-version we wish to compute $h_i^k = h(\mathbf{r}_i, t_k)$. Therefore we introduce for radial level i , time level k – apart from the fixed vertical levels – an extra (mobile) node $z = h_i^k$ to keep track of the local frozen layer surface. This node is characterised by a fixed

3.2 PDEs and solution method

no-flow temperature T_M and it separates two cavity gap regions, ℓ = liquid phase ($0 \leq z \leq h_i^k$) and s = solid phase ($h_i^k \leq z \leq H$), of possibly different material parameters λ, ρ, c_p . At the front (when $i = k$), the previous height h_i^{k-1} is taken as the result of an initial fountain effect or front convection (see **Sec. 3.1.4**), normally $h_i^{k-1} = H$. In general (when $i \leq k$), we will use the FD approximation

$$\frac{\partial h}{\partial t} \approx \frac{h_i^k - h_i^{k-1}}{\Delta t_k}.$$

An outer iteration means that a trial value $h = h_i^k$ is evaluated. The heat fluxes through $z = h$ at time t_k are determined by the result $T = T(h, t)$ of the inner temperature iterations (see next **Sec.**). All three terms in the expression for $f(h, t)$ are expected to be strictly decreasing functions of h ($= H - \delta$, where δ denotes the thickness of the frozen layer), since

- (1st term:) a fixed T_M at $z = h$ is to be matched by the local flux resulting from a fixed cooling temperature T_E at the fixed position $z = H + L$ (cf. **Sec. 3.2.5**),
- (2nd term:) a fixed T_M at $z = h$ is to be matched by the local flux resulting from an essentially constant temperature T_i at the fixed position $z = 0$,
- (3rd term:) enthalpy is absorbed (by the polymer) if $\frac{\partial h}{\partial t} > 0$.

Moreover, $f(h, t_k)$ becomes much less than zero by the first term if $h \rightarrow H$ (or T_M is attained within the wall), and much greater than zero by the second term if $h \rightarrow 0$ (or the freezing is complete). Hence the singular states $h = H$ and $h = 0$ can be identified. Otherwise $f(h, t_k) = 0$ has exactly one solution $h = h_i^k \in (0, H)$.

The updating of the trial value h is based upon accelerated linear extrapolation and weighted quadratic interpolation/interval bisection, guaranteed to converge at least linearly. The initial value is chosen by square-root extrapolation (see **Sec. 3.1.3**) from h_i^{k-1} . Provided that the convergence of the inner iterative (temperature) procedure can be proved, the overall convergence is established.

3.2.4 Inner iteration: Vertical temperature profile

In the discrete version of (3.11), the time and radial marching means that we consider one pair of discrete time t_k and horizontal (radial) position \mathbf{r}_i at a time, and refer the problem to the correct flow region, either active or passive. For fixed (k, i) the IBVPs of the two phases ℓ, s are discretized differently, but the two sub-systems of FD equations – uncoupled since their heat exchange is replaced by the interior BC $T = T_M$ at $z = h(\mathbf{r}_i, t_k)$ – for $J + 1$ vertical (axial) node level temperatures $\mathbf{T} = (T(\mathbf{r}_i, z_j, t_k))_{j=0}^J$ are treated simultaneously. Thus the PDE turns into a local system of FD-equations $f_j(\mathbf{T}) = 0 \quad j = 0, \dots, J$, or $\mathbf{f} = \mathbf{0}$ for short. The

equations are nonlinear by the presence of the viscous energy term and the temperature dependent parameters λ, c_p .

Let $\mathbf{G} := \nabla \mathbf{f}$ denote the Jacobian matrix. For the FD-scheme that we will derive in **Section 3.3.1**, the partial derivatives will constitute a tri-diagonal matrix $\mathbf{G} = \mathbf{G}(\mathbf{T})$. From a given iterate \mathbf{T} , new temperatures are searched along the Newton-Raphson direction $\mathbf{u} = -\mathbf{G}^{-1} \mathbf{f}$. For any linear \mathbf{f} , and otherwise close to a solution of $\mathbf{f} = \mathbf{0}$, the optimal step length 1 is expected. At a distance, step length control may be necessary. Consider an objective function $F := \sum_j f_j^2$, minimised by the solution of the PDE system. The gradient vector of F satisfies $\nabla F = 2\mathbf{G}^T \mathbf{f}$. If \mathbf{G} is non-singular and $\mathbf{f} \neq \mathbf{0}$, then $\nabla F \neq \mathbf{0}$ and the directional derivative along the Newton-Raphson direction becomes $\nabla F^T \mathbf{u} / |\mathbf{u}| = -2|\mathbf{f}|^2 / |\mathbf{u}| < 0$ – thus guaranteeing descent of F . Our step length strategy is to accept step length 1 if the F -reduction exceeds a predefined limit, e.g. 10% of $\nabla F^T \mathbf{u}$. Otherwise we apply the Goldstein-Armijo algorithm (e.g., [Ortega & Rheinboldt], p.503): the step length is halved until a proportionally reduced limit is exceeded, or else the step length reaches a prescribed lower limit, e.g. 1/128. This determines the new iterate \mathbf{T} . If the partial derivatives in \mathbf{G} are continuous and if the step length is chosen properly, descent methods are guaranteed to converge to a true solution. If \mathbf{G} is positive definite, then damped Newton methods show super-linear convergence; with an additional smoothness assumption of \mathbf{G} the convergence becomes quadratic ([ibid.], p.312).

As a starting temperature point \mathbf{T} in the first h -iteration, a weighted combination of the temperature solutions at the same radial node, previous time, and at the preceding radial node, same time, is used. In later h -iterations, the previous $\mathbf{T}(h)$ -solution is used as a starting point \mathbf{T} , adjusted to meet T_M at the new trial h -value. An alternative would be to use Richtmyer's linearization method (e.g., [Smith], p.144) as a start-up procedure.

As a backup procedure (e.g. in case of an almost singular Jacobian \mathbf{G}), the steepest descent direction $\mathbf{u} = -\nabla F$ is applied, with initial step length $s = F / |\nabla F|^2$, since this implies

$$F(\mathbf{T} + s \cdot \mathbf{u}) \approx F(\mathbf{T}) + s \cdot \nabla F(\mathbf{T})^T \mathbf{u} = 0.$$

The exceptional case $\nabla F(\mathbf{T}) = \mathbf{0}$, $\mathbf{f}(\mathbf{T}) \neq \mathbf{0}$ means that the iterative routine will stop at a \mathbf{T} that is not a solution. The risk of such a failure is investigated below in **Section 3.3.2**.

In **Flowcharts 3.1-3**, below, the data processing as well as the logic of the discrete FD-solution routine is illustrated, for active-flow and passive-flow. For active-flow, **Flowch. 3.2**, an angular equivalence is assumed, i.e. all nodes (of streaming fluid) on a radial level are equivalent as to temperature evolution. (This is the implemented program version, i.e. the special case where pseudo-radius and radius are synonymous.) For passive-flow, **Flowch. 3.3**, we distinguish node groups of different flow history, on each radial level.

3.2.5 Cooling PDE and its series solution

Along the lines of an \mathbf{r} -local, time step based FD-solution of the melt PDE, we formulate a 1D heat conduction model of the cooling problem. The model shall interact with our melt

3.2 PDEs and solution method

model which, as an FD-output, delivers the temperature change b at the wall surface during time step k and, as an input from the cooling model, receives the heat flux q_{surf} through the wall surface. Consider a metallic mould (cavity wall) of vertical extension $z' \in [0, L]$, $z' := H + L - z$ (cavity $z \in [0, H]$), where the temperature T_{surf} at the cavity wall surface $z' = L$ is assumed to be a prescribed linear function of time (during time step k) – see **Figure 3.1** – and the temperature at the cooling channels $z' = 0$ is constantly zero (BCs), i.e. T denotes the excess temperature above a given cooling temperature T_E . At local time $t' = 0$, $t' := t - t_{k-1}$, where t_{k-1} denotes the initial time of step k , of length $\Delta t_k := t_k - t_{k-1}$, the temperature profile $f(z')$ is given (IC). In practice, a new trial b -value and fixed $a, f, C_1(\Delta t_k), C_2(\Delta t_k)$ (see **Fig. 3.1**) determine q_{surf} . When the final b -value has been found, a, f are updated (for the next time step). The local IBVP (κ is constant) becomes

$$\begin{aligned} \frac{\partial T}{\partial t'} &= \kappa \cdot \frac{\partial^2 T}{\partial z'^2} & (z', t') \in [0, L] \times (0, \Delta t_k] \\ T(0, t') &= 0 & t' \in (0, \Delta t_k] \\ T(L, t') &= a + bt' & t' \in (0, \Delta t_k] \\ T(z', 0) &= f(z') & z' \in [0, L] \end{aligned}$$

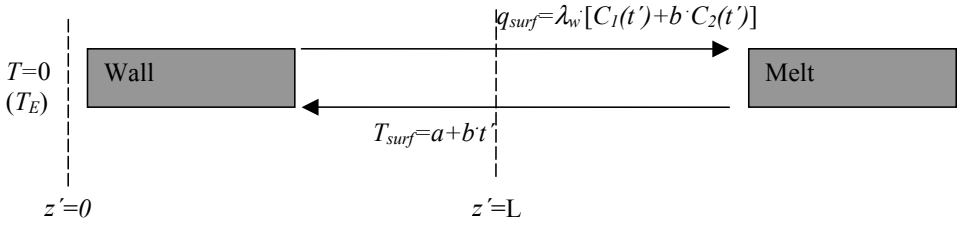


Figure 3.1 Input/output data at the series solution of the local cavity wall PDE. Time step k .

We look for a series solution. Let $T = V + W$, where V, W each satisfies a sub-problem

$$\begin{aligned} \frac{\partial V}{\partial t'} &= \kappa \cdot \frac{\partial^2 V}{\partial z'^2} & (z', t') \in [0, L] \times (0, \Delta t_k] \\ V(0, t') &= 0 & t' \in (0, \Delta t_k] \\ V(L, t') &= a + bt' & t' \in (0, \Delta t_k] \\ V(z', 0) &\text{unspecified} & z' \in [0, L] \end{aligned}$$

and

$$\begin{aligned} \frac{\partial W}{\partial t'} &= \kappa \cdot \frac{\partial^2 W}{\partial z'^2} & (z', t') \in [0, L] \times (0, \Delta t_k] \\ W(0, t') &= 0 & t' \in (0, \Delta t_k] \\ W(L, t') &= 0 & t' \in (0, \Delta t_k] \\ W(z', 0) &= f(z') - V(z', 0) & z' \in [0, L] \end{aligned}$$

The wall conduction problem is solved if the sub-problems are. Let $\mu_n := \frac{n\pi}{L}$ and take

$$V(z', t') = \frac{az'}{L} + \frac{bz'}{L} \cdot \left(t' + \frac{z'^2 - L^2}{6\kappa} \right),$$

$$W(z', t') = \sum_{n=1}^{\infty} W_n \cdot \sin(\mu_n z') \exp(-\kappa \mu_n^2 t'), \quad W_n := \frac{2}{L} \cdot \int_0^L [f(z') - U(z', 0)] \cdot \sin(\mu_n z') dz'.$$

Let $a = f(L)$ (constant) and define $g(z') := f(z') - \frac{az'}{L}$.

If $g(z')$ has a Fourier sine series expansion $g(z') = \sum_{n=1}^{\infty} g_n \cdot \sin(\mu_n z')$, then

$$W_n = g_n - \frac{2(-1)^n}{\kappa \mu_n^3 L} \cdot b.$$

The initial temperature profile of the next time period, $\tilde{f}(z') := T(z', \Delta t_k)$, is fixed by b and

$$\begin{aligned} \tilde{f}(z') &= (a + b \cdot \Delta t_k) \cdot \frac{z'}{L} + \tilde{g}(z'), \\ \tilde{g}_n &:= g_n \cdot \exp(-\kappa \mu_n^2 \Delta t_k) + b \cdot \frac{2(-1)^n}{\kappa \mu_n^3 L} \cdot (1 - \exp(-\kappa \mu_n^2 \Delta t_k)). \end{aligned}$$

At the wall surface,

$$\begin{aligned} \left(\frac{\partial T}{\partial z'} \right)_{z'=L} &= \frac{a + bt'}{L} + \frac{bL}{3\kappa} + \sum_{n=1}^{\infty} W_n \mu_n \cdot (-1)^n \exp(-\kappa \mu_n^2 t') \\ &= \frac{a}{L} + \sum_{n=1}^{\infty} g_n \mu_n \cdot (-1)^n \exp(-\kappa \mu_n^2 t') + b \cdot \left[\frac{t'}{L} + \frac{L}{3\kappa} - \frac{2}{\kappa L} \cdot \sum_{n=1}^{\infty} \frac{1}{\mu_n^2} \exp(-\kappa \mu_n^2 t') \right] \\ &=: C_1(t') + C_2(t') \cdot b. \end{aligned}$$

Here we are only interested in $t' = \Delta t_k$. Thus $C_1(\Delta t_k), C_2(\Delta t_k)$ are locally fixed in time step k and, as a response to a new b -value from the melt model, the updating computational work of

$$q_{surf} = \lambda_w \cdot \left(\frac{\partial T}{\partial z'} \right)_{z'=L} \text{ becomes a linear operation only.}$$

The $C_1(t')$ -series converges absolutely for every $t' > 0$, irrespectively of $g(z')$, and the $C_2(t')$ -series converges absolutely for every $t' \geq 0$. At the front, as T measures the

temperature above T_E , then $a \approx T_l - T_E \gg 0$, and $f(z') \equiv 0$. Here $g_n = \frac{2(-1)^n}{\mu_n L} \cdot a$, and the

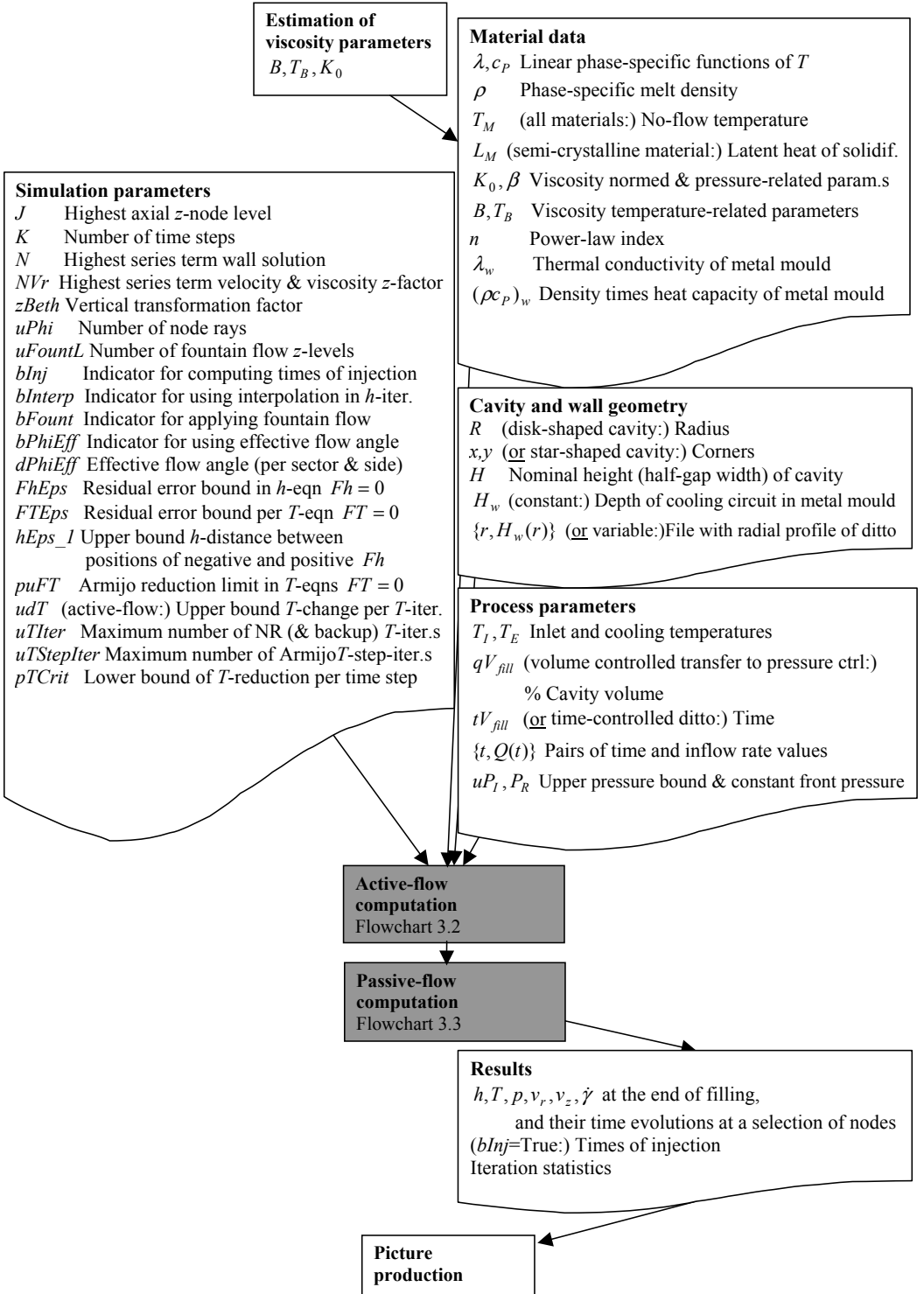
$C_1(t')$ -series diverges at $t' = 0$, due to infinite initial heat flux. In this case, $\frac{2C_1}{a} \cdot t' = C_2$

holds in general. This means that $\left(\frac{\partial T}{\partial z'} \right)_{z'=L} = C_2 \cdot \left(\frac{a}{2t'} + b \right) = 0$ is obtained at a time $t' = t'_c$

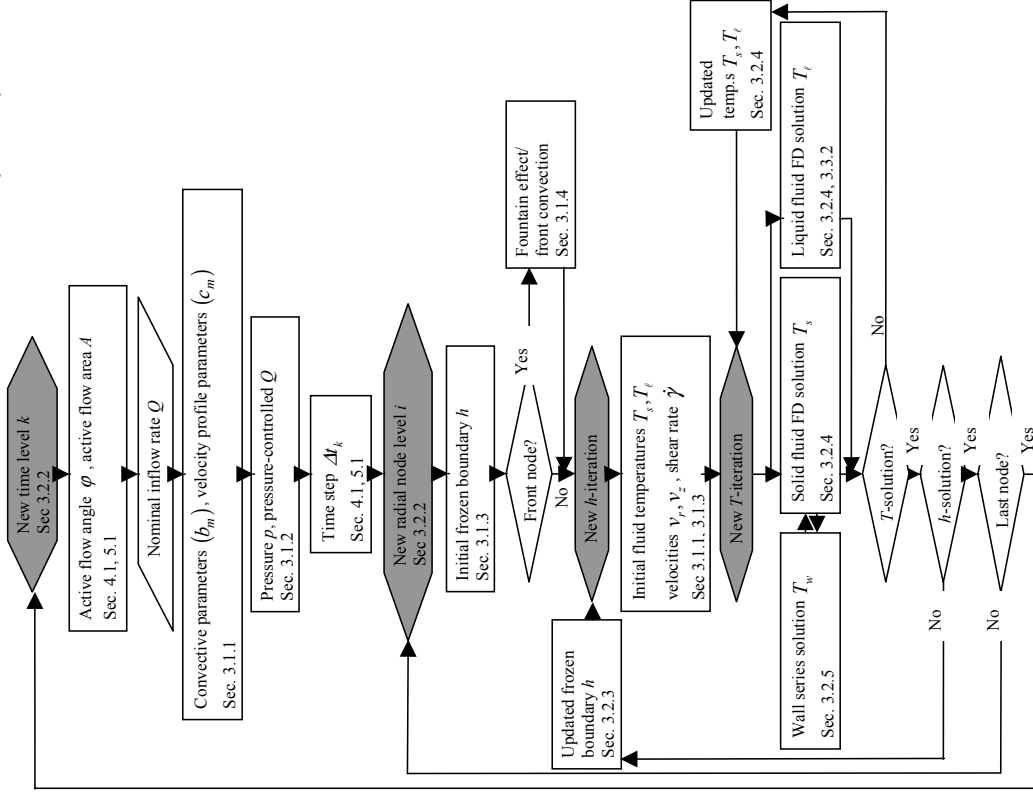
fulfilling $b \cdot t'_c = -\frac{1}{2}a$, i.e. when the initial temperature difference between melt and wall is halved. If necessary, because of the basic linear approximation of flux and temperature, the front time step should be subdivided into sub-steps much shorter than t'_c . In practice the sub-step control at the front is activated, if the initial temperature difference melt-wall is reduced by more than a prescribed percentage during Δt_k . Behind the front, since $a = f(L)$, i.e. $g(L) = 0$, the $C_1(t')$ -series is expected to converge rapidly also at $t' = 0$.

To cope with the singularity for $t' = 0$ at the front, i.e. when the hot melt meets the cold metal, an improved initial time-substep is described in **App. 2**, where we replace the slowly converging series solution by an analytical square-root solution, according to **Sec. 3.1.3**.

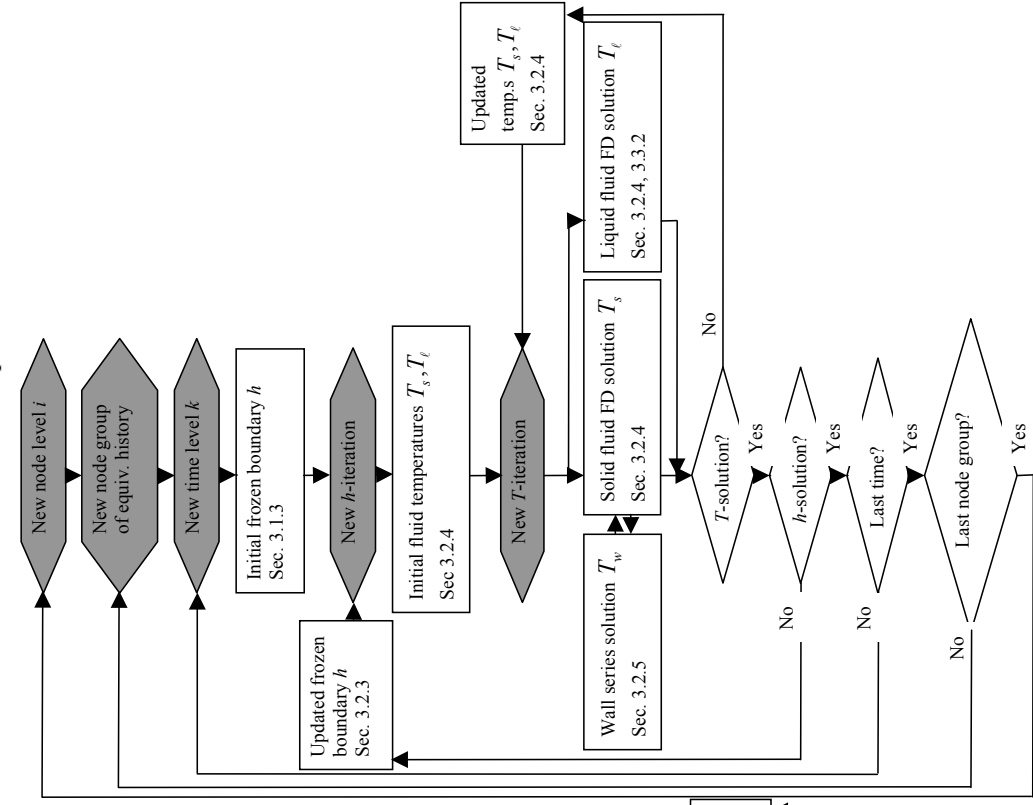
Flowchart 3.1 Data processing.



Flowchart 3.2 Solution routine for active flow. Radial symmetry.



Flowchart 3.3 Solution routine for passive flow.



3.3 FD scheme

In this **Section** the FD-scheme is derived and examined. The discretization of the PDE (3.11) is made by control volumes in **Sec 3.3.1**, in such a way that truncation errors become small. Several potential FD schemes have been investigated in this project, but this thesis describes a time-implicit scheme only. Since the temperature is expected to fall rapidly near the cavity wall, the density of the gap-wise (axial), discrete node levels should increase towards the wall, and the transformation we find does not reduce the order of accuracy. Another principle is to base our discretization upon a conservative form of the PDE, in consideration of phase-specific, linear heat capacity and conductivity functions of temperature, according to our conclusions in **Sec. 2.2.5**. In **Sec. 3.3.2** we investigate the existence and uniqueness of the solution of the discretized problem, and formulate operational conditions for the NR routine to converge. An FD-equation is said to be convergent if its solution approaches the PDE solution as the step sizes tend to 0. For linear and linearized well-posed PDEs in simple geometries, convergence in L^2 -norm of one-step FD-schemes is guaranteed by consistency and stability, according to the Lax-Richtmyer equivalence theorem (e.g., [Strikwerda], p.222). Consistency, i.e. that the truncation error tends to 0 as the step sizes do, is guaranteed by our choice of FD scheme – see **Sec. 3.3.1** – and by the convergence of our FD solution method – see **Sec. 3.3.2**. Stability means that the FD routine does not amplify errors. Although stability of a linearized scheme is no guarantee for overall stability, we investigate such schemes in **Appendix 5**, in order to identify crucial quantities for the nonlinear problem. As for fluid acceleration, the restrictions are similar to the well-posedness conditions in **App. 4**. But the possibility of instabilities due to $h \downarrow 0$ now becomes evident.

3.3.1 Control volume approach and truncation error

Assuming one inlet at $r = 0$, we consider a node O at radius r and a surrounding small cavity volume with radial extension $(r - \frac{1}{2}\Delta r, r + \frac{1}{2}\Delta r)$, axial extension Δz and covering the whole active flow angle φ_{act} , i.e. having the volume measure $\mu_V := \varphi_{act} r \Delta r \Delta z$. The difference between the PDE-terms and the approximating FD-equation terms for one and the same temperature distribution is the truncation error. Consistency now means that the truncation error tends to zero if the step sizes Δr , Δz do. To prepare for an analysis by control volumes, we introduce a local coordinate system (\tilde{r}, \tilde{z}) surrounding node O. The third, angular, dimension is implicit. Also time is implicit in the non-dynamic PDE terms below, since all function evaluations are assumed to take place at the current time, i.e. without time error. The explicit equation at O represents the heat balance within a rectangle (control volume) $n-w-s-e$, the boundaries being placed half ways between O and each of its four neighbour nodes N, W, S and E. The eastward (flow direction) step size Δr is assumed fixed; thus $e = -w =: \Delta r / 2$ and $\Delta r = e - w$. However, the northward (vertical) step size Δz is allowed to vary; thus $n \neq -s (> 0)$ may hold in $\Delta z := n - s (= n + |s|)$. This makes the control volume approach useful, also in representing the energy weight of the corresponding FD-equation, by the volume measure μ_V . The local coordinates (\tilde{r}, \tilde{z}) of the surrounding node points become $N := (0, 2n)$, $W := (-\Delta r, 0)$, $S := (0, 2s)$, $E := (\Delta r, 0)$ – see **Figure 3.2**.

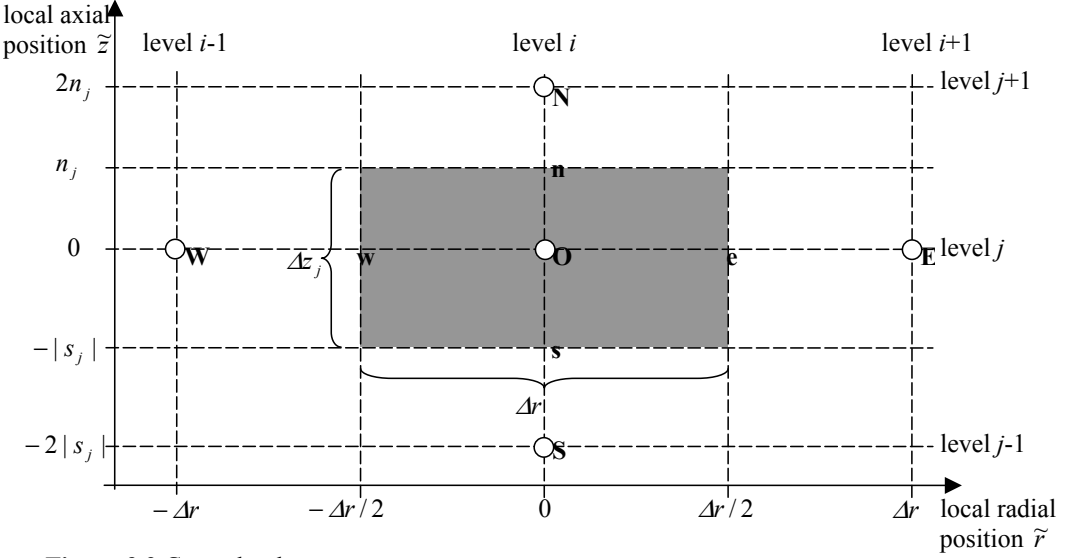


Figure 3.2 Control volume.

First, consider the conduction term of the PDE, represented by

$$I_{cond,PDE} := \int_{-w}^e \int_{-s}^n \frac{\partial}{\partial z} \left(\lambda \frac{\partial T}{\partial z} \right) (r + \tilde{r}) d\tilde{z} d\tilde{r} = \varphi_{act} \cdot \int_{-w}^e \int_{-s}^n \frac{\partial}{\partial z} \left(\lambda \frac{\partial T}{\partial z} \right) d\tilde{z} (r + \tilde{r}) d\tilde{r}.$$

A PDE is said to be in conservative form (see, e.g., [Özisik], p.5), if the coefficients of the derivative terms are constant. Here the conductivity λ (cf. Sec. 2.2.2) is assumed to be a linear function of temperature, $\lambda =: \lambda_0 + \lambda_1 T$. Letting $L(T) := (\lambda_0 + \frac{1}{2} \lambda_1 T) \cdot T$ the integral takes the conservative form

$$I_{cond,PDE} = \varphi_{act} \cdot \int_{-w}^e \int_{-s}^n \frac{\partial^2 L(T)}{\partial z^2} d\tilde{z} (r + \tilde{r}) d\tilde{r} = \varphi_{act} \cdot \int_{-w}^e \left[\left(\frac{\partial L}{\partial z} \right)_n - \left(\frac{\partial L}{\partial z} \right)_s \right] (r + \tilde{r}) d\tilde{r}.$$

In a more general setting, introducing $u(\tilde{r}, \tilde{z}) := \varphi_{act} \cdot (r + \tilde{r}) \cdot \frac{\partial L}{\partial z}$, the integral is of type

$$I_{cond,PDE} = \int_{-w}^e [u(\tilde{r}, n) - u(\tilde{r}, s)] d\tilde{r}.$$

Assume that u is an analytic function of (\tilde{r}, \tilde{z}) in a neighbourhood of $(0,0)$, i.e. of node O.

Then u can be described locally by the power series $u(\tilde{r}, \tilde{z}) =: \sum_{i,j=0}^{\infty} u_{ij} \tilde{r}^i \tilde{z}^j$, convergent for

sufficiently small $|\tilde{r}|, |\tilde{z}|$. Now the integral can be evaluated by termwise integration and use of $e = -w = \Delta r/2$ as

$$\begin{aligned} I_{cond,PDE} &= \sum_{i,j=0}^{\infty} u_{ij} \frac{1}{i+1} (e^{i+1} - w^{i+1}) (n^j - s^j) = \sum_{m=0}^{\infty} \sum_{j=1}^{\infty} u_{2m,j} \frac{\Delta r^{2m+1}}{(2m+1)2^{2m}} [n^j - (-|s|)^j] = \\ &= u_{01} \Delta r \Delta z + u_{02} \Delta r (n^2 - |s|^2) + u_{03} \Delta r (n^3 + |s|^3) + \frac{1}{12} u_{21} \Delta r^3 \Delta z + \dots \end{aligned}$$

where higher order terms of $\Delta r, \Delta z$ are omitted.

If T is analytic at O, then termwise u, T power series identification in

3.3 FD scheme

$$u(\tilde{r}, \tilde{z}) \left(= \varphi_{act} \cdot (r + \tilde{r}) \cdot \frac{\partial L}{\partial z} \right) = \varphi_{act} \cdot (r + \tilde{r}) \cdot \left(\lambda_0 \frac{\partial T}{\partial z} + \lambda_0 T \frac{\partial T}{\partial z} \right)$$

yields

$$u_{ij} = \varphi_{act} r \cdot \left[\lambda_0 \cdot (j+1) T_{i,j+1} + \lambda_1 \cdot \sum_{i'=0}^i \sum_{j'=1}^{j+1} j' \cdot T_{i-i', j+1-j'} T_{i' j'} \right] \\ + \varphi_{act} \cdot \lambda_0 \cdot (j+1) T_{i-1, j+1} + \lambda_1 \cdot \sum_{i'=0}^{i-1} \sum_{j'=1}^{j+1} j' \cdot T_{i-i'-1, j+1-j'} T_{i' j'}$$

In order to cancel the leading term of $I_{cond, PDE}$ by a matching FD-discretization $I_{cond, FD}$ we evaluate and weigh λ , T at N, O, S. The basic approximation is

$$I_{cond, PDE} = \varphi_{act} \cdot \int_w^e \left[\left(\frac{\partial L}{\partial z} \right)_n - \left(\frac{\partial L}{\partial z} \right)_s \right] (r + \tilde{r}) d\tilde{r} \approx \\ \approx \varphi_{act} \cdot \left[\left(\frac{\partial L}{\partial z} \right)_{\tilde{r}=0, n} - \left(\frac{\partial L}{\partial z} \right)_{\tilde{r}=0, s} \right] \cdot \left[r(e-w) + \frac{1}{2}(e^2 - w^2) \right] = \left[\left(\frac{\partial L}{\partial z} \right)_{\tilde{r}=0, n} - \left(\frac{\partial L}{\partial z} \right)_{\tilde{r}=0, s} \right] \cdot \frac{\mu_V}{\Delta z}.$$

Consistent heat flow across the borders between adjacent control volumes is accomplished by using the implicit central difference scheme

$$I_{cond, FD} := \left[\frac{L(T_N) - L(T_O)}{2n} - \frac{L(T_O) - L(T_S)}{2|s|} \right] \cdot \frac{\mu_V}{\Delta z} = \left[\lambda(\hat{T}_n) \frac{T_N - T_O}{2n} - \lambda(\hat{T}_s) \frac{T_O - T_S}{2|s|} \right] \cdot \frac{\mu_V}{\Delta z},$$

where $\hat{T}_n := \frac{1}{2}(T_N + T_O)$, $\hat{T}_s := \frac{1}{2}(T_O + T_S)$. Then

$$I_{cond, PDE} - I_{cond, FD} = -\frac{1}{3} u_{02} \Delta r (n^2 - |s|^2) - u_{03} \Delta r (n^3 + |s|^3) + \frac{1}{12} u_{21} \Delta r^3 \Delta z + \dots$$

If $(n - |s|) / \Delta z^p \rightarrow const \neq 0$ as $\Delta z \rightarrow 0$, i.e. $n - |s| = O(\Delta z^p)$, the error magnitude becomes $\mu_V \cdot O(\Delta r^2 + \Delta z^{\min[p, 2]})$. Hence it is unaffected for $p \geq 2$ (where fixed step size corresponds to $p \rightarrow \infty$). Since the steepest temperature variation occurs at the mould wall and since freezing is in focus, the axial step sizes Δz should decrease towards the wall. Although $p = 1$ serves these demands, including, e.g., any geometric series of diminishing node distances, the disadvantage is a reduced order of accuracy. Instead, we use a transformation from $z \in [0, H]$ to a uniform grid in the computational domain $\zeta \in [0, 1]$, generated by (cf. [Özisik], p.315):

$$\zeta = \frac{\ln A(z)}{\ln B}, \quad A(z) := \frac{\beta + \frac{z}{H}}{\beta - \frac{z}{H}}, \quad B := \frac{\beta + 1}{\beta - 1};$$

where β is a parameter, $\beta > 1$.

The inverse transformation is

$$z = \frac{\beta \cdot (B^\zeta - 1)}{B^\zeta + 1} \cdot H.$$

Here a constant space step $\Delta \zeta$ is applied to the computational domain.

A full transformation means that also the PDE is transformed. However, we prefer to work in z -space – alas a non-constant step size Δz .

The leading transformation derivatives are

$$\zeta'(z) = \frac{1}{H \cdot \ln B \cdot \left[\beta^2 - \left(\frac{z}{H} \right)^2 \right]} = \frac{(B^\zeta + 1)^2}{H \cdot \ln B \cdot \beta^2 \cdot 4B^\zeta} (> 0),$$

$$\zeta''(z) = \frac{2z}{H^3 \cdot \ln B \cdot \left[\beta^2 - \left(\frac{z}{H} \right)^2 \right]^2} = \frac{(B^\zeta + 1)^2 (B^{2\zeta} - 1)}{H^2 \cdot \ln B \cdot \beta^3 \cdot 8B^{2\zeta}}.$$

As for the decisive (dimensioning) p -value we realize that, since $\zeta''(z) > 0$ for $z > 0$ ($\zeta > 0$), $\zeta'(z)$ will increase by z . Hence the critical behaviour is close to the wall surface, where $z = H$, so $\zeta \approx 1$, and consecutive step sizes satisfy

$$n - |s| \rightarrow \frac{(B-1)^2}{8BH} \cdot \Delta z^2 = O(\Delta z^2).$$

Thus $p \geq 2$ everywhere (when $\Delta \zeta \downarrow 0$), and the truncation error is unaffected.

As for the conservative form of the two convection terms, the coefficient ρ_ℓ (cf. **Sec. 2.2.2**) is assumed constant but $c_{P,\ell}$ (cf. **Sec. 2.2.1**) is a linear function of T , $c_{P,\ell} =: c_0 + c_1 T$. Consider the internal energy $U(T) := \rho_\ell (c_0 + \frac{1}{2} c_1 T) \cdot T$ and let \mathbf{v} denote the velocity vector. By the equation of continuity (the fluid is incompressible) the convection terms can be put into the conservative form

$$\begin{aligned} \rho_\ell c_{P,\ell}(T) \cdot \left(v_r \frac{\partial T}{\partial r} + v_z \frac{\partial T}{\partial z} \right) &= \rho_\ell c_{P,\ell}(T) \cdot (\mathbf{v} \cdot \text{grad} T) = \\ &= U(T) \cdot \text{div} \mathbf{v} + \mathbf{v} \cdot \text{grad} U(T) = \text{div}[\mathbf{v} U(T)] \end{aligned}$$

By use of Gauss's theorem the corresponding PDE-integral on the control volume can be written

$$I_{\text{conv},PDE} = \varphi_{\text{act}} \cdot \int_s^n \left\{ [(r + \tilde{r}) v_r U]_e - [(r + \tilde{r}) v_r U]_w \right\} d\tilde{z} + \varphi_{\text{act}} \cdot \int_w^e \left\{ [v_z U]_n - [v_z U]_s \right\} (r + \tilde{r}) d\tilde{r}.$$

By letting $u(\tilde{r}, \tilde{z}) := \varphi_{\text{act}} \cdot (r + \tilde{r}) \cdot v_r U$, bounded for $v_r \propto 1/(r + \tilde{r})$ if $r + \tilde{r} \rightarrow 0$, the first integral of $I_{\text{conv},PDE}$ becomes

$$I_{\text{conv1},PDE} := \int_s^n \{ u(e, \tilde{z}) - u(w, \tilde{z}) \} d\tilde{z}.$$

In a standard up-winding FD-scheme $I_{\text{conv1},PDE}$ is approximated (cf. **Fig. 3.2**) by

$$I_{\text{conv1},FD} := (u_O - u_w) \Delta z.$$

Assuming a series expansion $u(\tilde{r}, \tilde{z}) =: \sum_{i,j=0}^{\infty} u_{ij} \tilde{r}^i \tilde{z}^j$, the error becomes

$$\begin{aligned} I_{\text{conv1},PDE} - I_{\text{conv1},FD} &= \sum_{m,j=0}^{\infty} u_{2m+1,j} \frac{\Delta r^{2m+1}}{2^{2m}} \cdot \frac{n^{j+1} - (-|s|)^{j+1}}{j+1} + \sum_{i=1}^{\infty} u_{i0} (-\Delta r)^i \Delta z = \\ &= u_{20} \Delta r^2 \Delta z - \frac{3}{4} u_{30} \Delta r^3 \Delta z + \frac{1}{2} u_{11} \Delta r (n^2 - |s|^2) + \dots = \mu_r \cdot O(\Delta r + \Delta z^{\min[p,2]}). \end{aligned}$$

If we let $u(\tilde{r}, \tilde{z}) := \varphi_{\text{act}} \cdot (r + \tilde{r}) \cdot v_z U$, the second integral of $I_{\text{conv},PDE}$ turns into

3.3 FD scheme

$$I_{conv2,PDE} := \int_w^e \{u(\tilde{r}, n) - u(\tilde{r}, s)\} d\tilde{r}.$$

It resembles the final conduction integral $I_{cond,PDE}$, but now the integrand u can be evaluated at N, O, S without further discretization error. We implement the “central” difference scheme (cf. **Fig. 3.2**)

$$I_{conv2,FD} := \frac{1}{2}(u_N - u_S)\Delta r,$$

with a truncation error of order $\mu_V \cdot O(\Delta r^2 + \Delta z^{\min[p,2]})$.

Now consider the viscosity source term $I_{visc,PDE}$. By introducing $u(\tilde{r}, \tilde{z}) := \varphi_{act} \cdot (r + \tilde{r}) \cdot \eta \dot{\gamma}^2$ for the integrand, we get

$$I_{visc,PDE} := \int_s^e \int_w^e u(\tilde{r}, \tilde{z}) d\tilde{r} d\tilde{z} = \sum_{m,j=0}^{\infty} u_{2m,j} \frac{\Delta r^{2m+1}}{(2m+1)2^{2m}} \cdot \frac{n^{j+1} - (-|s|)^{j+1}}{j+1}.$$

If discretization is made at node O, i.e. an implicit 1-point scheme

$$I_{visc,FD} := u_O \Delta r \Delta z,$$

the corresponding error magnitude is $\mu_V \cdot O(\Delta r^2 + \Delta z^{\min[p,2]})$.

The time-dependent term is expressed in conservative form by $U(T)$ and

$$\frac{\partial U(T)}{\partial t} = \frac{\partial}{\partial t} [\rho_\ell (c_0 + \frac{1}{2} c_1 T) T] = \rho_\ell (c_0 + c_1 T) \frac{\partial T}{\partial t} = \rho_\ell c_{P,\ell}(T) \frac{\partial T}{\partial t}$$

as

$$I_{dyn,PDE} := \varphi_{act} \cdot \int_s^e \int_w^e \rho_\ell c_{P,\ell} \frac{\partial T}{\partial t} \cdot (r + \tilde{r}) d\tilde{r} d\tilde{z} = \varphi_{act} \cdot \int_s^e \int_w^e \frac{\partial U}{\partial t} \cdot (r + \tilde{r}) d\tilde{r} d\tilde{z},$$

which is of the same form as $I_{visc,PDE}$ and the results above apply. If node O takes index values (i, j, k) , $k =$ current time level, then the standard backward-time approximation is

$$\frac{\partial U}{\partial t} \approx \frac{U(T_{ij}^k) - U(T_{ij}^{k-1})}{\Delta t_k} =: \frac{\Delta U}{\Delta t_k}.$$

Apart from the spatial truncation error, this adds a further term $\mu_V \cdot O(\Delta t_k + \dots)$.

Let us summarize the general FD scheme for the liquid phase ℓ of streaming fluid. In the system of equations, the control volume weights μ_V differ only by Δz . Therefore the weighted FD equation, that corresponds to PDE (3.12) or (3.11), is written

$$\begin{aligned} \Delta z \cdot \frac{\Delta U}{\Delta t} + \frac{\Delta z}{\Delta r} \cdot \left[(v_r U)_O - (v_r U)_W \cdot \left(1 - \frac{\Delta r}{r} \right) \right] + \frac{1}{2} \cdot [(v_z U)_N - (v_z U)_S] = \\ = \lambda(\hat{T}_n) \cdot \frac{T_N - T_O}{2n} - \lambda(\hat{T}_s) \cdot \frac{T_O - T_S}{2|s|} + \Delta z \cdot \eta \dot{\gamma}^2. \end{aligned} \quad (3.15)$$

The FD-scheme has to be modified at the boundaries (cf. **Sec. 2.4.1**): At the mould (cavity wall) surface $z = H$ the northern conduction term of $I_{cond,FD}$ is replaced by the heat flux taken from the wall solution, and the two convection terms by $I_{conv1,FD} = 0$ (no-slip $v_r = 0$)

and $I_{conv2,FD} = \Delta r \Delta z \cdot (u_o - u_s) / 2 |s|$, respectively.

At the surface of the frozen layer $z = h(\mathbf{r}, t)$, regarded as the local position n for the last node O in the liquid phase, the northern conduction term is based upon temperature T_M as

$$\left(\frac{\partial L}{\partial z} \right)_{n/2} \approx \frac{L(T_M) - L(T_o)}{n}$$

and the heat flux across h is extrapolated as

$$\left(\frac{\partial L}{\partial z} \right)_n \approx \left(\frac{\partial L}{\partial z} \right)_{n/2} + \left[\left(\frac{\partial L}{\partial z} \right)_{n/2} - \lambda(\hat{T}_s) \frac{T_o - T_s}{2 |s|} \right] \cdot \frac{n/2}{n/2 + |s|},$$

and the vertical convection term is replaced by $(v_z U)_n - \frac{1}{2} \cdot [(v_z U)_o - (v_z U)_s]$.

For converging tapered flow the radial convection I_{conv1} is approximated as above, but for expanding tapered flow and nodes O with z close to h , $I_{conv1,FD}$ is exchanged for an upwind-ing from the radial position between W and O where h hits vertical level z (i.e. where $v_r = 0$).

The symmetry (middle) plane node $z_0 = 0$ is regarded as the centre of a control volume between $n = z_1/2$ and $s = z_{-1}/2 = -n$, where $z_{-1} = -z_1$ is a fictitious, symmetrically placed node. The symmetry conditions (cf. Sec 2.4.1) mean $\frac{\partial T}{\partial z} = 0$, $\frac{\partial v_z}{\partial z} = 0$ at z_0 , and

$T(z_1) = T(z_{-1})$, $v_z(z_1) = -v_z(z_{-1})$ etc. By applying the ordinary FD-scheme at z_0 , with halved weight, the order of accuracy will not decrease (cf. [Özisik], p.47).

The first radial node level has radius $r = \Delta r$ and the preceding node level corresponds to the inlet, with a cylindrical extension of radius $\frac{1}{2} \Delta r$.

The general FD schemes for phase ℓ of stagnant fluid and for the solid phase s of streaming as well as stagnant fluid are simplifications of (3.15) – without the convective and viscous energy terms.

3.3.2 Convergence of inner iterations

In Sec 3.3.1 we introduced the notations $\hat{T}_n := \frac{1}{2}(T_N + T_o)$, $\hat{T}_s := \frac{1}{2}(T_o + T_s)$ and $U(T) := \rho_\ell (c_0 + \frac{1}{2} c_1 T) \cdot T$, where $c_{p,\ell} := c_0 + c_1 T$. Denote the diffusivity of the liquid phase by $\kappa_\ell(T) := \lambda_\ell(T) / \rho_\ell c_{p,\ell}(T)$. The FD-character becomes more obvious if we divide the weighted FD equation (3.15) by Δz , to get an unweighted equation of finite differences for the internal energy $U(T)$:

$$\begin{aligned} \frac{\Delta U}{\Delta t} + \frac{1}{\Delta r} \cdot \left[(v_r U)_o - (v_r U)_w \cdot \left(1 - \frac{\Delta r}{r} \right) \right] + \frac{1}{2 \Delta z} \cdot [(v_z U)_N - (v_z U)_s] \\ - \frac{1}{\Delta z} \cdot \left[\kappa_\ell(\hat{T}_n) \cdot \frac{U_N - U_o}{2n} - \kappa_\ell(\hat{T}_s) \cdot \frac{U_o - U_s}{2 |s|} \right] = \eta \gamma^2. \end{aligned}$$

Here the temperature T is uniquely determined from U as

$$T = (2U / \rho_\ell) / \left(c_0 + \sqrt{c_0^2 + 2c_1 U / \rho_\ell} \right).$$

To emphasize the discrete character of the equation, replace the local node notations O etc. by indices – radial level i , vertical level j and time level k , as follows

3.3 FD scheme

$$U_{ij}^k := U(T_{ij}^k), \quad T_{ij}^k := T(r_i, z_j, t_k).$$

During an h -iteration, a trial value of the frozen layer surface $h = h(r_i, t_k)$ is fixed. Then v_r, v_z and $\dot{\gamma}$ become locally fixed, but η and (maybe) κ_ℓ depend upon T . The upper index k is used to mark this implicitly for η , κ_ℓ , making the (unweighted) FD equation nonlinear:

$$\begin{aligned} & \frac{U_{ij}^k - U_{ij}^{k-1}}{\Delta t_k} + \frac{v_{r,ij} U_{ij}^k - v_{r,i-1,j} (1 - \Delta r / r_i) U_{i-1,j}^k}{\Delta r} + \frac{v_{z,i,j+1} U_{i,j+1}^k - v_{z,i,j-1} U_{i,j-1}^k}{2 \Delta z_j} \\ & - \frac{1}{\Delta z_j} \cdot \left[\kappa_{\ell,i,j+1/2}^k \cdot \frac{U_{i,j+1}^k - U_{ij}^k}{2 n_j} - \kappa_{\ell,i,j-1/2}^k \cdot \frac{U_{ij}^k - U_{i,j-1}^k}{2 |s_j|} \right] = \eta_{ij}^k \cdot (\dot{\gamma}_{ij}^k)^2. \end{aligned} \quad (3.16)$$

In the inner iterative procedure for the active-flow cavity region a system of $J+1$ equations of type (3.16) is solved for $(U_{ij}^k)_{j=0}^J$ (in reality for $(T_{ij}^k)_{j=0}^J$), subdivided into two disjoint sets, of liquid and solid fluid, modified at the boundaries and simplified in the solid phase. In each phase of state let the system be written $\mathbf{f} = \mathbf{0}$ (LHS – RHS of (3.16)). An iteration of the Newton-Raphson (NR) method means that the vector \mathbf{T} of T -variables is changed by an amount \mathbf{u} satisfying $\mathbf{G}\mathbf{u} = -\mathbf{f}$, where \mathbf{f} and the tri-diagonal Jacobian matrix \mathbf{G} are evaluated at the current \mathbf{T} -iterate. Here Thomas's algorithm, i.e. simple LU-factorization (e.g., [Özsisik], p.50) is well suited, producing the solution \mathbf{u} by $O(J)$ operations. For the solid phase and for the whole passive-flow region of the cavity, the viscous energy term disappears. Then if κ does not depend upon temperature, \mathbf{G} becomes constant, i.e. (3.16) is just a set of linear equations (and only one NR-iteration is needed).

For the general iterative procedure to be well-defined, \mathbf{G} needs to be non-singular. We will show that \mathbf{G} is strictly diagonally dominant. Let the liquid phase correspond to the vertical levels $j \in [0, jh]$, with weights $\Delta z_j = n_j + |s_j|$, $n_j \leq |s_j|$.

Moreover, let $a_{N,j} := \frac{1}{2} \cdot \left(\frac{\kappa_\ell(T_{ij}^k)}{n_j} + v_{z,ij} \right)$, $a_{S,j} := \frac{1}{2} \cdot \left(\frac{\kappa_\ell(T_{ij}^k)}{|s_j|} - v_{z,ij} \right)$. We focus on the general expression, i.e. $0 < j < jh$. The three non-zero elements in \mathbf{G} -row j are

$$\begin{aligned} G_{j,j-1} &= -\rho_\ell c_{P,\ell}(T_{i,j-1}^k) \cdot a_{N,j-1} \\ G_{jj} &= \rho_\ell c_{P,\ell}(T_{ij}^k) \cdot \left[\Delta z_j \left(\frac{1}{\Delta t_k} + \frac{v_{r,ij}}{\Delta r} + \frac{\eta_{ij}^k \dot{\gamma}_{ij}^2}{\rho_\ell c_{P,\ell}(T_{ij}^k)} \cdot \frac{B}{(T_{ij}^k - T_B)^2} \right) + a_{N,j} + a_{S,j} \right] \\ G_{j,j+1} &= -\rho_\ell c_{P,\ell}(T_{i,j+1}^k) \cdot a_{S,j+1} \end{aligned}$$

Assume that conduction dominates over vertical convection, in the sense that $a_N, a_S > 0$. This is a numerical and not a physical restriction, since it can be accomplished by sufficiently small step lengths $(\Delta z_j)_{j=0}^{jh}$ in any temperature region of interest. Now all the terms of G_{jj} are positive, since $v_{r,ij} > 0$ (upwinding) and $B > 0$ (Arrhenius factor for real materials, cf. (2.4)). The non-zero elements in column j fulfil

$$|G_{jj}| - |G_{j-1,j}| - |G_{j+1,j}| = \rho_\ell c_{P,\ell}(T_{ij}^k) \cdot \Delta z_j \left(\frac{1}{\Delta t_k} + \frac{v_{r,ij}}{\Delta r} + \frac{\eta_{ij}^k \dot{\gamma}_{ij}^2}{\rho_\ell c_{P,\ell}(T_{ij}^k)} \cdot \frac{B}{(T_{ij}^k - T_B)^2} \right) > 0.$$

Therefore \mathbf{G} is an M-matrix ([Ortega], p.223), strictly (and irreducibly) diagonally dominant.

Hence (e.g., [Ortega & Rheinboldt], p.48) \mathbf{G} is invertible with $\mathbf{G}^{-1} > \mathbf{0}$, and the NR-iterates are well-defined. Since the diagonal \mathbf{G} -elements are positive, the diagonal dominance also ensures that the eigenvalues have a positive real part. The temperature vector $\mathbf{T} := (T_{ij}^k)_{j=0}^{jh}$ varies in an open, convex set $D_T \subset R^{jh+1}$, $D_T := \{\mathbf{T} \in R^{jh+1} \mid T_B + \varepsilon < T_{ij}^k < T_\infty, \forall j\}$, where T_B is defined in (2.4), and $\varepsilon(> 0)$, T_∞ are artificial bounds. Now ([ibid.], p.143) $\mathbf{T} \rightarrow \mathbf{f}$ is a one-to-one mapping in D_T , and $\mathbf{f} = \mathbf{0}$ has at most one solution in D_T . We want to show that a solution always exists, or else that unacceptably high or low temperatures (above T_∞ or below $T_B + \varepsilon$) can be identified. Through a variable transformation – the mapping $\mathbf{T} \rightarrow \mathbf{V}$, $T_{ij}^k := T_B + e^{V_j}$, i.e. $V_j := \ln(T_{ij}^k - T_B)$ – the new variable vector $\mathbf{V} := (V_j)_{j=0}^{jh}$ defines a new mapping $\mathbf{V} \rightarrow \tilde{\mathbf{f}}$, $\tilde{\mathbf{f}}(\mathbf{V}) := \mathbf{f}(\mathbf{T}(\mathbf{V}))$ in the open, convex set $D_V := \{\mathbf{V} \in R^{jh+1} \mid V_B < V_j < V_\infty, \forall j\}$, where $V_B := \ln \varepsilon$, $V_\infty := \ln(T_\infty - T_B)$. In theory, $\varepsilon = 0$ and $T_\infty = +\infty$, i.e. $V_B := -\infty$ and $V_\infty := +\infty$, are possible. In case $\kappa_\ell(T)$ and/or $c_{P,\ell}(T)$ are strictly decreasing functions of T , the positivity constraints $a_N, a_S > 0$ will imply a theoretical bound $T_\infty < +\infty$. In practice, the acceptable temperatures of the filling phase are far below the zeroes of $\kappa_\ell(T)$, $c_{P,\ell}(T)$ and any application that leads to a solution above these practical acceptance limits should be interpreted as non-solvable. The Jacobian $\tilde{\mathbf{G}}(\mathbf{V})$ of $\tilde{\mathbf{f}}(\mathbf{V})$ satisfies $\tilde{\mathbf{G}}(\mathbf{V}) = \mathbf{G}(\mathbf{T}(\mathbf{V})) \text{Diag}(e^{V_j})$, i.e. with $\beta := \rho_\ell \cdot \min[c_{P,\ell}(T_B + \varepsilon), c_{P,\ell}(T_\infty)] \cdot \frac{\Delta z_j}{\Delta t_k}$ the non-zero elements in column j fulfil

$$\begin{aligned} & |\tilde{G}_{jj}| - |\tilde{G}_{j-1,j}| - |\tilde{G}_{j+1,j}| = e^{V_j} \cdot (|G_{jj}| - |G_{j-1,j}| - |G_{j+1,j}|) > \\ & > \beta e^{V_j} + \Delta z_j \eta_{ij}^k \gamma_{ij}^2 B e^{-V_j} \geq 2\sqrt{\beta \Delta z_j \eta_{ij}^k \gamma_{ij}^2 B} =: \alpha_j \end{aligned}$$

This lower bound $\alpha_j(> 0)$ is well-defined whenever $\varepsilon < \sqrt{\Delta z_j \eta_{ij}^k \gamma_{ij}^2 B} / \beta < e^{V_\infty}$. Thus $\tilde{\mathbf{f}}(\mathbf{V})$ is uniformly monotone in D_V . For $V_B := -\infty$, $V_\infty := +\infty$ ([ibid.], p.143) $\tilde{\mathbf{f}}$ is a homeo-morphism of R^{jh+1} onto R^{jh+1} , and $\tilde{\mathbf{f}}(\mathbf{V}) = \mathbf{0}$, i.e. $\mathbf{f}(\mathbf{T}(\mathbf{V})) = \mathbf{0}$, has exactly one solution \mathbf{T} .

In order to apply the Newton-Mysovskii Theorem ([ibid.], p.412) we have to show that (i): \mathbf{G} satisfies a Lipschitz condition, and (ii): $\|\mathbf{G}^{-1}\|$ is bounded above, for some norm.

Property (i) follows at once, since we realize that \mathbf{f} is twice-continuously differentiable.

To verify (ii) we start by showing that $\|\mathbf{G}\|$ is bounded below. Take $\alpha := \frac{1}{\varepsilon} \cdot \min_{j \in [0, jh]} \alpha_j$ and let

$|\lambda(\mathbf{G})|_{\min}$ denote the smallest absolute eigenvalue of \mathbf{G} . Now since all diagonal elements $\{G_{jj}\}$ are real and positive, the Gersgorin Circle Theorem ([ibid.], p.49) yields $|\lambda(\mathbf{G})|_{\min} \geq \alpha$ in D_T .

The L^2 -norm of the real matrix \mathbf{G} is $\|\mathbf{G}\|_2 := \sup_{\|\mathbf{x}\|_2=1} \|\mathbf{G}\mathbf{x}\|_2 = \sqrt{\lambda_{\max}(\mathbf{G}^T \mathbf{G})}$. This is the largest

singular value of \mathbf{G} , satisfying ([Horn & Johnson], p.176) $\sqrt{\lambda_{\max}(\mathbf{G}^T \mathbf{G})} \geq |\lambda(\mathbf{G})|_{\max}$.

Hence we get a positive lower norm bound in D_T ,

$$\|\mathbf{G}\|_2 \geq |\lambda(\mathbf{G})|_{\max} \geq |\lambda(\mathbf{G})|_{\min} \geq \alpha.$$

3.3 FD scheme

Next we will use this lower bound to derive a general upper bound for $\|\mathbf{G}^{-1}\|_2$.

The L^2 -norm of \mathbf{G}^{-1} is $\|\mathbf{G}^{-1}\|_2 = \sqrt{\lambda_{\max}((\mathbf{G}^T \mathbf{G})^{-1})} = 1/\sqrt{\lambda_{\min}(\mathbf{G}^T \mathbf{G})}$.

The products of all eigenvalues and all singular values, respectively, satisfy ([ibid.], p.171)

$$(|\det \mathbf{G}| =) \prod_{j=0}^{jh} \sqrt{\lambda_j(\mathbf{G}^T \mathbf{G})} = \left| \prod_{j=0}^{jh} \lambda_j(\mathbf{G}) \right|.$$

Hence

$$(\|\mathbf{G}\|_2)^{jh} \cdot \sqrt{\lambda_{\min}(\mathbf{G}^T \mathbf{G})} = \left(\sqrt{\lambda_{\max}(\mathbf{G}^T \mathbf{G})} \right)^{jh} \cdot \sqrt{\lambda_{\min}(\mathbf{G}^T \mathbf{G})} \geq \prod_{j=0}^{jh} \sqrt{\lambda_j(\mathbf{G}^T \mathbf{G})} = \left| \prod_{j=0}^{jh} \lambda_j(\mathbf{G}) \right| \geq \alpha^{jh+1}$$

and finally

$$\|\mathbf{G}^{-1}\|_2 = 1/\sqrt{\lambda_{\min}(\mathbf{G}^T \mathbf{G})} \leq (\|\mathbf{G}\|_2)^{jh} / \alpha^{jh+1} =: M, \quad (3.17)$$

a general upper norm bound. This shows property (ii).

(In particular, if we assume that \mathbf{G} is normal, i.e. (e.g., [Meyer], p.547) has a complete set of $jh+1$ orthonormal eigenvectors $\{\mathbf{z}_j\}$, corresponding to the eigenvalues $\{\lambda_j\}$, then any unit

length eigenvector \mathbf{z} , corresponding to $\lambda_{\min}(\mathbf{G}^T \mathbf{G})$, can be written $\mathbf{z} = \sum_{j=0}^{jh} p_j \mathbf{z}_j$ with

$1 = \mathbf{z}^* \mathbf{z} = \sum_{j=0}^{jh} |p_j|^2$, where \mathbf{z}^* denotes the transposed complex conjugate of \mathbf{z} . We get

$$\begin{aligned} \lambda_{\min}(\mathbf{G}^T \mathbf{G}) &= \lambda_{\min}(\mathbf{G}^T \mathbf{G}) \cdot \mathbf{z}^* \mathbf{z} = \mathbf{z}^* \mathbf{G}^T \mathbf{G} \mathbf{z} = (\mathbf{G} \mathbf{z})^* \mathbf{G} \mathbf{z} = \\ &= \left(\sum_j \lambda_j p_j \mathbf{z}_j \right)^* \sum_j \lambda_j p_j \mathbf{z}_j = \sum_j |\lambda_j|^2 |p_j|^2 \geq \alpha^2 \cdot \sum_j |p_j|^2 = \alpha^2 \cdot 1 \end{aligned}$$

and receive the stronger bound $\|\mathbf{G}^{-1}\|_2 \leq 1/\alpha =: M$ in D_T .

Now if the first NR-iterate $\mathbf{T}_{(0)}$ is chosen such that the start direction $\mathbf{u}_{(0)} := -\mathbf{G}^{-1}(\mathbf{T}_{(0)}) \mathbf{f}(\mathbf{T}_{(0)})$ has a sufficiently small norm, then the Newton-Mysovskii Theorem guarantees that the iterates converge to the unique solution. In practice, as a security measure (see **Sec. 3.2.4**) we evaluate the objective function $F := \mathbf{f}^T \mathbf{f}$, and use the damped Newton method if necessary. According to [Dennis & Schnabel], p.121, the problem properties imply that the damped NR iterations k lead to $\mathbf{f}(\mathbf{T}_{(k)}) = \mathbf{0}$ for some $k \geq 0$, or

$$\lim_{k \rightarrow \infty} \frac{\nabla F(\mathbf{T}_{(k)})^T \mathbf{u}_{(k)}}{\|\mathbf{u}_{(k)}\|_2} = 0.$$

The directional derivative satisfies, using inequality (3.17),

$$\frac{|\nabla F^T \mathbf{u}|}{\|\mathbf{u}\|_2} = \frac{2\|\mathbf{f}\|_2^2}{\|\mathbf{G}^{-1} \mathbf{f}\|_2} \geq \frac{2\|\mathbf{f}\|_2^2}{\|\mathbf{G}^{-1}\|_2 \|\mathbf{f}\|_2} \geq \frac{2\|\mathbf{f}\|_2}{M},$$

i.e. it tends to 0 only if $\|\mathbf{f}\|_2$ does, and not because ∇F and \mathbf{u} are orthogonal. Thus the inner iterative procedure converges globally to a solution of $\mathbf{f} = \mathbf{0}$, irrespectively of starting point.

In theory we have to accept that the bounds $T_B + \varepsilon$, T_∞ may be violated during the iteration process, before the solution is found.

4 Application: Circular plate

Our method has been implemented for two different applications. The first type, disk shaped cavities, is studied in this **Chapter**. In **Sec. 4.1** we are modelling the disk flow. The discrete time steps are chosen such that the radial expansion per step becomes constant. A time step is primarily determined from the (prescribed) inflow rate and the volume to fill, but we also consider the shrinkage effect that solidification has upon the volume to fill, due to a density variation by temperature. In a true circular case a front expansion rate according to the distance model is uncontroversial. In **Sec. 4.2** two specific materials, one amorphous polycarbonate (PC) and one semi-crystalline polyethylene (HDPE) are modelled. Data for the two materials come from the data base of the FEM-FD-program Moldflow (of Moldflow Corp.). We have made a somewhat critical comment on the Moldflow PVT, 2nd order viscosity and enthalpy models. Unlike the 3D-capacity of Moldflow in modelling mould cavity and metal mould, we rely on a 2D flow model and a 1D cooling model, describing the distance from the cavity wall surface to the cooling lines as radially varying only. In **Sec. 4.3** the comparison runs, two of each material, are discussed. The Moldflow modelling and runs have been performed by [Valtonen]. First the time evolution of pressure is studied. We have tried both the isothermal viscosity model and the extension described in **Sec 3.1.2**. Next the temperatures are investigated, as to time evolution as well as radial distribution and vertical profile at the end of filling. Our two front models are compared, and as an alternative a constant depth of the cooling lines is tried. Finally the radial profiles of the frozen layer (no-flow temperature isotherm) at the end of filling are evaluated. In **Sec. 4.4** we are investigating whether our built-in, more advanced material models have any visible effect upon the basic HDPE run. In this respect a latent heat of crystallisation and a phase-specific linear heat capacity, a phase-specific linear heat conductivity and a pressure dependent viscosity are evaluated. In **Sec. 4.5** some aspects of the method performance are documented, primarily the number of outer (h) and inner (T) iterations, and their relation to the number of vertical node levels.

4.1 Special modelling: Radial flow

Because of the expansion of the frozen layer, the radial flow has a vertical component compensating for the contraction due to solidification (as $\rho_s > \rho_\ell$). When radial level i of time level k is treated numerically, by the method of radial marching, the vertical expansion $-\Delta h_i^k$ (h denotes non-frozen height) of the frozen layer at the preceding radial levels $i'=1, \dots, i-1$ during Δt_k is known. If the phase-change factor (cf. **Sec. 3.1.3**) is denoted $\alpha := \rho_s / \rho_\ell - 1$ and $\bar{\varphi}_k$ is the average active flow angle during Δt_k (with $\bar{\varphi}_k = 2\pi$ in the circular application), then the “lost” liquid volume up to i is

$$q_{i-1}^k := - \sum_{i'=1}^{i-1} \alpha \cdot 2\Delta h_{i'}^k \cdot \bar{\varphi}_k r_{i'} \Delta r.$$

To estimate a nominal mean radial velocity, the melt at i is assumed to move radially from $r_i - d/2$ to $r_i + d/2$, where the local distance d is given by the inflow rate Q_k and

$$Q_k \Delta t_k - q_{i-1}^k = \bar{\varphi}_k \cdot 2h_i^{k-1} r_i d.$$

The nominal velocity becomes

$$\bar{v}_{r,i}^k := \frac{d}{\Delta t_k} = \frac{Q_k - q_{i-1}^k / \Delta t_k}{\bar{\varphi}_k \cdot 2h_i^{k-1} r_i}.$$

In our time-implicit implementation $\bar{v}_{r,i}^k$ is based upon q_i^k, h_i^k instead of q_{i-1}^k, h_{i-1}^{k-1} .

Analogously, the front position is corrected (afterwards). During Δt_k the front is expected to expand from $r_k - \Delta r/2$ to $r_k + \Delta r/2$, by filling an area ΔA_k . The “lost” liquid volume of the previous time level $k-1$ is considered when the new time step Δt_k is determined by the nominal half-width H and

$$Q_k \Delta t_k = 2H \cdot \Delta A_k + q_{k-1}^{k-1}.$$

After that, the rate is corrected to measure the filling of new area exclusively,

$$Q_k := Q_k - q_{k-1}^{k-1} / \Delta t_k.$$

4.2 Materials data

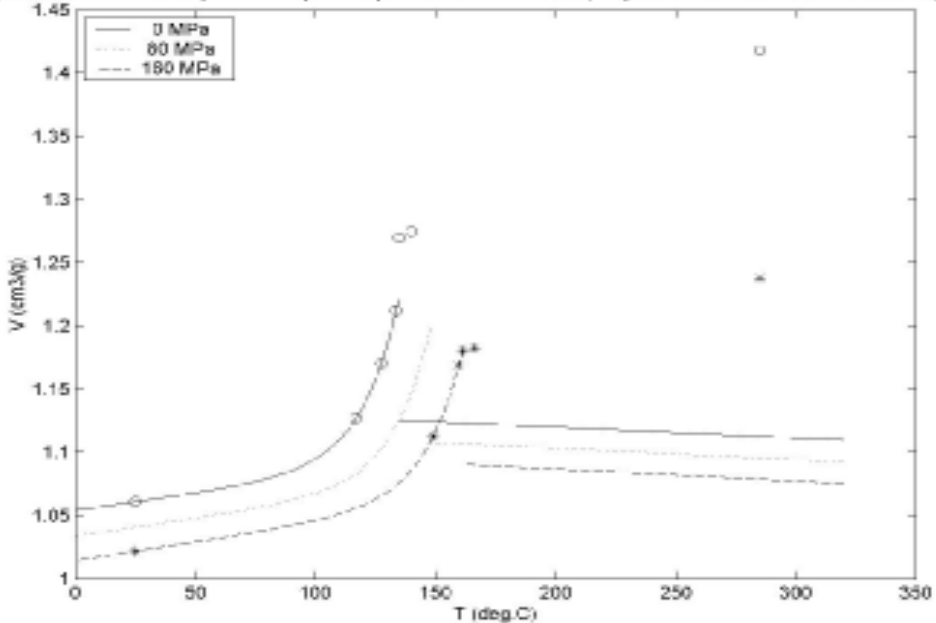
Simulation runs for comparison have been performed by [Valtonen], using the commercial software **Moldflow** of Moldflow Corp., version 2.0.1. From the Moldflow (“**Mfl**” below) data base of standard materials, one amorphous thermoplastic – the polycarbonate Makrolon 2205 of Bayer AG (“**PC**” below) – and one semi-crystalline material – the high density polyethylene Lupolen 5031 L of Basf AG (“**HDPE**” below) – were (arbitrarily) chosen. One run of normal processing conditions (“**warm**” below) and one of low temperature filling (“**cold**” below) were simulated for each material. The circular cavity radius was chosen extreme (40 cm) to provoke freezing. The plate thickness is 3 mm and the inlet is (unintentionally) 1.5 cm from the plate centre, i.e. the inlet to wall distance varies between 38.5 and 41.5 cm in the Mfl runs. The comments below on Mfl are solely based upon the four simulation runs. According to the materials documentation, the Mfl model assumes constant heat conductivity, constant specific heat and the existence of a no-flow temperature. The no-flow temperatures deviate a lot from the reported melting point $T_M = 131^\circ\text{C}$ for Lupolen (MatWeb, www.matweb.com) and from the glass transition temperature $T_G = 148^\circ\text{C}$ for Makrolon (Bayer product information, www.makrolon.com/eigenschaften), which is confusing – also see comment on **Fig. 4.1** below. No specific modelling of the latent heat of crystallization seems to exist. All convective heat transfer in the z -direction is ignored ([Kennedy], p.71). The shear rate is approximated as $\dot{\gamma} \approx |\partial v_r / \partial z|$ ([ibid.], p.70). The density variations are described by a thermodynamic PVT model – cf. [ibid.], p.28-29, or considered as incompressible ([ibid.], p.60). The underlying data points for pressure, specific volume and temperature, as well as the model coefficients, are documented in the Mfl data base. However, as can be seen from **Figure 4.1** – which we have constructed from the 13 given calibration points of Lupolen and which shows the two phase-specific Mfl sub-models – the modelling routine seems imperfect: as we understand Mfl data, the sub-model for the liquid phase does not fit the calibration points (and the Mfl no-flow value 120°C is lower than can be estimated from **Fig. 4.1**). In order to imitate the Mfl model, we have to use almost the same density in both phases – and therefore the contraction effect of solidification becomes (unrealistically) small. (According to the Mfl data base, the generic densities $\rho = 1/V$ of the solid and liquid phases are 0.952 and 0.809, respectively; the latter value fits the data points in **Fig. 4.1** but is contradictory to the sub-model for the liquid phase.) As to viscosity, the user may choose between a 1st and a 2nd order model – cf. [Kennedy], p.11. According to the 2nd order model, $\ln \eta$ is a 2nd order polynomial of T and $\ln \dot{\gamma}$, and no theoretical, asymptotic results are used – cf. **Sec. 2.2.3**. Such modelling is a risky business, especially if the calibration points are few and close – see **Figure 4.2**, where the 6-parameter 2nd order Moldflow model and the 6 underlying data points of Makrolon are shown. There are two kinds of questionable behaviour: an increase by $\ln \dot{\gamma}$ for fixed T at low $\ln \dot{\gamma}$ -values, and an

increase by T for fixed $\ln \dot{\gamma}$, shown by curves crossing at high $\ln \dot{\gamma}$ -values. The latter model weakness is merely theoretical – the shear rate is below 10^4 s^{-1} here – but the former is non-negligible: in our normal processing run for Makrolon, run **PC-warm**, 21% of the time-node registrations fall within the first questionable region. Therefore the 2nd order viscosity model has not been chosen here. The 1st order model is a power-law model with multiplicative temperature dependence, of type $\exp(-cT)$, making the deviations from an Arrhenius-type model relatively small. For Makrolon the Mfl viscosity shows a 20-fold decrease from $T_{no-flow}$ to T_f – a support for our non-isothermal model.

The materials data of the basic simulation runs are found in **Table 4.1**, where our fitted values to the Mfl density and viscosity models are marked by asterisks. Data seem somewhat uncertain, since e.g. Makrolon heat capacity $1170 \text{ J/kg}^\circ\text{C}$ and thermal conductivity $0.2 \text{ W/m}^\circ\text{C}$ are found in the online materials database MatWeb.

In the Mfl runs, the metal mould is modelled by [Valtonen] as a square block with sides 100 cm and height 50 cm. Two circular cooling circuits of diameter 30 mm, with c/c distance 10 cm are modelled – cf. **Figure 4.3**. For each circuit the distance between the inlet and outlet channel legs is 40 cm and the cross leg is situated 30 cm from the closest mould side surface. Thus the horizontal distance between the points on the cavity wall surface and the centre of the closest cooling line varies between 0 and 20 cm, with an average of 8.9 cm, and the overall distance to the closest tube wall varies between 3.5 and 19.1 cm, with an average of 9.15 cm – see **Figure 4.4**, where the radial variation is shown (inlet at $r = 0$). Four Mfl nodes, selected for special study, are also marked. Our FD program accepts a constant distance H_w to the closest tube wall or a specified radial distribution, like the one in **Fig. 4.4**. The standard Mfl wall parameters are $\rho_w = 7800 \text{ kg/m}^3$, $\lambda_w = 29 \text{ W/m}^\circ\text{C}$ and $c_{p,w} = 460 \text{ J/kg}^\circ\text{C}$.

Figure 4.1 Mfl calibration points and phase-specific PVT submodels, Lupolen 5031L. Curves for constant pressure



4.2 Materials data

Figure 4.2 MFI calibration points and 2nd order viscosity model, Makrolon 2205. Curves for constant temperature

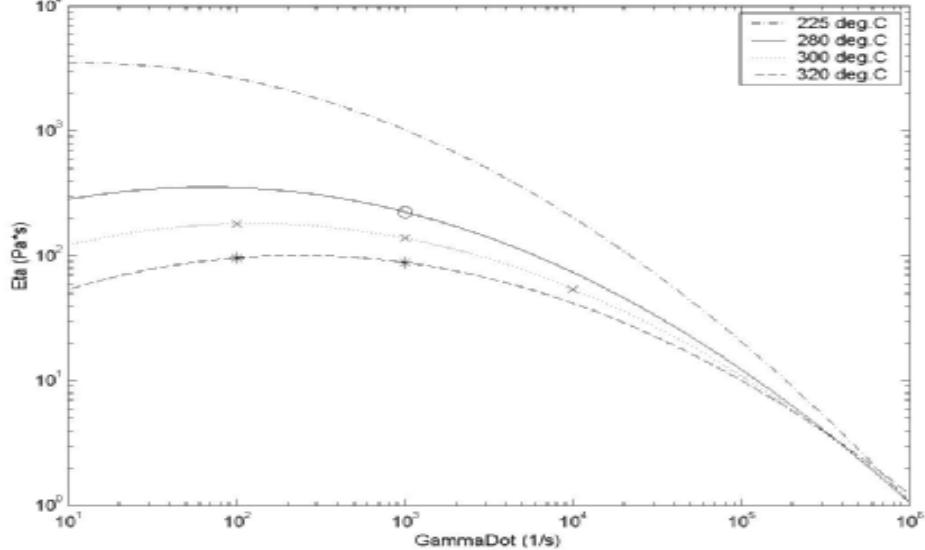
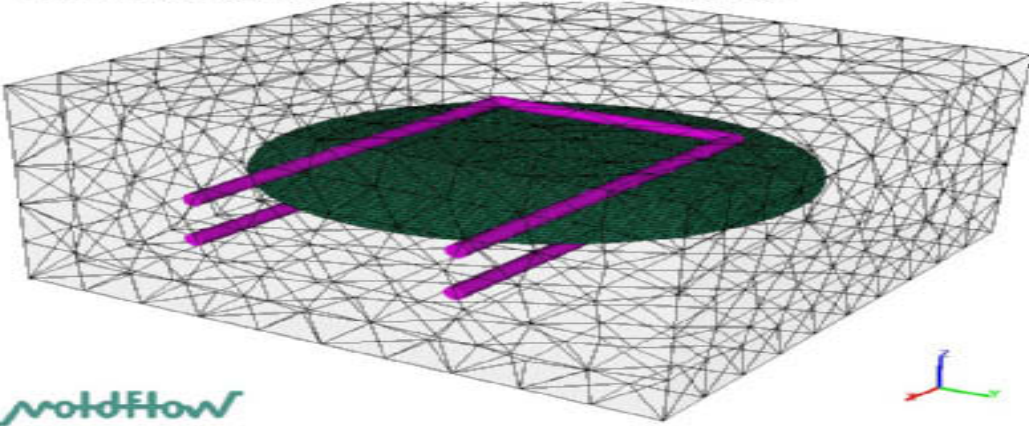
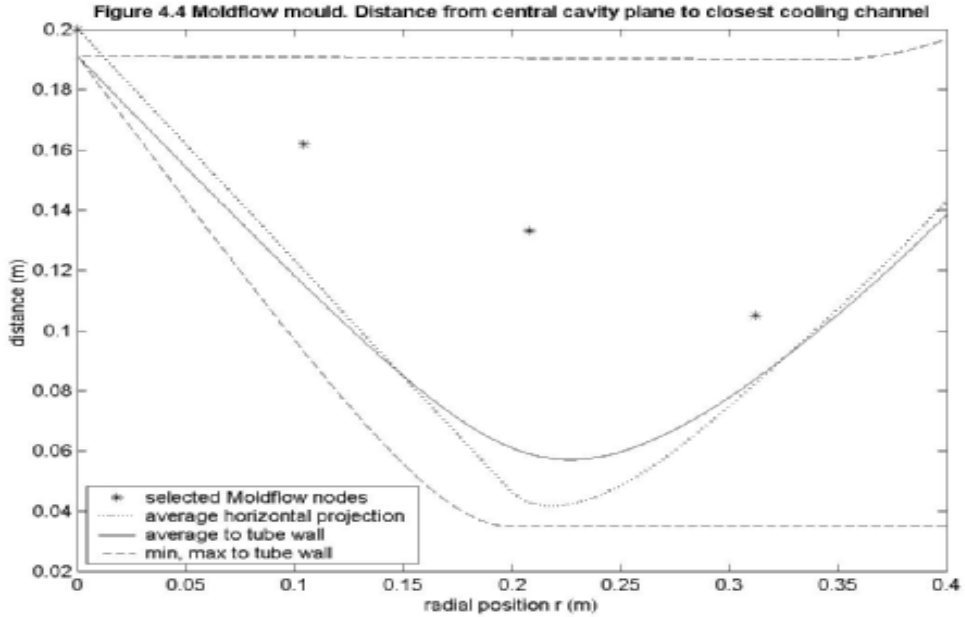


Table 4.1 Materials data used in basic FD runs

	Lupolen 5031 L	Makrolon 2205	
ρ_ℓ	900*	1120*	kg/m ³
ρ_s	925*	1180*	kg/m ³
$\lambda_\ell = \lambda_s$	0.175	0.173	W/m °C
$c_{p,\ell} = c_{p,s}$	3643	1700	J/kg °C
$\eta = K_0 \cdot e^{B/(T-T_B)} \cdot \dot{\gamma}^{n-1}$	K_0 802.2*	0.06195*	Pa · s ⁿ
	B 1139.0*	5552.0*	°C
	T_B -273.2	-273.2	°C
	n 0.4403	0.7351	
H_L	0	---	J/kg
$T_{no-flow}$	120	170	°C

Figure 4.3 Moldflow mesh. Mould, cavity and cooling circuits



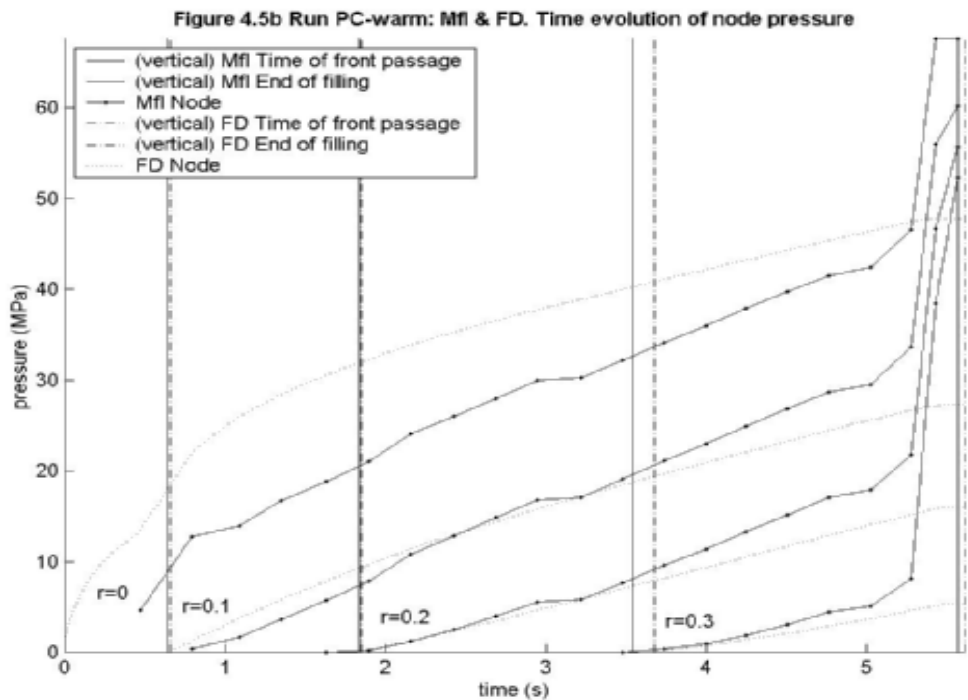
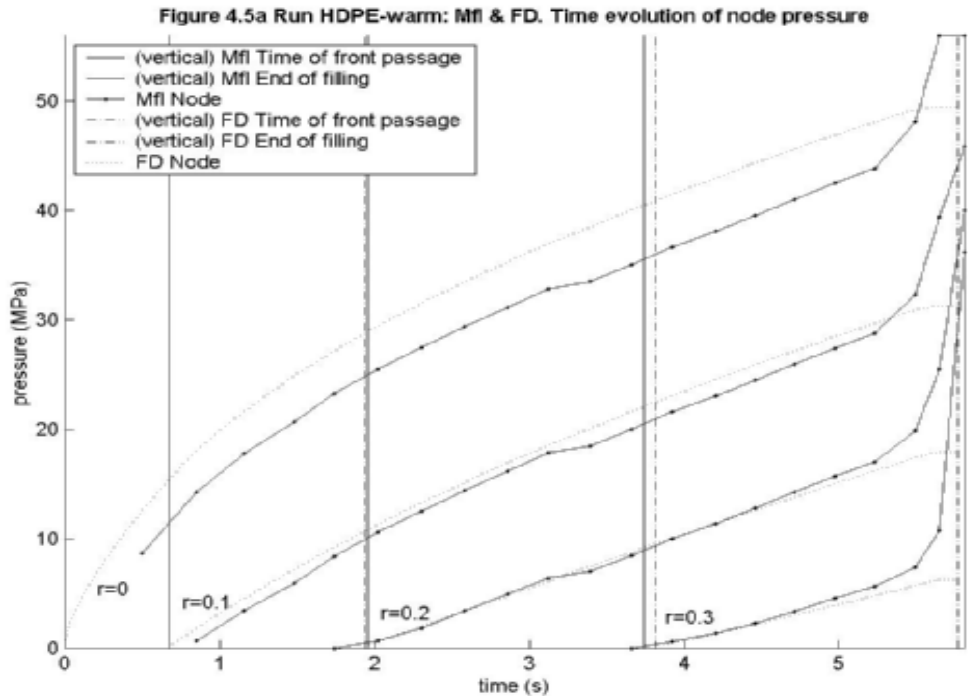


4.3 Comparison runs

4.3.1 Pressure distribution

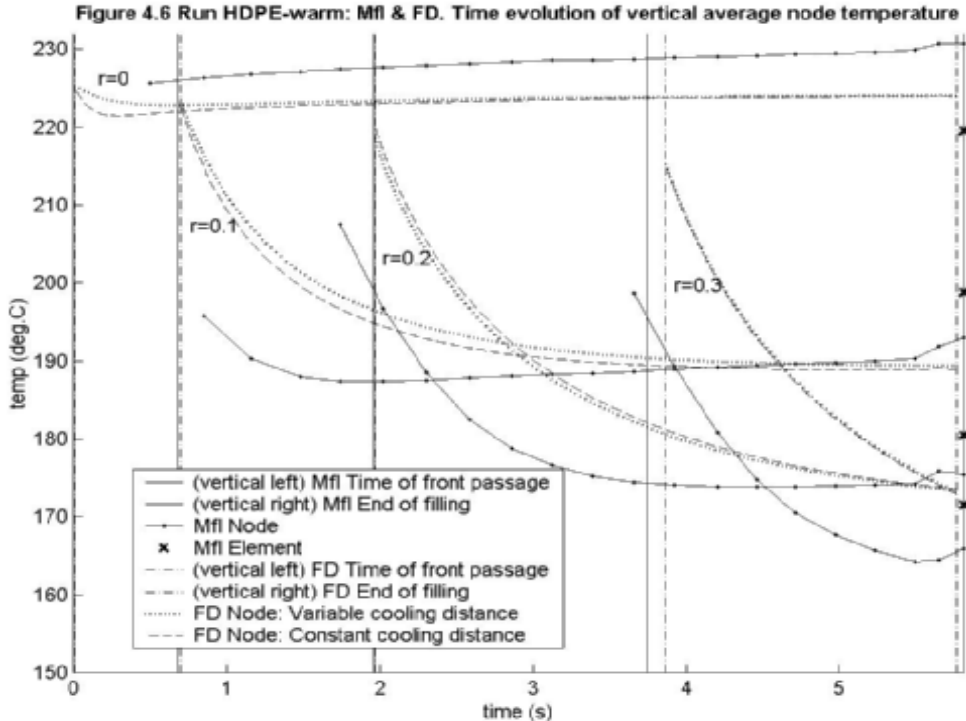
In the Moldflow (Mfl) runs, transfer to pressure controlled filling takes place when 98% of the mould cavity is filled. Before that, filling is controlled by the inflow rate. In our FD program this is implemented as a transfer to constant pressure at the inlet, as it (the pressure) is computed when 98% of the volume is filled, and kept for the rest of the filling. The time evolution of pressure, at four selected nodes, is shown in **Figure 4.5**. The vertical lines show the nodal front passages and the end of filling. Notice that the Mfl pressure registrations occur a little before the (in another data file) registered times of front passage. The steep increase of the Mfl pressure values immediately before the pressure-controlled filling (the horizontal pressure lines in **Fig. 4.5**) is probably due to the asymmetric placement of the inlet. The FD runs presume symmetry. Up to the end of filling the pressure deviations between FD and Mfl are relatively small for HDPE (in both runs). We have also tried isothermal pressure values (not shown) and as expected – cf., e.g., [Agassant et al.], pp.141,146 – these are much lower, even if based upon the average viscosity, and this simplifying model is therefore definitely rejected here. For PC the Mfl and FD pressure evolutions follow different increase rates (in both runs). **Figure 4.7** below shows that the inflow rates are of the same magnitude in all runs. The Mfl pressure evolutions in **Fig. 4.5** are almost identical for both materials, while in the FD runs the clear difference between the power law index n values – see **Tab. 4.1** – has an impact upon pressure propagation, according to (3.6). But shear thinning is of course also temperature-dependent – see **Fig. 4.7** for process temperatures T_I and T_E . Our logarithmic pressure model is clearly visible for $r = 0$ in **Fig. 4.5b**, and its systematic deviation from the Mfl evolution may indicate a model error. But we are somewhat sceptical to the Mfl results for both runs PC-warm and PC-cold – see **Fig. 4.10** below, where the differences between the top and bottom frozen layers, i.e. the vertical distances $\times - \times$ and $\nabla - \nabla$, are big.

4.3 Comparison runs



4.3.2 Temperature distribution

All four runs show similar patterns of node temperature evolution— see **Figure 4.6** for the vertical average temperatures in run HDPE-warm. For Mfl there are two data files of information – on the selected nodes and on the corresponding finite elements (at the end of filling, only). For most nodes, the final FD temperatures lie between and/or close to these two values. Although there is no severely divergent Mfl-FD pair of evolution curves, the average deviation is more than 5°C for all nodes in all runs. However, the differences at the time of filling between the Mfl node and Mfl element data are even bigger. This probably means that if both these Mfl sources of information were available during the whole filling phase the FD-curves in most cases would lie in between. For Mfl also notice the continuous temperature rise at the inlet node ($r = 0$) and the sharp initial fall at all the other nodes. The former might come from an implicit model for the inlet channels (runners), locally heating the metal mould but unknown to us, and the latter from a cooler front than we get (even before the front passage, as registered in another Mfl data file; which indicates an imprecise Mfl-time). The big differences for $r > 0$ at the very front passage and thereafter have a simple explanation, as we view it: Mfl ignores all heat transfer by vertical convection, here fountain flow. The general temperature fall by time in both Mfl and FD comes from the dynamic expansion of the frozen layer. The FD runs are shown with constant and with variable distance to the cooling lines. The differences between them are small. The variable distance model is expected to be the more realistic one close to the inlet – cf. **Fig. 4.4** – and for the other nodes, because of their position, both our models will probably accomplish slightly more cooling than Mfl, but neither the Mfl node nor element temperatures seem to deviate systematically from ours at the time of filling.



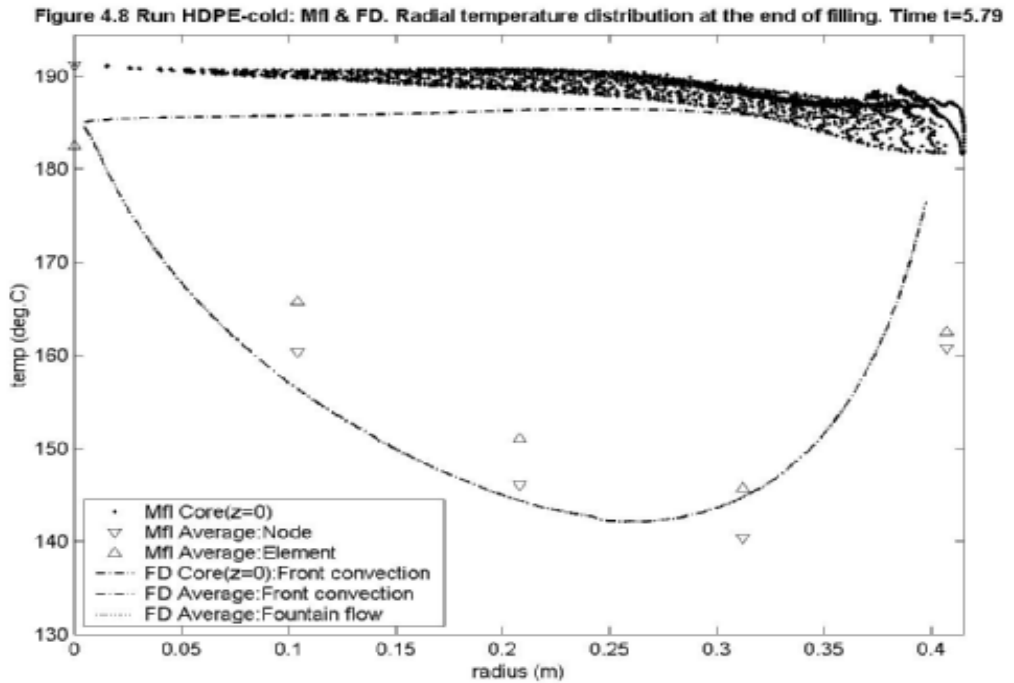
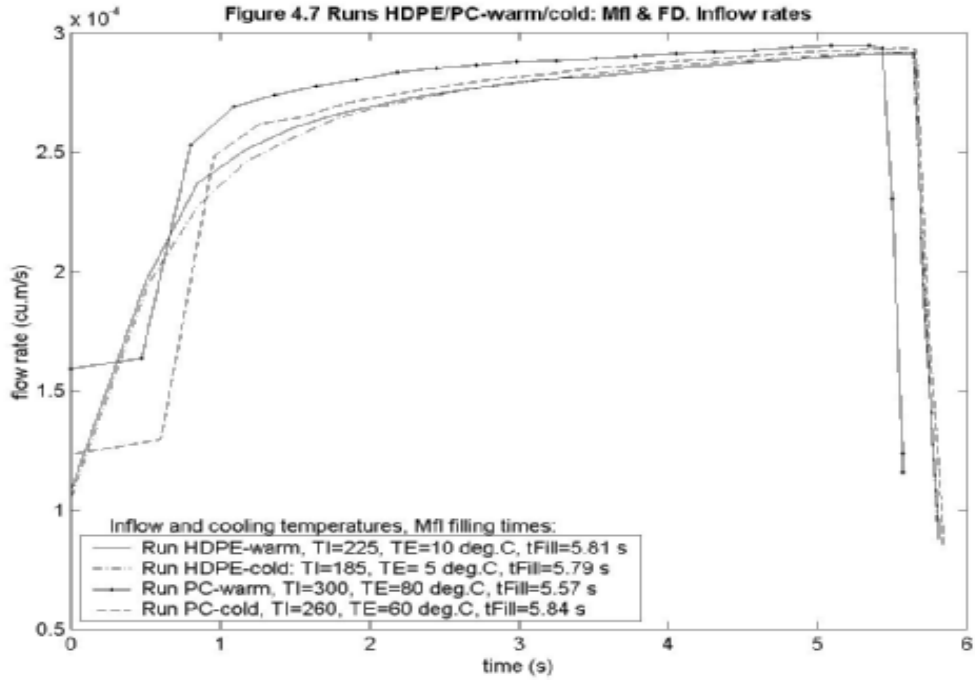
4.3 Comparison runs

The radial temperature distribution at the end of filling is illustrated for run HDPE-cold in **Figure 4.8**, letting the Mfl inlet, as well, correspond to $r = 0$. The picture is similar for all the other simulation runs. For Mfl the two sources of vertical averages, for the selected nodes and for the corresponding finite elements, are marked. Here a fifth Mfl node is included, at radial position $r = 40.74$ cm relative to the inlet. Since the Mfl end of filling corresponds to $r = 41.5$ cm (while FD assumes 40 cm), the Mfl nodes are on a different time scale. The first time registration at the fifth Mfl node, e.g., occurs simultaneously to the transfer to pressure controlled filling, at $t = 5.64$ s, which in the FD run corresponds to radial position $r = 39.5$ cm. Therefore the temperature differences in **Fig. 4.8** are partly exaggerated. The remaining deviations are probably due to our simplified front models. But to ignore completely vertical heat transfer by convection, as Moldflow does, may be an oversimplification. The difference between the two FD front models (see **Sec. 3.1.4**), fountain effect (dotted curve) and front convection (dashdot curve), is not visible. The FD and Mfl temperature profiles have similar shapes, with minimum at $r \approx 0.25 - 0.3$ m, but the Mfl profile is somewhat flatter. The temperatures at the symmetry plane $z = 0$ (core) for all FD and Mfl nodes are also plotted. The immediate rise from the inlet temperature for the Mfl core values – and “Mfl Average: Node” – at $r = 0$ is not fully understood (if not an effect of the unknown runner system), while the slight increase during the final filling comes from the asymmetric Mfl gate position. Moreover, we consider more shear rate terms in (2.7) than Mfl does, which ought to increase the FD values at the inlet. This is what the “Mfl Average: Element” indicates at $r = 0$.

The resulting vertical temperature profiles for the studied amorphous polymer are shown for the selected Mfl finite elements (including the fifth – ‘front’ – element situated near the cavity radius) in **Figure 4.9a-e**. (The semi-crystalline thermoplastic is considered in **Sec. 4.4**.) For Mfl the profile is subdivided into the positive and negative vertical positions (dashed and solid curves, respectively, because of systematic deviations). The Mfl cooling system and the flow direction of the coolant are symmetrically modelled (cf. **Fig. 4.3**), and the runner system is not explicitly (asymmetrically) modelled. Despite this symmetry, the Mfl temperatures in **Fig 4.9** differ between the upper and lower halves. If the runner system were implicitly modelled in Mfl, we would expect the temperature differences to be greatest near the inlet, but this is not the case. As for the FD and Mfl comparisons, the profiles are similar and there are clear deviations only at the inlet and at the front (cf. comments on **Fig. 4.8** above) – shown by the two plotted Mfl-averages ‘Mfl Element Vertical average’ and ‘Mfl Node’, that otherwise (nearly) surround the FD-average ‘FD Node Vertical average’ (dotted). However, the average absolute deviations FD-Mfl for the 21 individual vertical levels registered by Mfl are above 10 °C for all five nodes. The position of the frozen layer (i.e. the no-flow temperature) is marked. Again the clear deviations are at the inlet and at the front element; otherwise the FD layer position is between the upper and lower Mfl values. Notice the temperature levelling near the front, by comparing **Fig. 4.9e** and **Fig. 4.9d**. As expected, this effect is strongest for FD (with a special front model) but it is visible also for Mfl – unclear how. The success of the two FD sub-models of variable (shown here) and constant height to the cooling lines is similar.

The final frozen layer positions in all runs are shown in **Figure 4.10**. As for time-scale differences Mfl-FD – see comments on **Fig. 4.8**. The Mfl values for $Z < 0$ and $Z > 0$ differ a lot for the amorphous PC, but not as much for the semi-crystalline HDPE. Why? The maximum layer thickness for HDPE is obtained at a smaller radius than for PC according to FD, but rather the opposite according to Mfl. All Mfl and FD maxima occur at approximately 2/3-3/4 of the plate radius, differing from some earlier results for disk-shaped cavities, e.g. [Tadmor

& Gogos], p.600, where the relative radial position is below 40%. The absence of front convection places the Mfl maximum closer to the disk radius.



4.3 Comparison runs

Figure 4.9a Run PC-cold: Mfl & FD. Vertical temp.profile & frozen layer at the end of filling. Mfl $r=0.0000$, FD $r=0.0047(\text{m})$

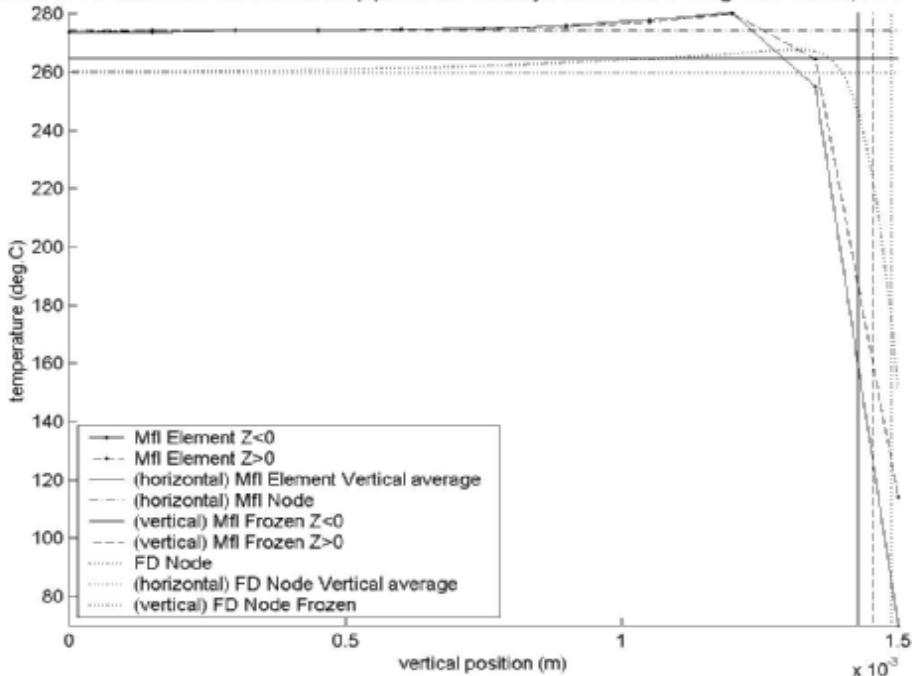


Figure 4.9b Run PC-cold: Mfl & FD. Vertical temp.profile & frozen layer at the end of filling. Mfl $r=0.1042$, FD $r=0.1089(\text{m})$

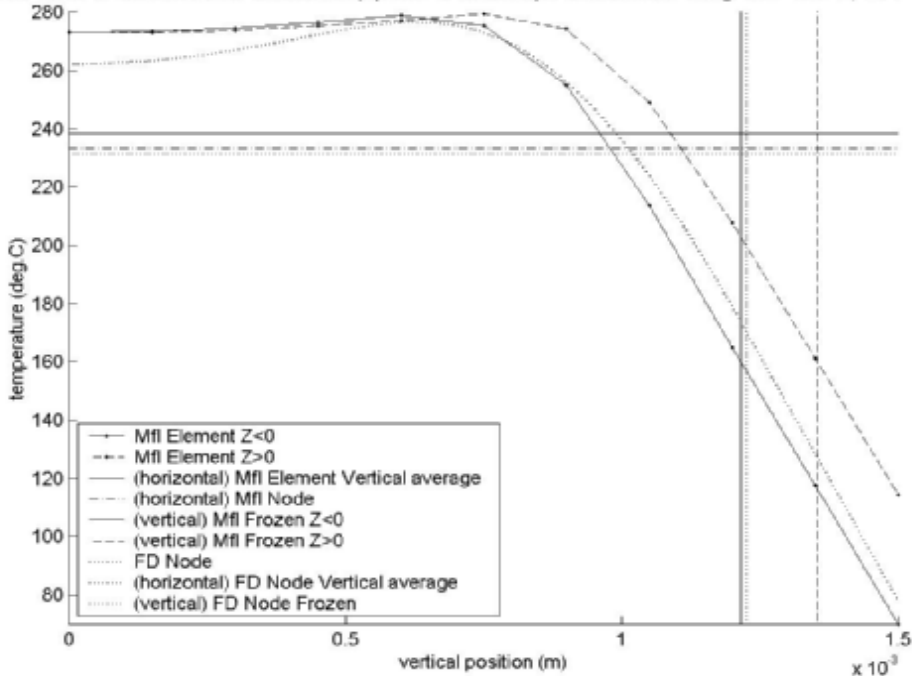
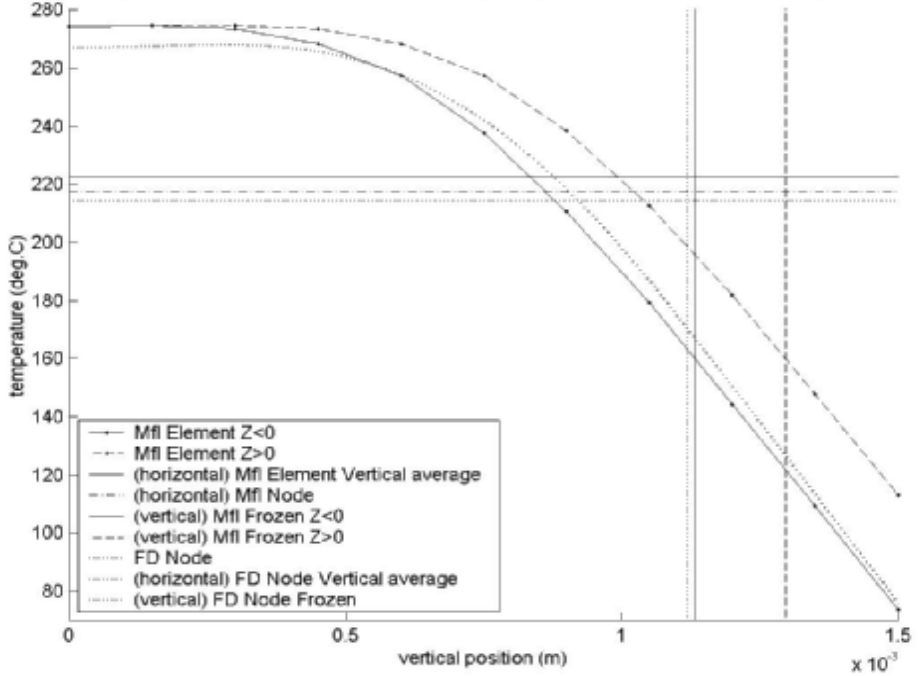
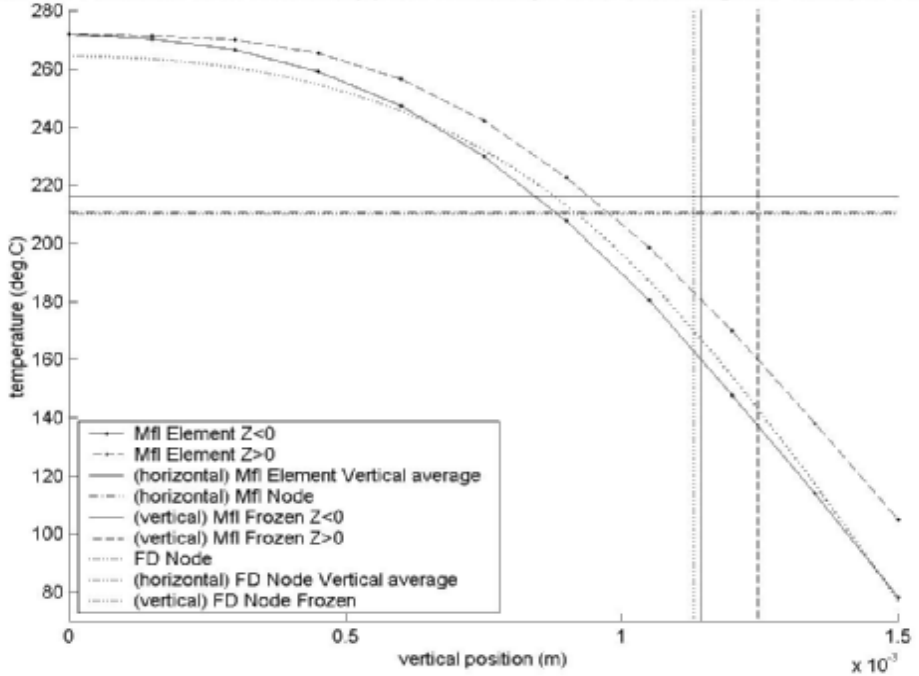


Figure 4.9c Run PC-cold: Mfi & FD. Vertical temp.profile & frozen layer at the end of filling. Mfi $r=0.2080$, FD $r=0.2130$ (m)Figure 4.9d Run PC-cold: Mfi & FD. Vertical temp.profile & frozen layer at the end of filling. Mfi $r=0.3121$, FD $r=0.3172$ (m)

4.3 Comparison runs

Figure 4.9e Run PC-cold: Mfl & FD. Vertical temp. profile & frozen layer at the end of filling. Mfl $r=0.4074$, FD $r=0.3976$ (m)

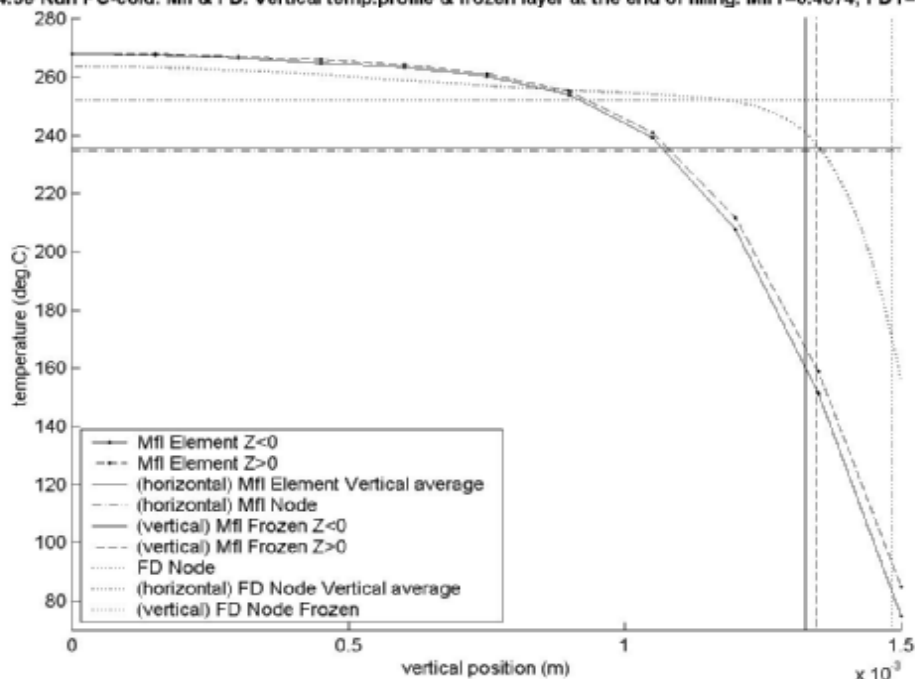
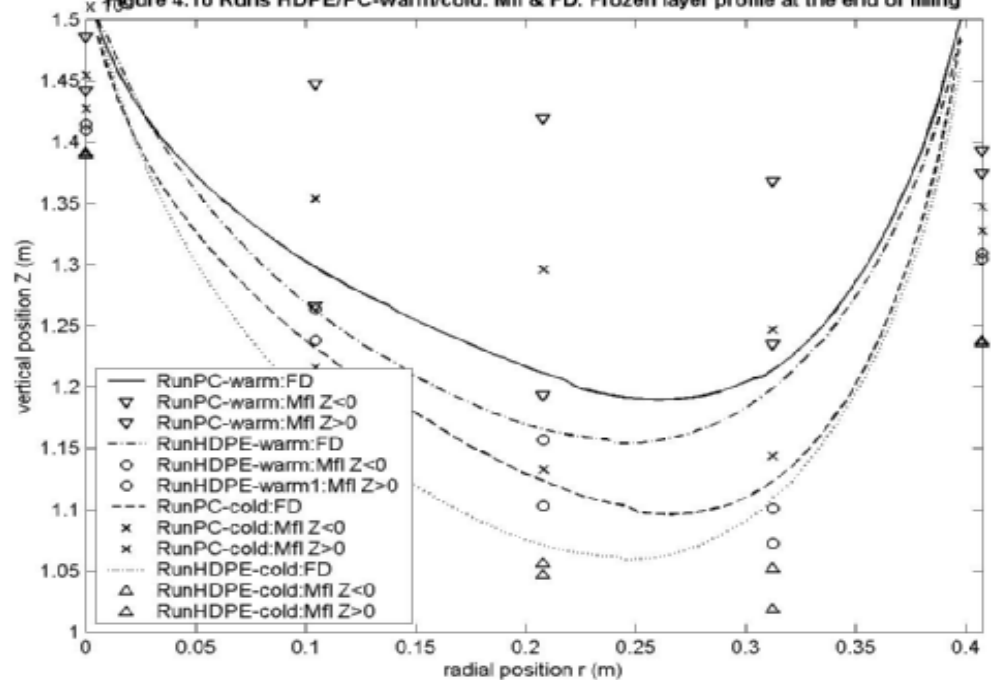


Figure 4.10 Runs HDPE/PC-warm/cold: Mfl & FD. Frozen layer profile at the end of filling



4.4 Variation of physical model

4.4.1 Latent heat of crystallization

The constant value $c_p = 3643 \text{ J/kg}^\circ\text{C}$, found for the semi-crystalline polymer Lupolen 5031 L in the Moldflow database, presumably reflects the overall enthalpy drop from recommended inflow temperature to cooling temperature, including the latent heat of crystallization L_M at T_M . Now we model L_M explicitly, and for a comparison with the basic runs above we adjust the molar weight ($= 0.0298 \text{ kg/mol}$) to get the same overall enthalpy drop. Our applied model – cf. (2.1), (2.2) – with T in $^\circ\text{C}$ is

$$c_{p,s}(T) = 1680 + 4.3 \cdot (T - 25), \quad c_{p,\ell}(T) = 2080 + 2.6 \cdot (T - 25) \text{ J/kg}^\circ\text{C}, \quad L_M = 270000 \text{ J/kg}.$$

According to **Figure 4.11** and **Figure 4.12** below (where the boldfaced curves refer to the **basic model**, i.e. the one with constant c_p , λ and pressure-coefficient $\beta = 0$), the temperatures are significantly affected by the $L_M \neq 0$, **linear c_p -model** (dashed curves) near the front, where the small $c_{p,\ell}$ -value offers little initial resistance to decreasing temperatures.

(For general comments upon the basic model, cf. **Fig. 4.8** for run HDPE-cold and **Fig. 4.9b,e** for PC-cold.)

4.4.2 Heat conductivity

The constant value $\lambda = 0.175 \text{ J/m}^\circ\text{C}$, found for Lupolen 5031L in the Moldflow database, is used in the basic runs above. To get a comparable overall heat conductivity of a general HDPE material according to [Van Krevelen], we have to assume the crystallinity less than 23% (!), letting

$$\lambda_s(T) = 0.235 - 0.000431 \cdot (T - 25), \quad \lambda_\ell(T) = 0.126 - 0.000137 \cdot (T - 25) \text{ J/m}^\circ\text{C}.$$

Despite the (unrealistically) small conductivity below T_M the resulting deviations – see the **linear λ -model** in **Fig. 4.11** and **Fig. 4.12** below (dashdot curves) – from the basic runs are evident, especially behind the front – λ_s increasing the heat flow through the frozen layer and hence decreasing the temperature. The opposite occurs at the front – where the conductivity is dominated by λ_ℓ , less than the overall average λ . The discontinuity of the temperature derivative at the frozen layer in **Fig. 4.12** is expected.

4.4.3 Viscosity dependence of pressure

In the Mfl comparison runs above the pressure coefficient of viscosity is put to zero. The reported pressure coefficient for HDPE, cf. [Van Krevelen], is $\beta = 0.68 \cdot 10^{-8} \text{ m}^2/\text{N}$. For Lupolen the effect is noticeable behind the front – see the **pressure coefficient $\beta \neq 0$ model** in **Fig. 4.11** and **Fig. 4.12** (dotted curves) – β slightly increasing the viscosity and thus the viscous heat and the temperature. (The exponential coefficient is four times as big for PC polymers, like Makrolon, but we limit our comparisons to the HDPE runs.) The pressure profile is also markedly affected, increasing the pressure levels in the HDPE runs by 20 - 25 %.

4.4 Variation of physical model

Figure 4.11 Run HDPE-warm-E: Mfi & FD. Radial temperature distribution at the end of filling. Time $t=5.81$

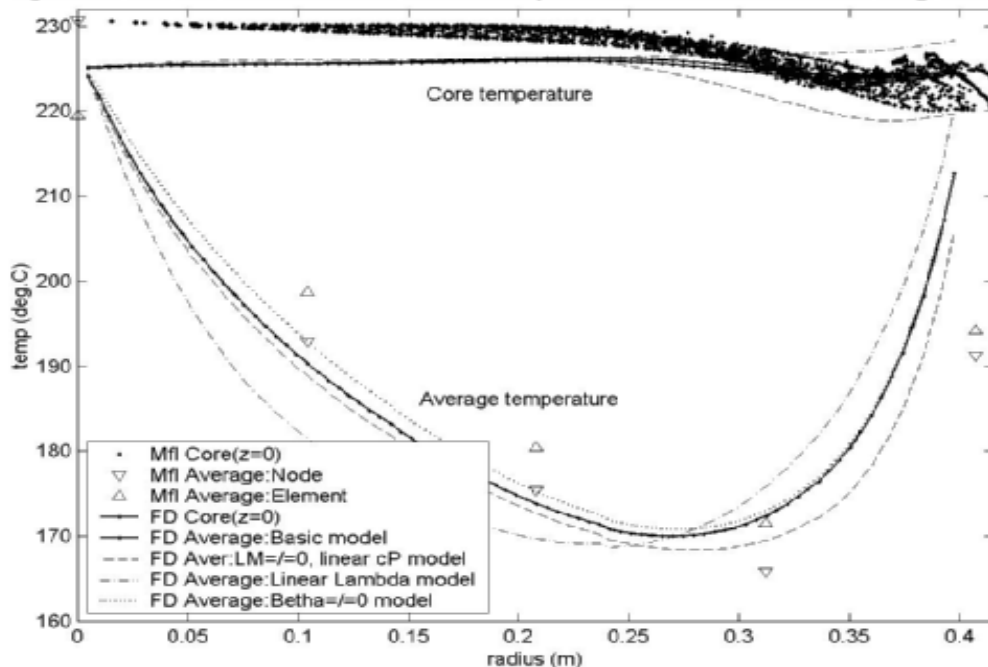


Figure 4.12a Run HDPE-cold-E: Mfi & FD. Vertical temperature profile at the end of filling. Mfi $r=0.1042$, FD $r=0.1089$ (n

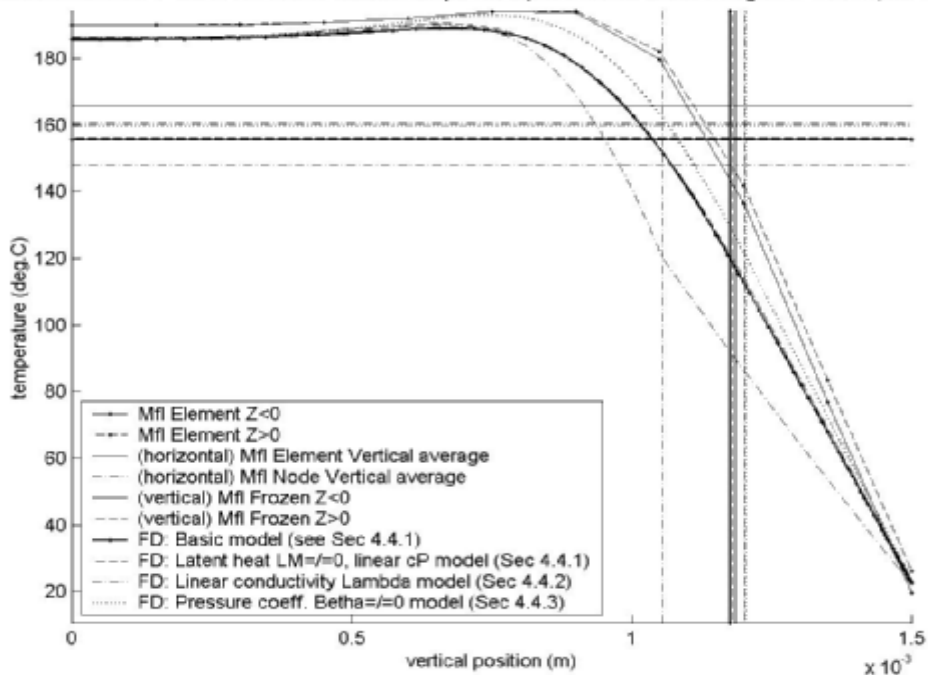
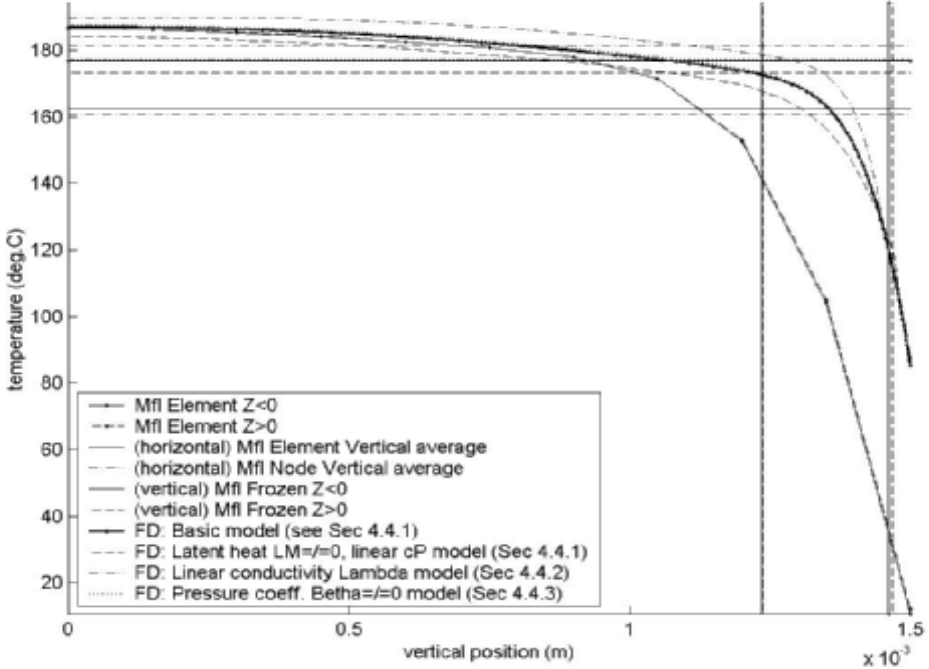


Figure 4.12b Run HDPE-cold-E: Mfl & FD. Vertical temperature profile at the end of filling. Mfl $r=0.4074$, FD $r=0.3976$ (n

4.5 Method performance

4.5.1 Relations to the number of vertical levels (control volumes)

With time step k and radial step i fixed, the number of control volumes $J+1$ is also the total number of equations in two systems, to solve for T_s and T_ℓ respectively. As J is varied, for compatibility the acceptance limits for a T -solution (with the non-frozen height h fixed) are taken equal, as measured by residual per equation. These simulation runs, named ‘HDPE-cold-E’, coincide with run HDPE-cold in **Sec. 4.3** but are here supplied with the more sophisticated physical HDPE properties $c_p - L_M, \lambda, \beta$ in **Sec. 4.4** (but remember that λ_s corresponds to a low crystallinity). The managing of these equations is illustrated by the vertical temperature profile in **Figure 4.13** for radius $r = 0.1$ m and for different J ’s. The radial profiles of average temperature are found in **Figure 4.14**. In the Mfl runs above, 11 vertical levels were used per half-width $Z \leq 0, Z \geq 0$, i.e. in all 21 levels. In the FD runs this number is rather too small to provide reliable results (cf. **Fig. 4.13**, **Fig. 4.14**), and $J = 40$ is recommended for this application. However, to be on the safe side we used $J = 80$ in the comparison runs above.

The h -equation, i.e. the determination of the frozen layer surface, is solved once per (k, i) -combination and the systems of T -equations are solved once per h -iteration. The average number of iterations per program call for a solution varies slightly, for the h -equation from 8.26 ($J = 10$) to 6.58 ($J = 600$) and for the T -equations from 3.73 ($J = 10$) to 3.36

4.5 Method performance

($J = 600$). For each T -iteration an iterative T -step routine is called. However, the standard Newton step length 1.0 is directly accepted in most cases – for $J = 10$ the T -step routine is called 8 times (out of 115 403 T -iterations overall), for $J = 20$ 2 times (out of 108 496) and for $J = 40$ 1 time (out of 95 758), and otherwise not at all. In all these exceptional cases the remaining residual sum, squared, is close to the acceptance limit of a solution, and neither a step length reduction nor (with one exception) the backup routine steepest descent provides improvements. All these difficulties occur at the inlet ($i = 1$), where the idealized initial/boundary conditions – (IC/BC) T_i constant across the cavity gap, and (IC) T_e constant in the wall – form a challenge. However, the overall method works also in these cases, by reducing the h -step length (closer to the solution of the previous time level $k-1$). The full distributions of iterations are shown in **Figure 4.15**. As for the h -computing, 1 iteration per program call corresponds to $h = H$.

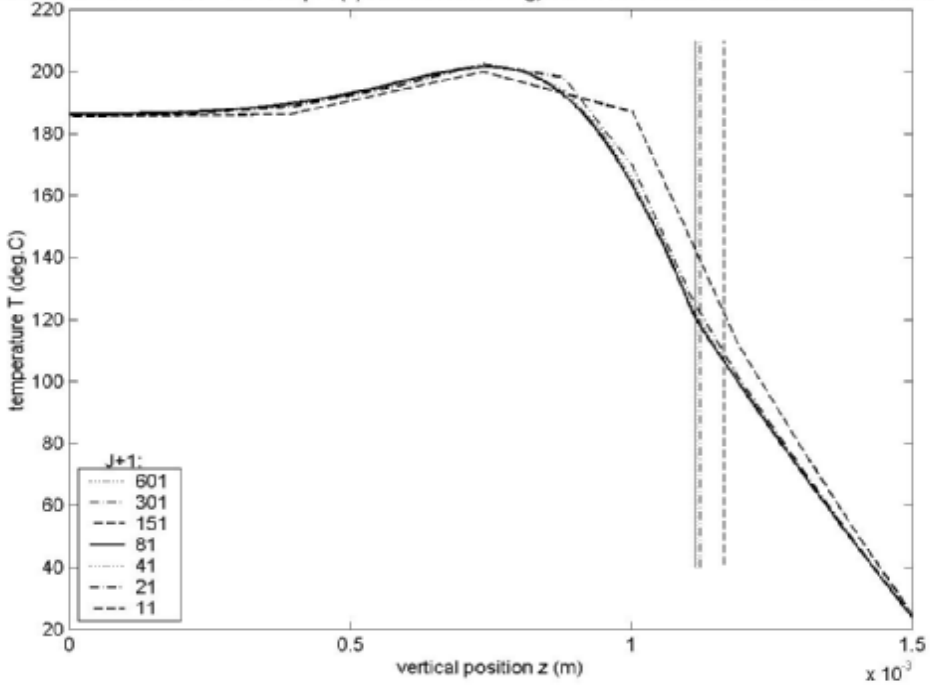
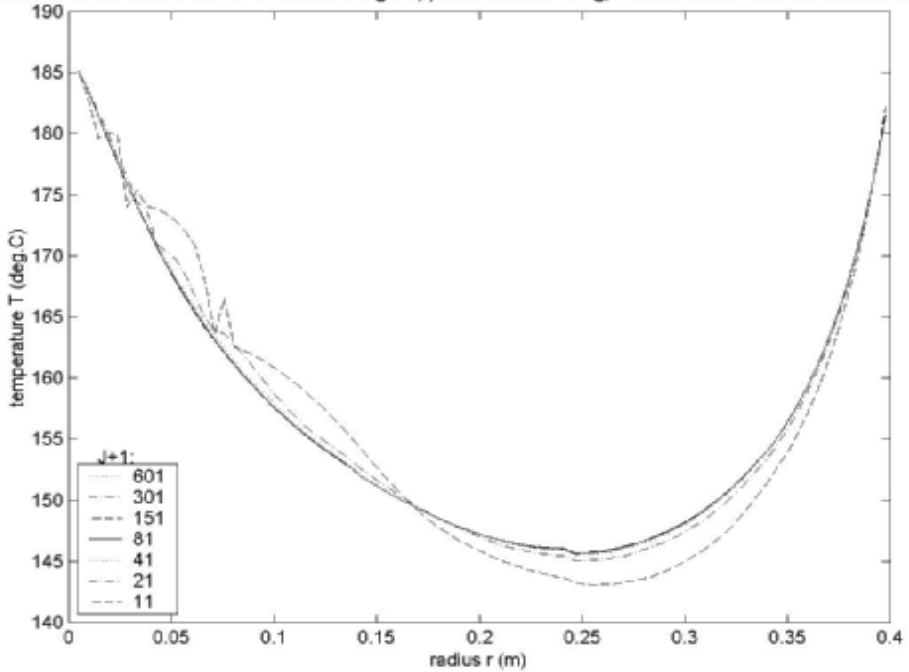
The computing time increases by J from around 11 sec. ($K = 84, J = 10$) via 20 sec. ($K = 84, J = 40$) to 3 min. ($K = 84, J = 600$) on a 32-bit 600 MHz Pentium-3 PC, i.e. slower than proportionally to J .

4.5.2 Wall series solution

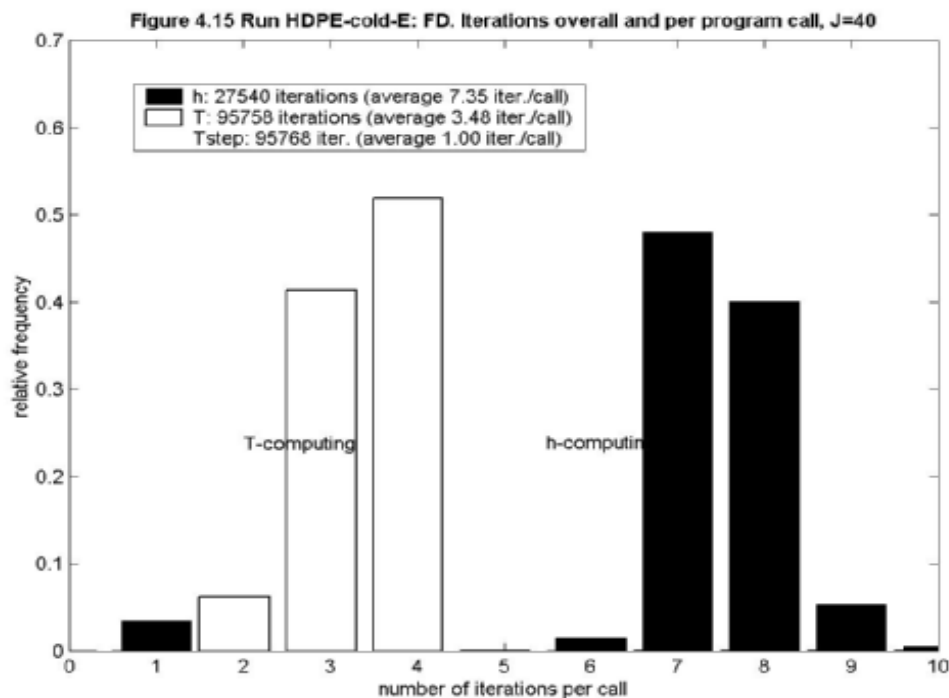
We have varied the number N of wall series terms as well. In run HDPE-warm $N = 20$ is enough to describe the temperature and frozen layer profiles for the inner cavity half ($r \leq 0.2$ m), while at least $N = 40$ is needed further out ($r \geq 0.2$ m). This is due to the worsened convergence properties at the front – cf. **Sec. 3.2.5**. Another possibility is to decrease the time step at the very front: we have used $pTCrit = 0.9$ (cf. **Flowchart 3.1**), i.e. a reduction by at most 10% per time step of the temperature difference solid melt – wall.

4.5.3 Control volume at the frozen layer

Let j_h denote the axial index value of the last liquid node, locally. Our original idea was to surround a movable node at the frozen layer position $z = h$ by a control volume of vertical extension $z \in [\frac{1}{2}(z_{j_h} + h), \frac{1}{2}(h + z_{j_h+1})]$, i.e. of fixed length as long as j_h is fixed, and to exclude that volume from the system of temperature equations (since the temperature is prescribed at h as T_M). However, each time h changes j_h -value the total weight of the frozen layer equations changes discontinuously, which might imply that the computed residual of the h -equation (3.13), discretized, becomes discontinuous as well. In fact, in one of the runs, HDPE-cold, 1722 h -iterations out of 9766 had one non-decreasing LHS-term in the h -equation as a function of h , and the number of h -iterations were almost twice that of our final choice; where we simply exclude the volume surrounding h , letting the neighbour volumes, which surround z_{j_h}, z_{j_h+1} , have one boundary at $z = h$. For this choice only 14 out of 42040 h -iterations in all four comparison runs had one of the three LHS-terms of the h -equation non-decreasing, and in none of them this unexpected behaviour (cf. Sec 3.2.3) meant a non-decreasing LHS.

Figure 4.13 Run HDPE-cold-E: FD. Temp. $T(z)$ at the end of filling, as the number of vertical levels $J+1$ varies, $r=0.108$ Figure 4.14 Run HDPE-cold-E: FD. Vertical average $T(r)$ at the end of filling, as the number of vertical levels $J+1$ varies

4.5 Method performance



5 Application: Triangular plate

This **Chapter** documents the second application type, polygonal star shaped cavities (relative to the inlet), of constant gap width. For the radial flow assumed, the distance along a stream ray to the cavity wall is crucial for the time when the streaming phase ends and the stagnant phase begins, for the ray in question. The geometry needs to be taken into account for the determination of each time step, based upon the active flow angle, the additional filled area and the gap width. This is done in **Sec. 5.1**. In **Sec. 5.2** we describe the data and model-ing of a concrete application, a uniform triangular plate. Materials data for one amorphous thermoplastic, a polystyrene (PS), and one semi-crystalline material, a polyoxymethylene (POM), come from the data base of Cadmould, a FEM-program of Simcon. We have made a somewhat critical comment about the Cadmould viscosity and enthalpy models. As a simplifying option in Cadmould, the metal mould has not been explicitly modelled (by [Nilsson]). To match this we assume a constant depth of the cooling lines from the cavity wall surface. In **Sec. 5.3** the comparison runs, two of each material, are analysed. The Cadmould runs are performed by [Nilsson]. We have to report fatal problems in the FD runs of POM, and limit the discussion to the PS runs. To compensate for our (perhaps too) strict subdivision into rays of full stream intensity and rays of complete stagnation we mention the possibility to use effective instead of nominal flow angles. The symmetry of the uniform triangle defines, e.g. three equivalent corner rays and three equivalent mid-side rays. This and the expected symmetry between the upper and lower halves of the cavity gap are used in plots of the vertical temperature profile vs. radius and vs. angular deviation from the nearest corner ray. The radial profile of the frozen layer surface (of no-flow temperature) is also evaluated. **Sec. 5.4** includes a few com-ments about the method performance. Apart from the iteration statistics we are also evaluating the square-root increase by time of the frozen layer. Furthermore, our velocity model has been applied to plot the time of injection for different material points at the end of filling.

5.1 Special modelling: Geometry

The mould cavity is here assumed to be star shaped relative to the inlet – positioned at $r = 0$ of a polar (r, φ, z) coordinate system – and the vertical cavity width is constant $2H$, with symmetry plane $z = 0$. By the principle of the distance model and the corresponding energy principle all node points of equal flow history are equivalent as to velocities and temperatures. This means that all node positions (r, φ) of a common radius r (equal activation time t_{act}) are equivalent during the streaming phase, but equivalence during the succeeding stagnant phase also requires a common distance to the mould wall along the radial flow directions (equal stagnation time t_{stag} and thus equal residence time of the fluid). As input the vertical boundary planes of the cavity are specified by the consecutive (x, y) - corner positions. For a computation of t_{stag} , as well as active flow angle φ_{act} and the filled volume, the geometry needs to be taken into account.

Since the mould cavity has constant gap width, the fluid expansion is viewed as an essentially 2D-space process in a flat, polygonal domain X . Consider a boundary line of X . Its intersection L with X is specified by the two corner points a, b – endpoints of the line segment L – and given by $(r_a, \varphi_a), (r_b, \varphi_b)$ where $\varphi_b > \varphi_a$ is assumed. In the star shaped domain, L occupies a positive sector angle $\varphi_b - \varphi_a$ as viewed from the injection point at the origin. The region

5.1 Special modelling: Geometry

enclosed by L and its two endpoint radii is a triangle T , and X is a union of such triangles.

Consider for a moment a basic boundary line, written in parameter form

$$\begin{cases} x(t) = x_a + t \cdot \Delta x, & \Delta x := x_b - x_a \\ y(t) = y_a + t \cdot \Delta y, & \Delta y := y_b - y_a \end{cases}$$

where $(x_a, y_a), (x_b, y_b)$ are the endpoints of the line segment L , which has the length

$$d_{ab} := \sqrt{(\Delta x)^2 + (\Delta y)^2}.$$

The boundary line point $(x(\hat{t}), y(\hat{t}))$ closest to the injection point at the origin is determined by

$$\hat{t} := -\frac{x_a \cdot \Delta x + y_a \cdot \Delta y}{d_{ab}^2}$$

and its distance from the origin is

$$\hat{r} := \left| \frac{x_a \cdot \Delta y - y_a \cdot \Delta x}{d_{ab}} \right|.$$

Denote by r_0 the distance of L from the injection point; whence \hat{r}, \hat{t} determine

$$r_0 := \begin{cases} \hat{r} & \hat{t} \in (0,1) \\ \min[r_a, r_b] & \text{otherwise.} \end{cases}$$

Now let r denote a front circle radius of the expanding fluid. For a mathematical description of the part of T covered by fluid, four cases are distinguished during the filling process.

1. Before the front reaches L , i.e. as $r \leq r_0$, the covered part of T is a circle sector of area

$$\pi r^2 \cdot \frac{\varphi_b - \varphi_a}{2\pi} = r^2 \cdot \frac{\varphi_b - \varphi_a}{2}.$$

2. When the front intersects L at two points $(r, \varphi_1), (r, \varphi_2), \varphi_2 > \varphi_1$, i.e. as the point on L closest to the origin lies between its endpoints and $r_0 < r < \min[r_a, r_b]$, one triangle in the middle plus two surrounding sectors contribute to the area

$$\frac{r^2 \cdot \sin(\varphi_2 - \varphi_1)}{2} + r^2 \cdot \frac{(\varphi_b - \varphi_2) + (\varphi_1 - \varphi_a)}{2}.$$

3. When the front intersects L at one point (r, φ) , i.e. as $\min[r_a, r_b] < r < \max[r_a, r_b]$, fluid covers L from one endpoint up to the point of intersection. The covered part of T is a triangle plus a sector, of area

$$\begin{aligned} & \frac{r \cdot r_a \sin(\varphi - \varphi_a)}{2} + r^2 \cdot \frac{\varphi_b - \varphi}{2} \quad \text{in case } r_a > r_b, \\ & \frac{r \cdot r_b \sin(\varphi_b - \varphi)}{2} + r^2 \cdot \frac{\varphi - \varphi_a}{2} \quad \text{in case } r_a < r_b. \end{aligned}$$

4. When the fluid covers L completely, i.e. as $r \geq \max[r_a, r_b]$, all of the triangle T is filled area

$$\frac{r_a r_b \cdot \sin(\varphi_b - \varphi_a)}{2}.$$

In these cases only the circle sector parts contribute to the active front at r . Their angular sum is the overall active flow angle $\varphi_{act}(r)$.

For a point $(x, y) \in T$, at a distance $r(>0)$ from the injection point at the origin, the stagnation time $t_{stag}(x, y)$ is when the flow radius through (x, y) reaches L :

$$r_{stag} = \beta \cdot r, \quad \beta := \frac{y_a \cdot \Delta x - x_a \cdot \Delta y}{y \cdot \Delta x - x \cdot \Delta y} (\geq 1).$$

During time step No. k , when the radius of the front circle expands another Δr , the additional covered polygonal area ΔA_k is obtained by summing up T -areas, and – in consideration of the efficient local gap width h – the time step Δt_k etc. can be determined as in **Sec. 4.1.1**.

5.2 Materials data

Simulation runs for comparison have been performed by [Nilsson], using the commercial software **Cadmould** of Simcon, Fill version 1.110. In the concrete application, X in **Sec. 5.1** was chosen as an equilateral triangle, with the inlet almost in the middle (4 mm from the centroid). From the Cadmould (“**Cmd**” below) data base of standard materials, one amorphous thermoplastic – the polystyrene Polystyrol 158 K of Basf AG (“**PS**” below) – and one semi-crystalline material – the polyoxymethylene Delrin 100 NC-10 of DuPont (“**POM**” below) – were (arbitrarily) chosen. One run of normal processing conditions (“**fast**” below) and one of slow filling (“**slow**” below) were simulated for each material. The triangle sides were chosen extreme (60 cm) to provoke freezing. The plate thickness is 2 mm. The comments below on Cmd are solely based upon these four simulation runs. According to the materials documentation, the Cmd model assumes constant heat conductivity, constant diffusivity and the existence of a no-flow temperature. These temperatures deviate a lot from the reported melting point $T_M = 178^\circ\text{C}$ for Delrin (DuPont product information, www.dupont.com/enggpolymer) and from the glass transition temperature $T_G = 100^\circ\text{C}$ for Polystyrol (MatWeb, www.matweb.com). The latent heat of crystallization seems to be neglected. The density variations are described by a Carreau PVT model – cf. [Kennedy], p.28-29. The viscosity obeys a model of $T, \dot{\gamma}$ that includes 2 universal and 5 material specific parameters, according to [Kutschera] – for Delrin see **Figure 5.1**, which we have constructed from the Cmd input data. Here the overall increase by T for fixed $\ln \dot{\gamma}$ is indeed questionable. However, for comparison we have adjusted the FD Arrhenius parameter of η in a best-fit estimation procedure to this questionable behaviour.

In **Table 5.1** all materials data of the simulation runs are collected, together with our fitted parameters, marked by asterisks. Our FD densities are estimated from the Cmd PVT model, and our heat capacities are then determined by the given diffusivity values.

In the Cmd runs, as a simplifying option, the metal mould has not been explicitly modelled. According to [Kutschera], the contact temperature at the inner wall surface is computed from standard wall conductivity and diffusivity, and prescribed wall temperature. The exact model is unknown to us. To match that model we have used the standard Moldflow mould wall parameters – see **Sec. 4.2** – and have applied a constant depth of the cooling channels, $H_w = 9\text{ cm}$, the rounded average in the Moldflow runs.

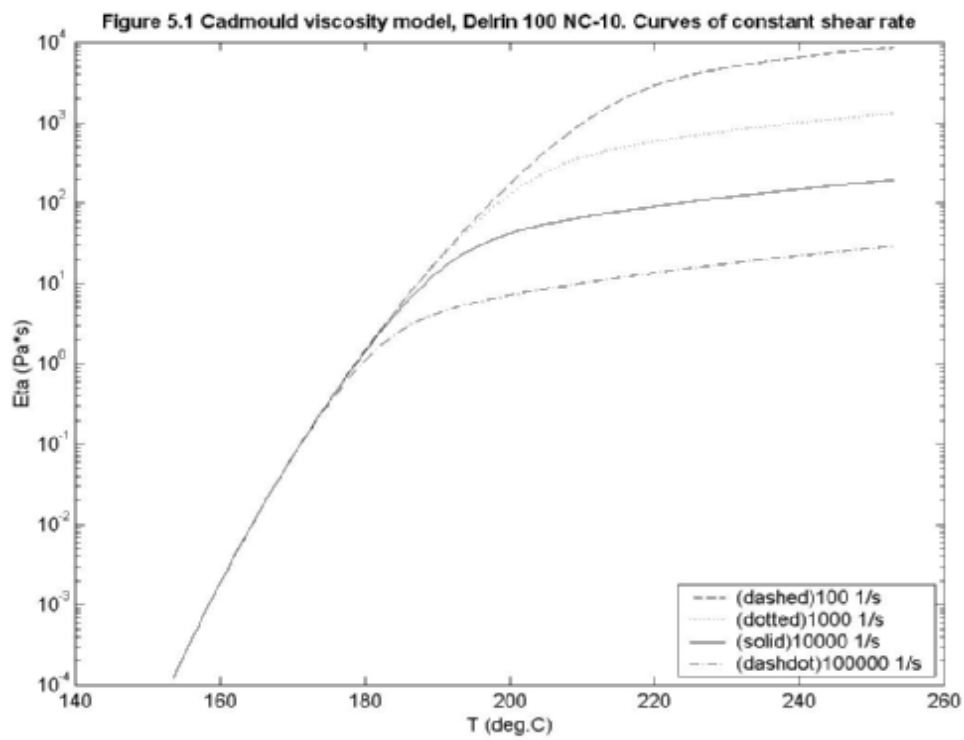


Table 5.1 Materials data used in basic FD runs			
	Polystyrol 158 K	Delrin 100 NC-10	
ρ_ℓ	1015*	1240*	kg/m ³
ρ_s	1045*	1320*	kg/m ³
$\lambda_\ell = \lambda_s$	0.14	0.158	W/m °C
$c_{p,s}$	1473	2708	J/kg °C
$c_{p,\ell}$	1517	2883	J/kg °C
$\eta = K_0 \cdot e^{B/(T-T_B)} \cdot \dot{\gamma}^{n-1}$	K_0 445.74*	316352*	Pa · s ⁿ
	B 2005.2*	-184.76*	°C
	T_B -273.2	141.79*	°C
	n 0.24836*	0.37405*	
H_L	---	0	J/kg
$T_{no-flow}$	130	153	°C

5.3 Comparison runs

5.3.1 Average temperature

The Cadmould (Cmd) runs assume “pressure-controlled filling 99%”. Since no explicit pressure bound seems to be prescribed, we interpret this as if the pressure registered at the inlet, when 99% of the cavity volume is filled, is dimensioning and is kept constant throughout the rest of the filling phase. In practice this means a successive reduction of the final flow rate.

During the first 99% of filling a constant flow rate is applied, chosen to provide the prescribed 99%-filling times 2.006 s (run PS-fast) and 8.000 s (run PS-slow), respectively. This causes big differences between the runs in resulting temperatures – see **Figure 5.2** for a general view of the final average temperatures in our FD runs, presented on one and the same colour scale. The steep temperature rise at the corner rays are subject to several comments below. If the nominal residence times, computed in the absence of freezing and for a plug-formed v_r -velocity profile, were decisive to the result, the coldest regions would be along the triangle sides, and there would be no reversing of temperatures along any stream ray from the inlet and outwards.

Both our FD runs on the high viscosity POM Delrin have failed: In run POM-slow, although our FD method works, the vertical temperature profiles are characterized by a narrow peak of extremely high temperature (and viscous energy), originating in the last second of filling simulation. In run POM-fast the Jacobian matrix \mathbf{G} in **Sec. 3.3.2** becomes ill-conditioned (by $B < 0$) and the backup routine is not sophisticated enough to provide acceptable convergence from the chosen starting point. Since the temperatures even in run POM-slow of Delrin become non-physically high, we have not worked on improving our method to handle run POM-fast as well. A plausible explanation for the failure is the non-physical Cmd viscosity model for this material – see **Fig. 5.1** – also remaining in our model – see **Tab. 5.1**, where the negative B -value indicates that the viscosity increases by temperature. Since the volume flow rate is prescribed, the high K_0 -value causes high viscous energy levels and correspondingly high temperatures, which add to the viscosity instead of acting as the ordinary stabilizing mechanism. The severity of these extreme input data is reinforced by the shortcomings of our model as discussed below, revealed as the flow sectors are narrowing. For these reasons we will limit our discussion to the two PS-runs.

A Cmd result data file documents the state at the end of filling, as to pressure, temperature, shear stress, velocity and frozen layer. According to the Cadmould file name convention, the whole filling phase takes 2.054 s in run PS-fast and 8.368 s in run PS-slow. Our corresponding times are 2.082 s and 8.277 s, respectively. The time deviations are attributed to pressure differences. The Cadmould pressure data indicate final levels at the inlet around 650 bar in run PS-fast and 800 bar in run PS-slow. These are contradictory to our interpretation of “pressure-controlled filling 99%”, both as to magnitude and relation: Our dimensioning 99%-pressures become 1177 bar in run PS-fast (after 2.005 s) and 1027 bar in run PS-slow (after 8.011 s). As for relations, a higher pressure level is expected in run PS-fast than in run PS-slow due to the higher flow rate. As for the pressure magnitudes, we see some weaknesses of our distance model, where the active flow angle concept (cf. **Sec. 5.1**) assumes rigid boundaries between streaming and stagnant fluid. In practice we would expect these boundaries to be flexible, admitting some tangential outflow to the stagnant sectors close to the inlet in a high-pressure situation and compensated by tangential inflow ahead of the flow

5.3 Comparison runs

front. We might instead use the term *effective flow angle* to describe these phenomena. As an illustration, see **Figure 5.9** below for “run PS-fast-E”, which denotes run PS-fast with the addition of a 10° flow angle, whenever possible, to each side of every active flow sector in the FD run, i.e. the overall effective flow angle is $60^\circ (= 3 \cdot (10 + 10))$ more than the nominal angle at the end of filling. **Fig. 5.9a-b** should be compared with **Fig. 5.3a** and **Fig. 5.4c**, respectively – see comments below. The final pressure at the inlet in FD run PS-fast-E is 901 bar, and the filling takes 2.039 s. We have not developed the concept effective flow angle further, but it might be relevant also in case of non-star shaped cavities, where flow around corners causes singularities, if the strict distance model is applied.

The vertical average temperatures, computed for different node positions (r, φ) at the end of filling, are presented in **Figures 5.3-5.6**, where **Fig. 5.3-5.4** refer to run PS-fast and **Fig. 5.5-5.6** to run PS-slow. The plot symbols for the Cmd values differentiate between cavity nodes at the upper wall surface $z = +1$ and at the lower surface $z = -1$. Due to triangular symmetry, nodes of equal r and equal φ – deviation from the closest corner ray (from inlet to triangle corner) are equivalent as to temperatures, etc. The φ – deviation 0° corresponds to nodes on a corner ray – the three final flow directions – and 60° refers to nodes on a midside ray – the three directions of first stagnation. In **Fig. 5.3, 5.5** the node rays are grouped into 3° φ – deviation classes, of which a subset is presented. Especially in run PS-slow there are extreme differences – more than 100°C near the inlet – between the Cmd temperatures registered for the $z = +1$ - and $z = -1$ -nodes, respectively. According to [Kutschera] both are average nodal values from wall to wall ($-1 \leq z \leq +1$). Even if the vertical positions are weighted differently for the two node groups and if the implicit Cmd cooling model handles the upper and lower part differently, we have no obvious explanation for such big differences. Notwithstanding this big temperature span of Cmd, our FD temperatures show systematic deviations. In **Fig. 5.3a** all nodes close to the corner rays are plotted. Our FD temperatures are higher, except at the inlet ($r = 0$) and at the mould wall ($r \approx 0.35\text{ m}$). For each plot in **Fig. 5.3** the FD temperatures fall in relation to the Cmd temperatures – except at the mould wall. The same phenomenon appears for the six radial classes in **Fig. 5.4a-e**, where the Cmd temperatures decrease much slower tangentially, from the final flow direction (φ - deviation = 0°) to the direction of first stagnation (φ - deviation = 60°). The overall average fluid temperatures Cmd-FD coincide, 187°C . In run PS-slow, **Fig. 5.5-5.6**, the overall average temperatures differ, 132°C for FD and 139°C for Cmd. When the strict distance model is applied in run PS-fast, we contribute some of the discrepancies to our above mentioned negligence of tangential convection, to which our negligence of tangential conduction should be added, together preventing any tangential temperature levelling. On the other hand, an increased steepness near φ - deviation = 0° is expected due to finally accelerating shear rates, instead of the levelling out that the Cmd temperatures show in **Fig. 5.4**.

Figure 5.2a Run PS-fast: FD. Vertical average temperature (deg.C) at the end of filling, $t=2.08(s)$

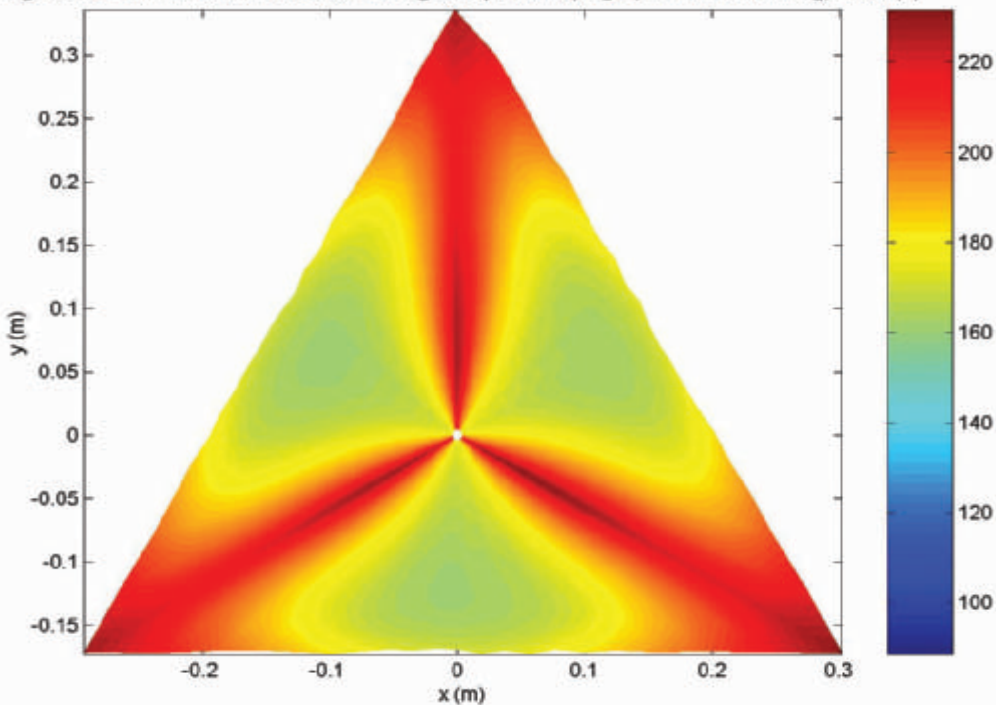
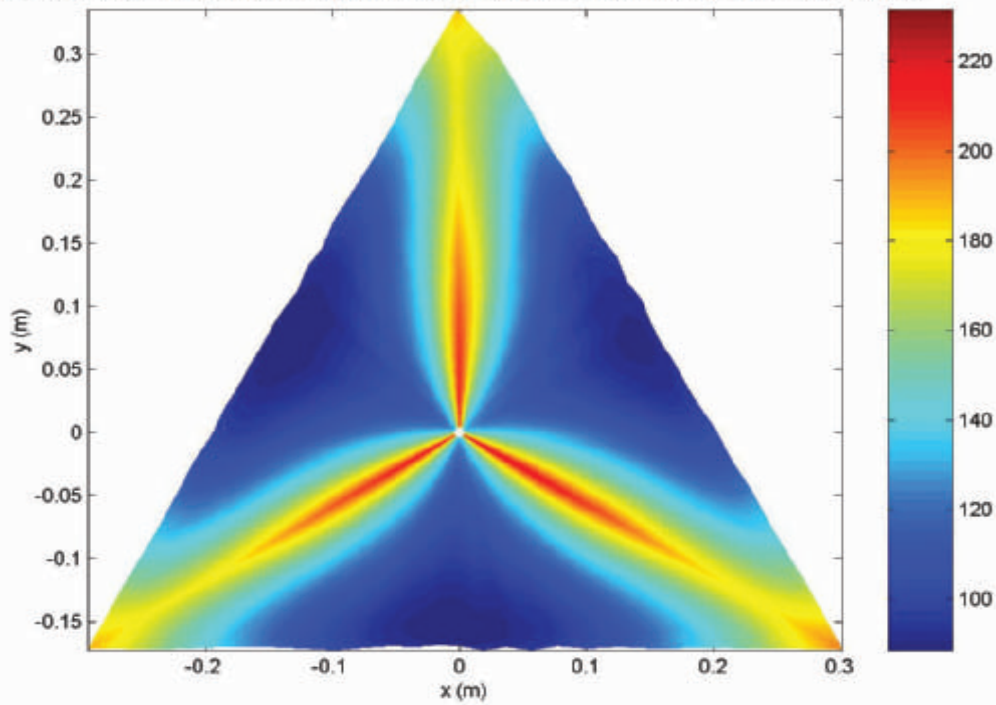


Figure 5.2b Run PS-slow: FD. Vertical average temperature (deg.C) at the end of filling, $t=8.28(s)$



5.3 Comparison runs

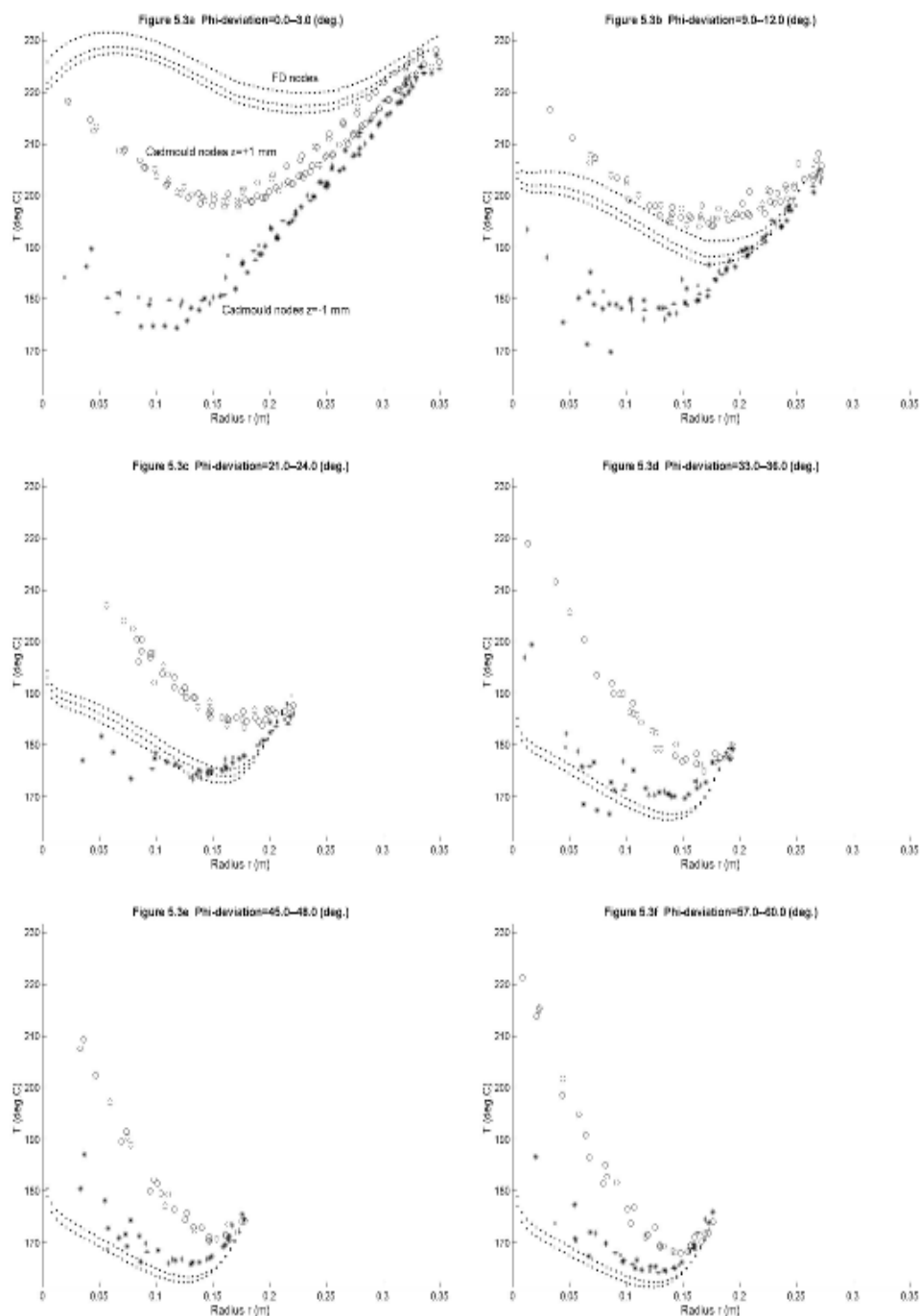


Figure 5.3 Run PS-fast: Cmd and FD. Vertical average temperatures at the end of filling. Rays of different φ - deviations, measured from the closest corner ray.

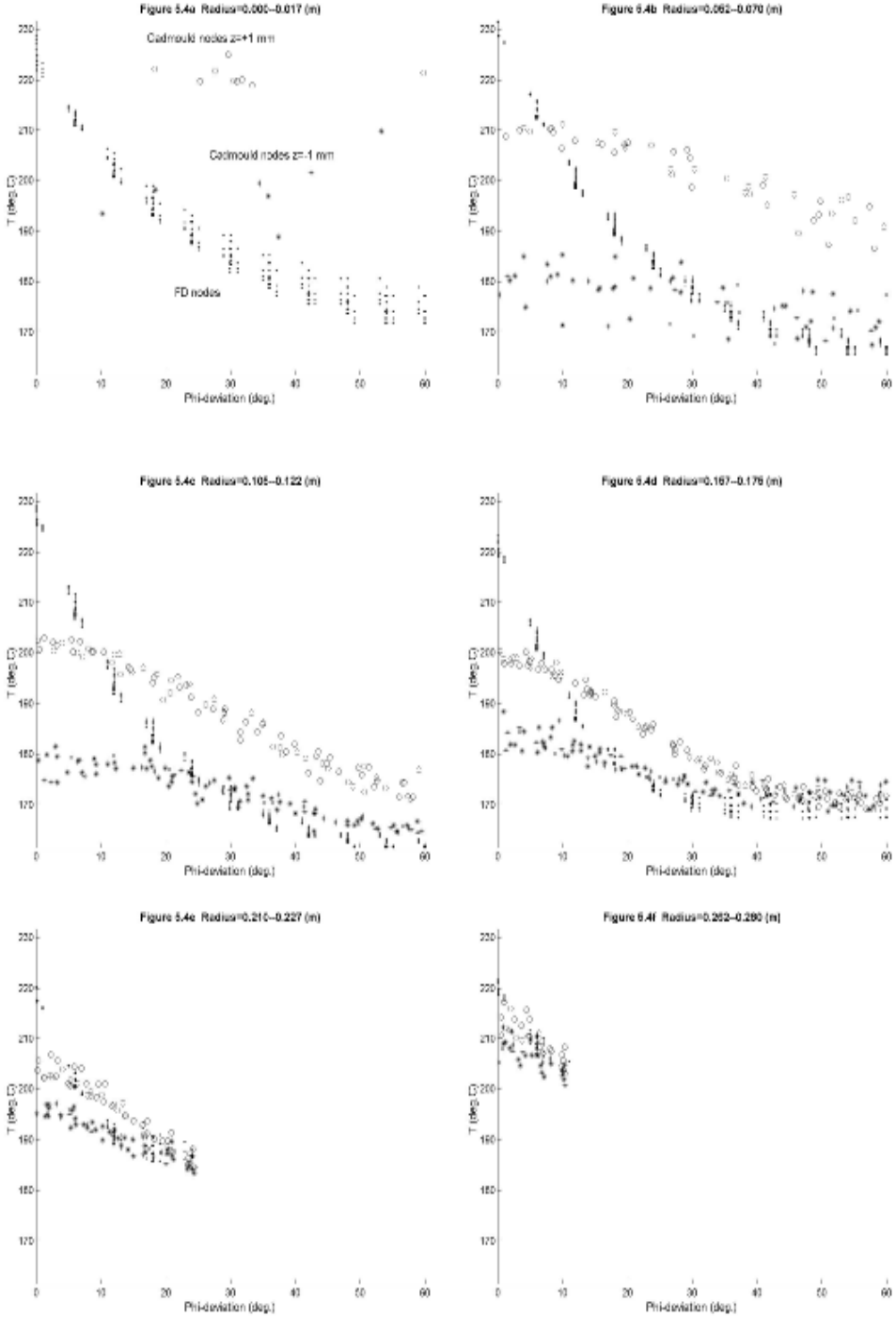


Figure 5.4 Run PS-fast: Cmd and FD. Vertical average temperatures at the end of filling. Different concentric circles.

5.3 Comparison runs

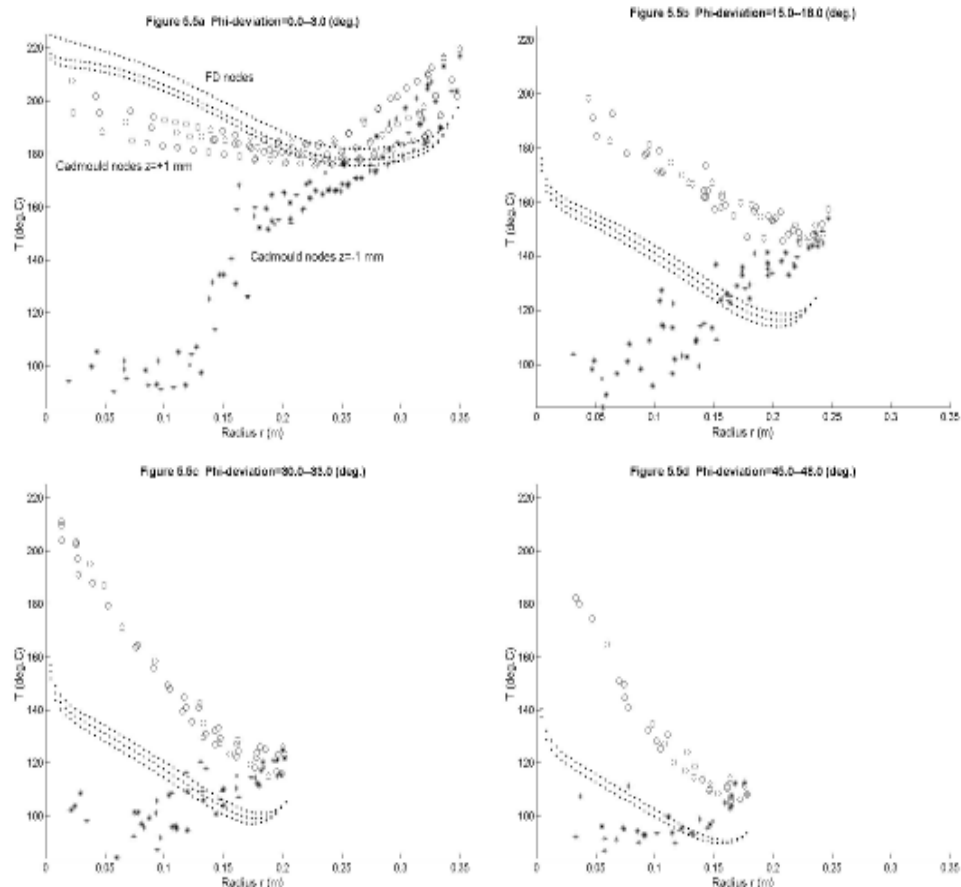


Figure 5.5 Run PS-slow: Cmd and FD. Vertical average temperatures at the end of filling. Rays of different φ – deviations, measured from the closest corner ray.

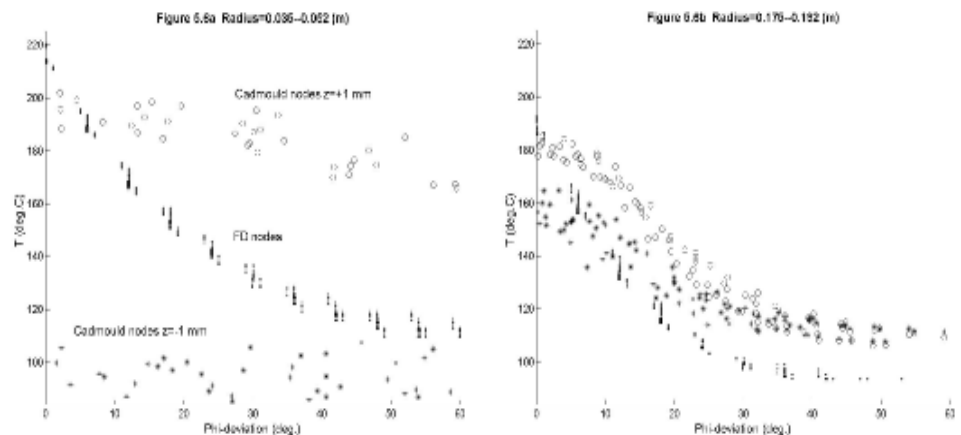


Figure 5.6 Run PS-slow: Cmd and FD. Vertical average temperatures at the end of filling. Different concentric circles.

Figure 5.7a Run PS-slow: FD. Temperature T (deg.C) at the end of filling, t=8.28(s). Corner ray.
Contour of frozen layer, no-flow temp. 130 deg.C

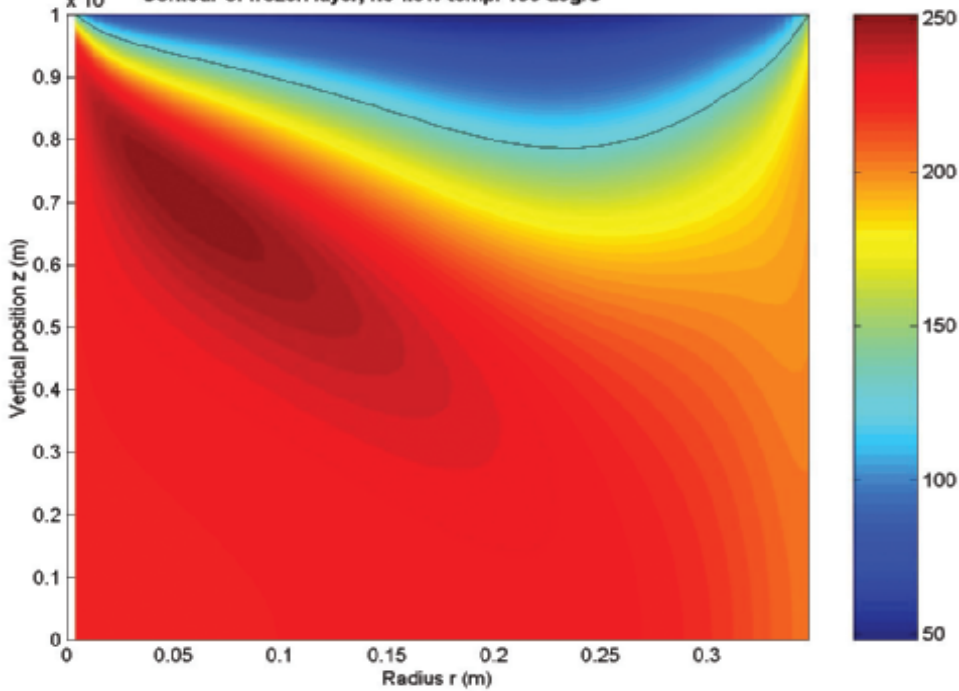
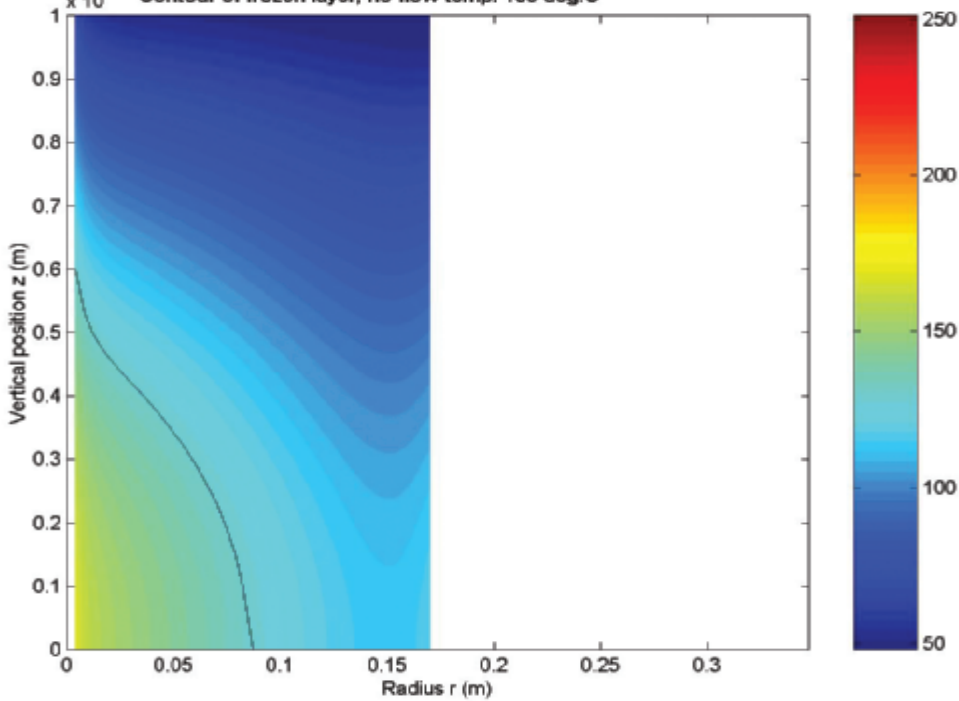


Figure 5.7b Run PS-slow: FD. Temperature T (deg.C) at the end of filling, t=8.28(s). Midside ray.
Contour of frozen layer, no-flow temp. 130 deg.C



5.3 Comparison runs

Figure 5.8a Run PS-slow: FD. Vertical temp.profile $T(z)$ of streaming fluid. Node radius $r=0.004$ (m)

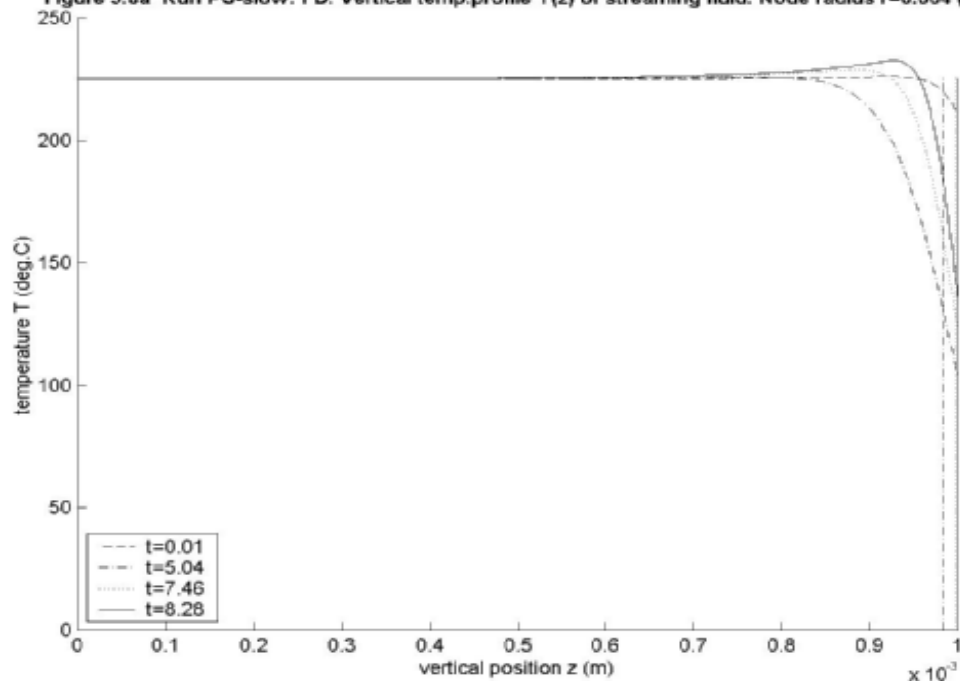
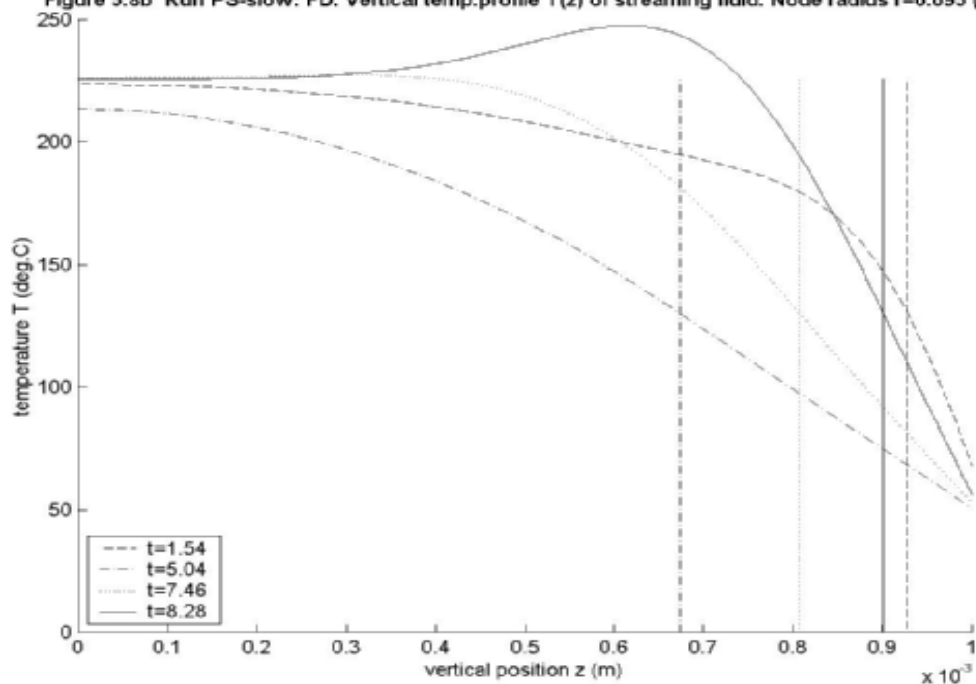


Figure 5.8b Run PS-slow: FD. Vertical temp.profile $T(z)$ of streaming fluid. Node radius $r=0.095$ (m)



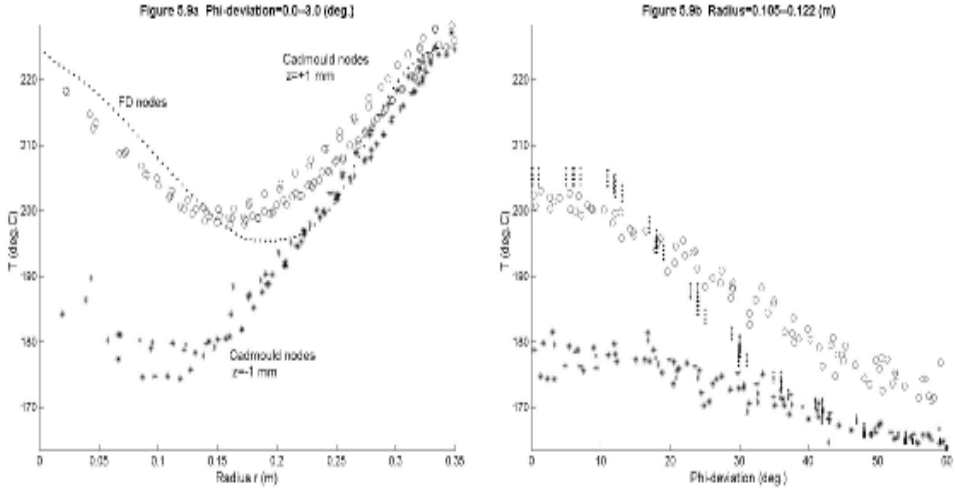


Figure 5.9 Run PS-fast-E: Cmd and FD (effective flow angle: $+60^\circ$). Vertical average temperatures at the end of filling. (a): rays of similar φ – deviations, measured from the closest corner ray, (b): concentric circles of similar radius.

5.3.2 Temperature profiles

In **Figure 5.7a-b** we illustrate the temperature contrast at the end of filling in run PS-slow, between two flow directions – a corner ray is shown in **Fig. 5.7a** and a midside ray (where the fluid hits the wall after 4.83 s) in **Fig. 5.7b**. One and the same colour scale is used. In **Fig. 5.7b** part of the fluid is frozen to the bottom, in **Fig. 5.7a** we recognize the frozen layer profile from **Ch. 4**, with the maximum layer thickness far from the inlet. In **Figure 5.8a-b** we consider the time evolution of vertically registered temperatures, at two nodes chosen on a corner ray. At the inlet – see **Fig. 5.8a** – a thin frozen layer is built up initially, but towards the end of filling the increased pressures, velocities and shear rates make the layer melt. At 9.5 cm from the inlet – see **Fig. 5.8b** – the same kind of evolution is even more pronounced – two thirds of the layer that exists at 5.05 s are molten at the end of filling. (This phenomenon, but far more extreme, is decisive for our Delrin simulation failures. Realistic or not: our model behaves like this when the flow is confined to narrowing flow sectors.) The final temperature rise is also traced as the hot spot in **Fig. 5.7a**. This is also an explanation for the slow fall of the FD average temperature in **Fig. 5.5a** (run PS-slow) and for the initial rise by radius in **Fig. 5.3a** (run PS-fast). Comparisons with the Cmd frozen layers in run PS-fast for all nodes in two φ – deviation classes are shown in **Figure 5.10a-b** below. The Cmd bottom layer is much thicker than the top layer, for unknown reasons, if not for the implicit cooling. As can be seen in **Fig. 5.10a** for the corner rays, the Cmd maxima at the lower and upper walls occur at a smaller radius than the corresponding FD value. There is a systematic change of FD maximum position and value as the φ – deviation angle increases, while the Cmd maxima are essentially constant – both as to radial position and, especially at the lower wall surface, as to extension. Before the (local) time of stagnation the relative, rather than the absolute, position along a flow line is expected to be decisive for the maximum. At the end of filling a tangential heat flow, which we completely ignore, might have accomplished some levelling, but the almost full angular symmetry of the Cmd frozen layers is hard to understand.

5.4 Method performance

5.4.1 Square-root parameter

To predict the frozen layer thickness $\delta = H - h$ after a new time step, a $\sqrt{t - t_{act}}$ -increase (cf. **Sec. 3.1.3**) is optional in our simulation program, both for the streaming fluid and in the stagnant regions. For the streaming fluid in run PS-fast this option does not perform better than to start the h -iterations (h is the non-frozen height) from the previous value, without extrapolation. A glance at **Fig. 5.8** explains this, since the normal increase during the first seconds is followed by a shrinking layer. In run PS-slow a 50-50-weighted combination of the latest square-root coefficient, computed as $\delta/\sqrt{t - t_{act}}$, and the previously registered average coefficient performs better. In the stagnant phase the growth rate (faster) differs radically from that of the streaming fluid. Therefore a node specific, equivalent activation time t_{act} is estimated initially and used thereafter. By extrapolating the latest registered expansion rate, according to the square-root formula, a few percent of the h -iterations are saved.

5.4.2 Iteration statistics

Since the stagnant phase, for fixed h and with constant parameters, represents linear systems of equations in each phase, liquid and solid, we expect the Newton temperature iterations to converge in one step to the solution. This is accomplished – always with step length 1 – if we avoid applying an upper limit of accepted temperature changes per iteration; which is used in the nonlinear case. The average number of iterations per program call, for the computation of a new h -solution (for fixed node and time), is the same as in **Ch. 4** (with nonlinear viscosity and temperature dependent parameters): 6.31 h -iterations per call in the streaming phase and 6.73 in the stagnant phase for run PS-fast. The rather tough convergence criterion used, with an overall residual squared sum $F = \mathbf{f}^T \mathbf{f}$ below 10^{-12} for $J = 80$ vertical node levels, is no problem. Stop values in **Flowchart 3.1** are $FTEps = 1.665 \cdot 10^{-14}$, $FhEps = 10^{-5}$ and $hEps_1 = 5.3 \cdot 10^{-8}$. The whole run, with extensive checking and saving on files, takes a few minutes if $K = 84$ time steps (radial levels), $uPhi = 20$ nodes per radial level and $J = 80$ are used.

5.4.3 Velocity profiles and residence time

In this application we have used two terms only in the power series expansion of viscosity and velocity components. Apart from the isothermal exponent $1 + \frac{1}{n}$ in (3.4), the estimated exponent of the additional term always becomes $3 + \frac{1}{n}$. The velocity components can be used for computing the residence time, or equivalently, the time of injection for the stagnant fluid at the end of filling. In **Figure 5.11a** the vertical average time of injection is shown for the triangle, in **Figure 5.11b** the vertical distribution is plotted for a corner ray. Due to the hot, fast moving material at the centre plane, redirected vertically at the front, and to the freezing followed by melting as the shear rate increases at the walls, the pattern becomes complex. **Fig. 5.11a** can be compared with **Fig. 5.2a**. The distributions of residence time (time of injection) and the average temperature are similar, although both show a non-standard behaviour, influenced by local freezing and succeeding melting.

Figure 5.10a Run PS-fast: Cmd & FD. Frozen layer at the end of filling. Phi-deviation=0.0–3.0 (deg.

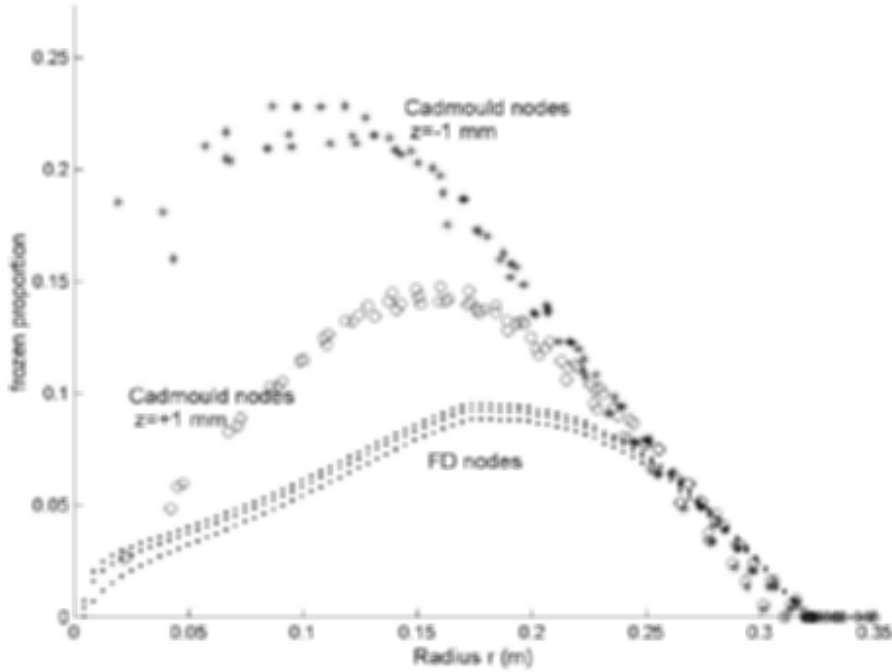


Figure 5.10b Run PS-fast: Cmd & FD. Frozen layer at the end of filling. Phi-deviation=15.0–18.0 (deg

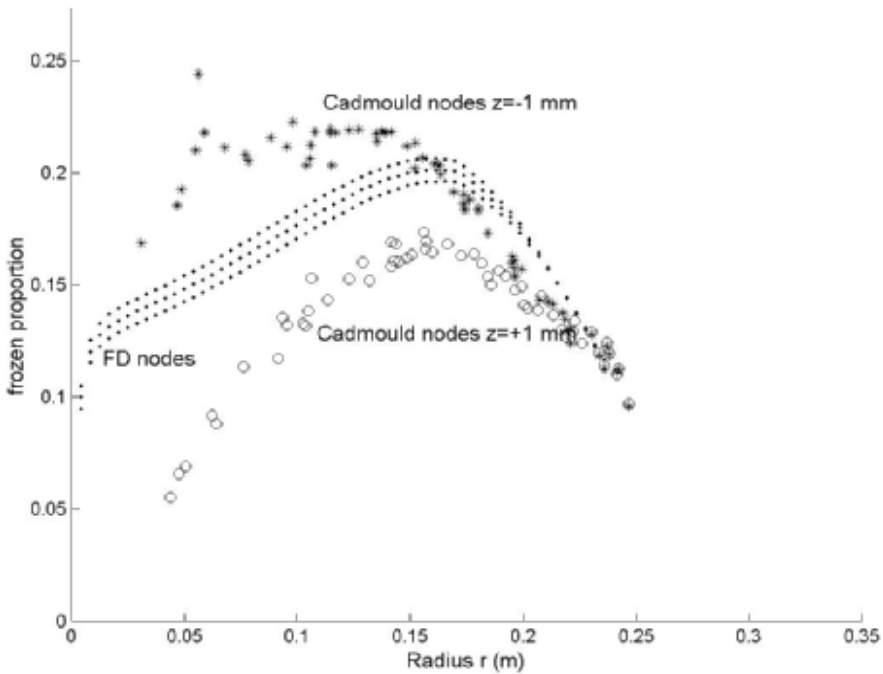


Figure 5.11a Run PS-fast: FD. Vertical average time of injection (s) at the end of filling, $t=2.08(s)$

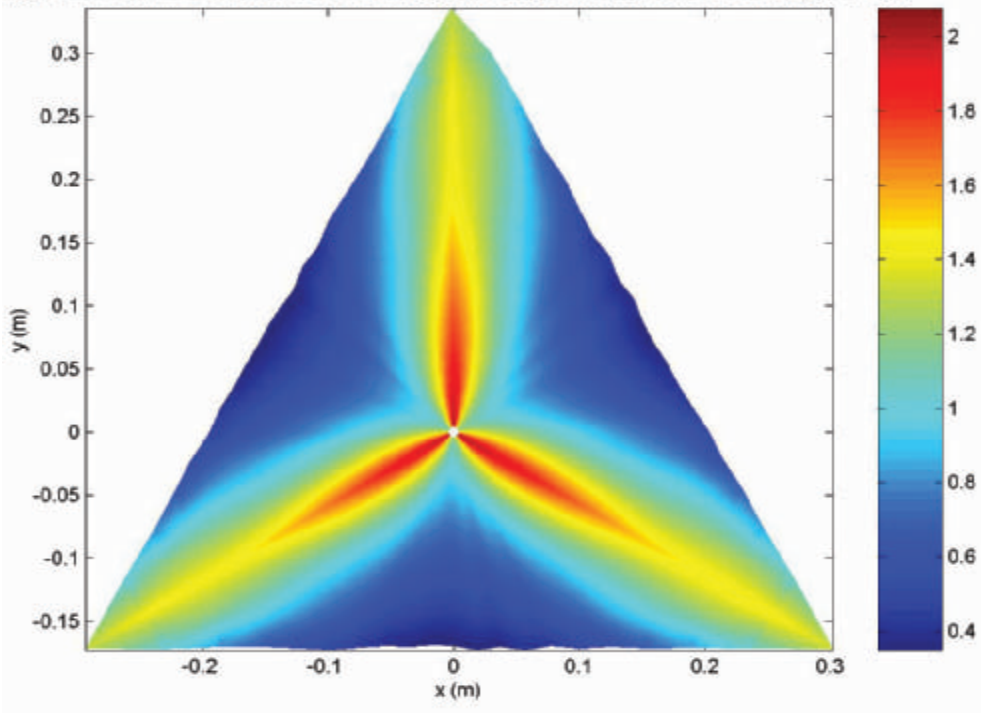
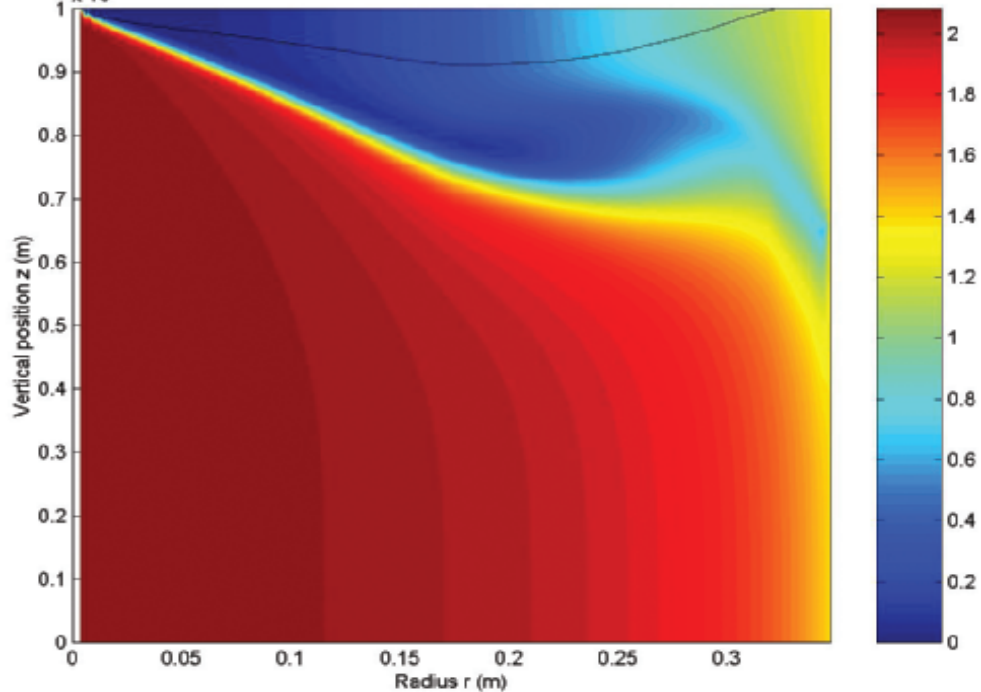


Figure 5.11b RunPS-fast: FD. Time of injection (s) at the end of filling, $t=2.08(s)$. Corner ray. Contour of frozen layer, no-flow temp. 130 deg.C



6 Conclusions

In the two implemented radial flow applications the plus points for our FD program are:

- It admits variable material properties of both melt and metal mould (**Sec. 2.2, 3.2.5**).
- It can be run with material and process input data similar to those used in commercial programs.
- Some interaction between the momentum and energy equations is considered by an analytical pressure-velocity model, fitted to FD-computed temperatures via a linking viscosity (**Sec 3.1**).
- Fairly realistic temperature profiles in **Fig A1.1** (cf. **Fig. 4.9**) indicate that our analytical link with the pressure-velocity fields replaces a FEM model reasonably well. The stable velocity profiles in **Fig. A1.1** support our approximation by a common profile along the flow ray.
- It takes full advantage of the symmetries, streaming fluid being handled by a single flow ray and stagnant fluid by one representative for each node group sharing flow history.
- We use the possibilities to simplify the basic PDE in regions of stagnant fluid and in cavity parts of “solid”, “frozen” fluid.
- The axial node spacing can be chosen non-uniform, adjusted to a steeper temperature variation at the cavity wall, without jeopardising the numerical accuracy (**Sec. 3.3.1**).
- The resulting nonlinear systems of FD-equations are small, efficiently solved on a standard PC.
- For realistic materials our solution method is reasonably robust, being supported by theoretical and practical convergence results (**Sec. 3.2, 3.3.2, 4.5, 5.4**).
- The qualitative agreement FD - Mfl (Moldflow) and FD - Cmd (Cadmould) is acceptable/good, as a rule, both for pressure evolution (**Fig. 4.5**) and temperatures (**Sec. 4.3.2, 5.3.1**).

In the comparison runs with the two commercial FEM-FD programs we notice big temperature differences in two cases:

- At the flow front (FD - Mfl). We refer this to different PDE-formulations of axial heat flow (**Sec 2.3.3** and [Kennedy], p.71). Our two front models, conventional convection and fountain flow (cf. **Fig. 4.8**), are unanimous in this respect, and we claim they are realistic.
- In narrow flow sectors (FD - Cmd). We explain this by our negligence of angular convection and conduction. The discrepancy is fatal for a material with unrealistic viscosity dependence upon temperature. Although our FD-method converges in one such run, the rapid temperature rise in the diminishing flow sectors is unrealistic. An isothermal viscosity model would perform better here but worse on realistic material models. Our decisive model weakness is an exaggerated shear rate (**Sec. 5.3.1**).

As for the commercial programs we are critical in some respects, with reservations for our limited study and insight:

- Some basic material data and some modelling methods show questionable quality: different values are found in different data bases, and unrealistic data are indiscriminately used (**Sec. 4.2, 5.2, 5.3.1**).
- The realism of some parts of the material model might be improved: the viscosity model should rely on known asymptotic results and – according to our findings in **Sec. 4.4** – also allow pressure-dependence, and the material model should admit temperature-dependent thermal conductivity, specific and latent heat. (However, we have not set an example, in relying on the power-law behaviour with fixed index n .)
- The asymmetry between the upper and lower cavity halves is in some cases extreme, for unknown reasons (**Fig. 4.9-10, 5.3-6**).
- The axial heat convection, especially at the flow front, should not be ignored (Mfl; the Cmd model is unknown to us).
- The angular stretching part of the shear rate should not be neglected in radial flow (**Sec. 2.3.3** and [Kennedy], p.70).

Some observations of the general filling process are:

- Our radial temperature profile takes its minimum and the frozen layer is thickest closer to the inlet than suggested by Mfl (FD - Mfl: **Fig. 4.8, 4.10**). We consider this to be an implication of the different axial heat models at the front.
- The axial temperature profiles and the frozen layer thickness show non-monotone evolution by time (FD: **Fig. 5.11b**). We explain this by local viscous heating and melting caused by increased shear rates in narrowing flow sectors. (Hence our effect might be somewhat exaggerated.)

Our main experience and insight is:

- As for the narrow flow sectors, in relying on the commercial program Cmd, we must admit the shortcomings of the distance model and our 2D heat flow principle, even in a triangular case (cf. **Fig. 5.4**). Although we have mentioned the possibility to modify our principle (by the concept of an effective flow angle, **Fig. 5.9**), such a modification is hard to implement in a general case. In this sense our 2D temperature model fails to be equally robust as the distance model itself. For educational purposes, on the other hand, even a 2D FD-model is too sophisticated to balance the simplicity of the distance model.
- As a by-product we have formulated two different analytical forms of temperature solutions – see **App. 1-2** – based on our pressure-velocity model and on an extended Stefan problem, respectively. These or similar classes of temperature profiles are hopefully robust, e.g. in narrow flow sectors and in complex geometries, simple enough to be transparent and yet capture the main variation. In the development of such standard profiles our FD program might be of some value.

References

- Advani, S.G. (ed.), *Flow and Rheology in Polymer Composites Manufacturing*, Elsevier, Amsterdam, 1994.
- Agassant, J.-F. et al, *Polymer Processing*, Munich, 1991.
- Ames, W. F., *Nonlinear Partial Differential Equations in Engineering*, vol. I, Academic Press, New York, 1965.
- Aronsson, G., On p-harmonic functions, convex duality and an asymptotic formula for injection mould filling, *European J. Appl. Math.* **7** (1996), 417-437.
- Baehr, H.D. and Stephan, K., *Heat and Mass transfer*, Springer, Berlin, 1998.
- Baird, D.G. and Collias, D.I., *Polymer Processing*, Butterworth-Heinemann, Newton, MA, 1995.
- Becker, J., Berggren, K., Nilsson, L.-Å., Strömvall, H.-E., *Formsprutningsteknik*, Yrkesnämnden för fabriksindustrin (YFIND), Stockholm, 2000.
- Berins, M.L. (ed.), *Plastics Engineering Handbook of the SPI*, 5th ed., Chapman & Hall, New York, 1991.
- Bicerano, J., *Prediction of Polymer Properties*, Dekker, New York, 1993.
- Birkhoff, G. and Rota, G.-C., *Ordinary Differential Equations*, John Wiley, New York, 1989.
- Carslaw, H.S. and Jaeger, J.C., *Conduction of Heat in Solids*, Oxford Univ. Press, Oxford, 1959.
- Dennis, J.R. & Schnabel, R.B., *Numerical methods of unconstrained optimization and nonlinear equations*, Prentice-Hall, Englewood Cliffs, NJ, 1983.
- Gustafsson, B., Kreiss, H.-O. and Oliger, J., *Time Dependent Problems and Difference Methods*, Wiley, New York, 1995.
- Hieber, C.A. and Shen, S.F., A finite-element/finite-difference simulation of the injection-molding filling process, *J. Non-Newtonian Fluid Mech.* **7** (1980), 1-32.
- Holman, J.P., *Heat Transfer*, McGraw-Hill, New York, 1997.
- Horn, R.A. & Johnson, C.R., *Topics in matrix analysis*, Cambridge Univ. Press, Cambridge, 1991.
- Isayev, A.I. (ed.), *Injection and Compression Molding Fundamentals*, Dekker, New York, 1987.
- Johansson, P., *On a Weighted Distance Model for Injection Moulding*, LiU-TEK-LIC-1997:05, thesis No. 604, Linköping, 1997.
- Kennedy, P., *Flow Analysis of Injection Molds*, Hanser, Munich, 1995.
- Kutschera, H., (*Personal comm.*), Simcon kunststofftechnische Software GmbH (producer of Cadmould).
- Manzione, L.T. (ed.), *Applications of CAE in Injection Molding*, Hanser, New York, 1987.
- Meyer, C.D., *Matrix Analysis and Applied Linear Algebra*, SIAM, Philadelphia, 2000.
- Morton-Jones, D.H., *Polymer Processing*, Chapman & Hall, London, 1989.
- Nilsson, L.-Å., (*Personal comm.*), PolyInvent AB (distributor of Cadmould in Sweden).
- Ortega, J.M., *Matrix theory*, Plenum Press, New York, 1987.
- Ortega, J.M. and Rheinboldt, W.C., *Iterative Solution of Nonlinear Equations in Several Variables*, Academic Press, New York, 1970.
- Pearson, J.R.A., *Mechanics of Polymer Processing*, Elsevier, Barking, Essex, 1985.
- Perepechko, I., *Low-temperature Properties of Polymers*, Mir, Moscow, 1980.
- Rao, N.S., *Design Formulas for Plastics Engineers*, Hanser, Munich, 1991.
- Renardy, M. and Rogers, R. C., *An Introduction to Partial Differential Equations*, Springer, New York, 1993.

Siginer, D.A., DeKee, D. and Chhabra, R.P. (ed.s), *Advances in the Flow and Rheology of Non-Newtonian Fluids*, Part B, Elsevier, Amsterdam, 1999.

Smith, G.D., *Numerical Solution of Partial Differential Equations: Finite Difference Methods*, Clarendon Press, Oxford, 1985.

Storck, K., *Thermal system analysis: heat transfer in glass forming and fluid temperature-control systems*, LiU dissertation No. 542, Linköping, 1998.

Straughan, B., *The Energy Method, Stability, and Nonlinear Convection*, Applied Math. Sciences 91, Springer, New York, 1992.

Strikwerda, J. C., *Finite Difference Schemes and Partial Differential Equations*, Wadsworth, Belmont, CA, 1989.

Tadmor, Z. and Gogos, C.G., *Principles of Polymer Processing*, Wiley, New York, 1979.

Tucker, C.L. (ed.), *Fundamentals of Computer Modeling for Polymer Processing*, Hanser, Munich, 1989.

Valtonen, M., (*Personal comm.*), Tampere University of Technology, Institute of Materials Science, Plastics and Elastomers Technology.

Van Krevelen, D.W., *Properties of Polymers*, Elsevier, Amsterdam, 1990.

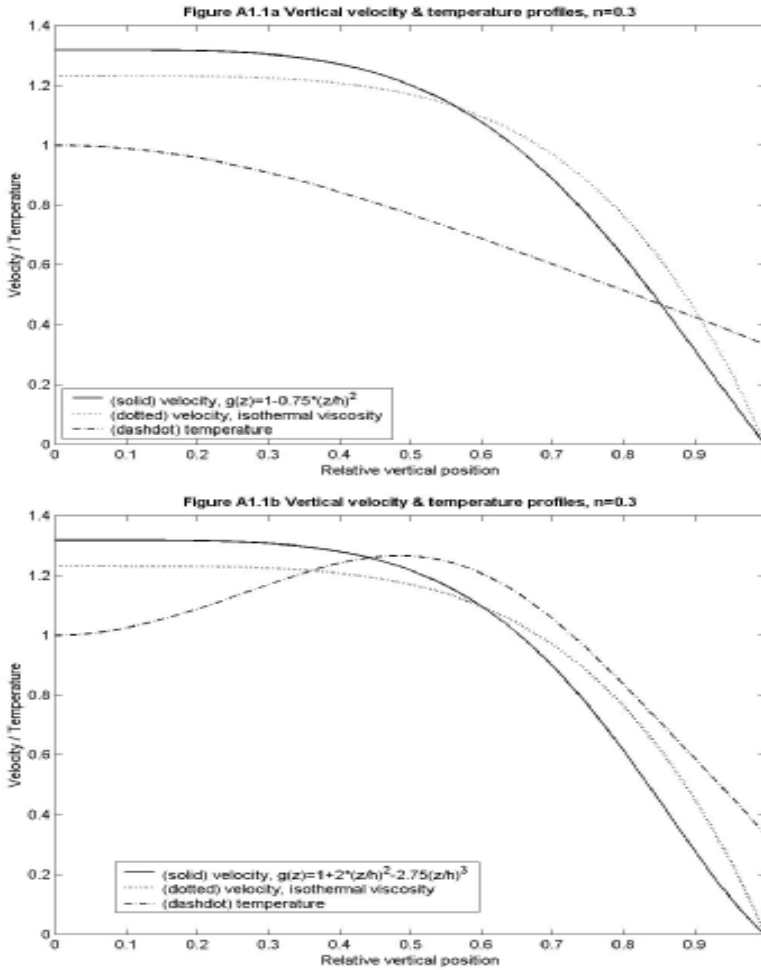
Özisik, M.N., *Finite Difference Methods in Heat Transfer*, CRC Press, Boca Raton, Fla, 1994.

Appendix 1 Vertical velocity profiles

As one example, consider (3.1) with the special choice $g\left(\frac{z}{h}\right) := 1 - \frac{3}{4} \cdot \left(\frac{z}{h}\right)^2$ for $|z| \leq h$, $h \leq H$. The viscosity increases as $|z| \uparrow h$ by the factor $\dot{\gamma}^{n-1}$ and here, due to the temperature gradient, also by the factor $e^{B(T-T_B)}$. The no-slip boundary condition $V(h) = 0$ implies

$$V(z) = \frac{c^{\frac{1}{n}}}{1 + \frac{1}{n}} \left(1 - \left| \frac{z}{h} \right|^{1 + \frac{1}{n}} \right) - \frac{3}{4} \frac{c^{\frac{1}{n}}}{3 + \frac{1}{n}} \left(1 - \left| \frac{z}{h} \right|^{3 + \frac{1}{n}} \right), \quad c^{\frac{1}{n}} = \frac{(2 + \frac{1}{n})(4 + \frac{1}{n})}{\frac{5}{2} + \frac{1}{4n}};$$

corresponding to the two leading terms of the series expansion (3.4). The velocity profile becomes less plug-like than for the isothermal case – see **Figure A1.1a**. Unlike the isothermal case, maximum shear rate does not occur at the very no-flow boundary, but inside (cf. [Manziona], p.259, and [Pearson], p.610). A corresponding temperature profile, based upon (3.2), is illustrated.



As a second example we choose $g\left(\frac{z}{h}\right) := 1 + 2 \cdot \left(\frac{z}{h}\right)^2 - \frac{11}{4} \cdot \left(\frac{z}{h}\right)^3$ – see **Figure A1.1b**. Although the velocity profiles in **Fig. A1.1a,b** are quite similar, the temperature profiles differ a lot – cf. the assumption in **Sec. 3.1.1** of a common $V(z)$ and the temperature profiles in, e.g., **Fig. 4.9**.

Appendix 2 Further comments on the Stefan problem

A2.1 Freezing layer in the presence of particular heat generation

In our FD-implementation we use the square-root model of the frozen layer expansion $\delta = \delta(t)$ to estimate both the time evolution in the filled region and, optionally, the initial temperature profile at the flow front. These estimates are based upon the formulas in **Sec. 3.1.3**. In this **Appendix** we will describe two possible improvements of the temperature estimates. As it happens the first extension to a high extent captures the decreasing frozen layer thickness towards the inlet in a radial flow situation, unlike the standard square-root model (cf. [Carslaw & Jaeger], p.282). Here we extend the 1D Stefan problem of **Sec. 3.1.3**, by considering internal heat generation $Q(z, t)$ per unit volume and time, imitating local convection and dissipation. (The horizontal position x, y is fixed.) It is reasonable that the square-root behaviour of $\delta(t) := 2\varepsilon\sqrt{\kappa_s t}$ remains for a certain class of generation functions. The z -axis is here reversed, so that one-dimensional heat conduction is in the opposite z -direction, i.e. the wall surface corresponds to $z=0$ and the mould gap is the semi-infinite medium

$z > 0$. Let $c_3 := \sqrt{\frac{\kappa_s}{\kappa_\ell}}$, $y := \frac{z}{\sqrt{4\kappa_\ell t}}$, where phase region ℓ corresponds to $z > \delta(t)$, i.e. $y > c_3\varepsilon$.

In the solid region $0 < z < \delta(t)$, let the BC at the wall surface $z=0$ be $T_s(0, t) \equiv 0$.

In the liquid region the PDE is written

$$\frac{\partial^2 T_\ell}{\partial z^2} + \frac{\rho_s - \rho_\ell}{\rho_\ell \kappa_\ell} \cdot \delta'(t) \cdot \frac{\partial T_\ell}{\partial z} - \frac{1}{\kappa_\ell} \cdot \frac{\partial T_\ell}{\partial t} = -\frac{Q(z, t)}{\lambda_\ell}.$$

The 2nd term on the LHS corresponds to the convective term in PDE (3.11), with v_z according to

(3.10), where $\frac{\partial h}{\partial r} \approx 0$, $\tilde{U}(\tilde{z}) \approx \tilde{U}(1) = 1$ is assumed. As for the BCs at the layer surface $z = \delta(t)$ and at

$z \rightarrow \infty$, see [Carslaw & Jaeger], p.284. We make a separable-solution ansatz $D(y) \cdot g(t)$. For the

three PDE-terms on the LHS to have a common t -factor we must have $g'(t) = \alpha \cdot g(t)/t$,

i.e. $g(t) = \text{const} \cdot t^\alpha$, α arbitrary, and $Q(z, t) =: f(z/\sqrt{4\kappa_\ell t}) \cdot t^{\alpha-1}$. Let

$$T_\ell(z, t) =: U(z, t) + D\left(\frac{z}{\sqrt{4\kappa_\ell t}}\right) \cdot t^\alpha,$$

where U satisfies the corresponding homogeneous PDE in the liquid region and takes care of the BC at infinity, and $D(y)$ for $y \geq c_3\varepsilon$ solves the inhomogeneous ODE

$$D''(y) + 2(y + D_1)D'(y) - 4\alpha D(y) = -D_2 f(y), \quad D_1 := (c_2 - c_3)\varepsilon, \quad D_2 := \frac{4}{\rho_\ell c_{P,\ell}}.$$

In consideration of the time dependence of $T_\ell(z, t)$ upon t^α – there is one BC at infinity ($z \rightarrow \infty$) and two BCs at $z = \delta(t)$ to satisfy when t varies – $\alpha = 0$ is necessary for general f :s. This makes the ODE of 1st order and linear for $D'(y)$ – but restricts the class of generation functions to $f(y) \cdot t^{-1}$. For the assumed form $\delta(t)$, the temperature function U for some constant B ([ibid.], p.291) satisfies

$$U(z, t) =: T_I - D(\infty) - B \cdot \left[1 - \text{erf}\left(\frac{z}{\sqrt{4\kappa_\ell t}} + D_1\right) \right].$$

Since U for $\alpha = 0$ also solves the homogeneous ODE, D is taken as a particular solution determined by the initial values $D(c_3\varepsilon)$, $D'(c_3\varepsilon)$ (cf., e.g., [Birkhoff & Rota], p.41). A power series solution is easily obtained given a series expansion of f ([ibid.], p.99).

The BC corresponding to (3.7), determining the layer expansion parameter ε , becomes

$$\frac{\exp(-\varepsilon^2)}{\text{erf}(\varepsilon)} - \frac{c_1 \cdot [T_I - D(\infty) - T_M + D(c_3\varepsilon)]}{T_M - T_E} \cdot \frac{\exp(-(c_2\varepsilon)^2)}{1 - \text{erf}(c_2\varepsilon)} - \frac{c_1 \sqrt{\pi} D'(c_3\varepsilon)}{2(T_M - T_E)} = \frac{L_M \sqrt{\pi}}{c_{P,s}(T_M - T_E)} \varepsilon.$$

Here the excess melting temperature (above the zero wall temperature) is denoted $T_M - T_E$.

If, instead, the wall is modelled as a separate semi-infinite region ([ibid.], p.288), then, as in **Ch. 3** (cf. (3.8)), we obtain a correction by c_0 in the denominator of the first term of the ε -equation.

To illustrate the function class $f(y) \cdot t^{-1}$, we consider $f(y) = a \cdot (1 + 2D_1 y) e^{-y^2}$, $a > 0$, where Q takes its maximum at $z \approx D_1 \sqrt{4K_f t}$. For all functions in the class, the overall (integrated) heat generation in $\{(z, t) | z > \delta(t), 0 < t < t_{fill}\}$ becomes proportional to $\sqrt{t_{fill}}$. In the special case we get

$D(y) = a \cdot (D_2 / 2) e^{-y^2}$ as the additional temperature due to heat generation. This is illustrated in **Figure A2.1a-c**, for model (3.8) and its Q -extension. The relations between the a -values in **Fig. A2.1a-c** correspond to the viscous energy relations attributed to the different radial positions and their influence upon the average radial velocity and $\dot{\gamma}^{n+1}$. The time since activation is 2 s in **a** ($r = 0.3$ m), 3 s in **b** ($r = 0.2$ m) and 5 s in **c** ($r = 0.1$ m). In **Fig. A2.1a** we notice that already (3.8), i.e. $a = 0$, yields a shape similar to the FD simulated temperature profile, taken from **Fig. 4.9d**, but in **Fig. A2.1b-c**, which represent cavity parts far behind the front and behind the maximum frozen layer (cf. **Fig. 4.9c-b**), the Q -extended model provides better fit (especially in the frozen layer).

Figure A2.1a Run PC-cold: Analytical & FD. Vertical temp.profile & frozen layer at the end of filling, $r=0.3$ (m)

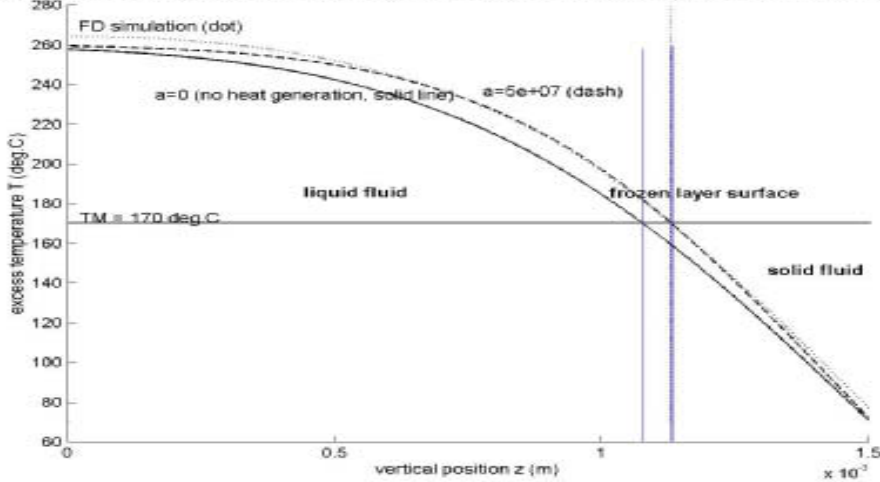


Figure A2.1b Run PC-cold: Analytical & FD. Vertical temp.profile & frozen layer at the end of filling, $r=0.2$ (m)

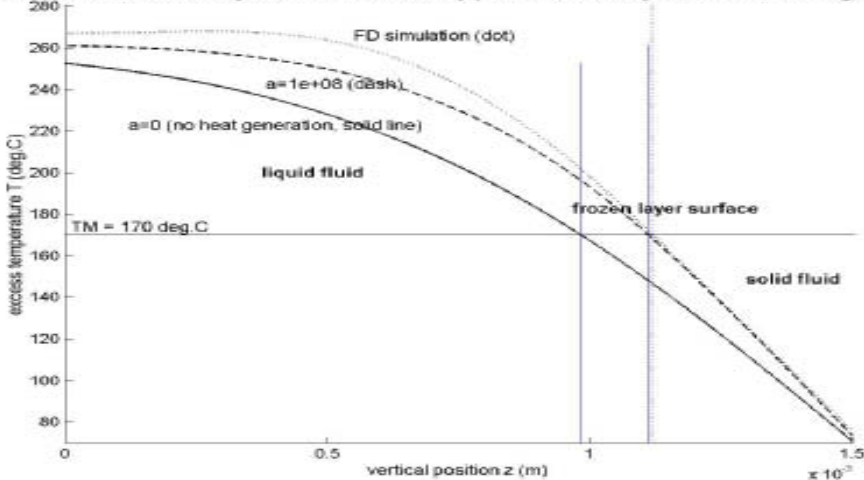
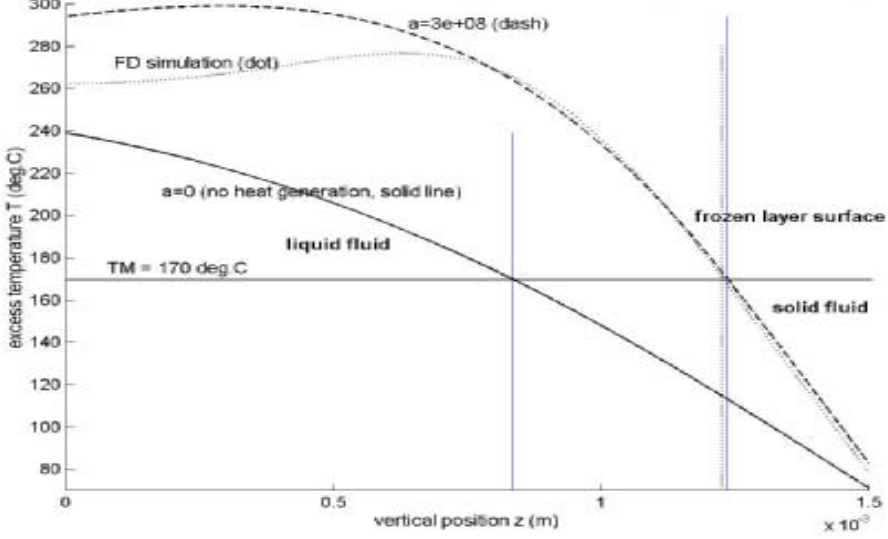


Figure A2.1c Run PC-cold: Analytical & FD. Vertical temp. profile & frozen layer at the end of filling, $r=0.1(\text{m})$



A2.2 Initial front temperatures by the square-root model

We saw in **Sec. 3.2.5** that the wall sine series converges slowly when the hot melt and the cold metal initially collide. This is not surprising, since the collision represents a singularity, with the initial heat flux tending to infinity. We also described how a stepwise linearization at the front, through a split time step, can cope with the fast initial change of heat flux. But the initial singularity remains. A possibility to get the flux and energy correct is to apply one of the square-root formulas in **Sec. 3.1.3** or **App. A2.1**. Since the front anyhow is subject to special handling, by fountain flow or front convection, it is natural to consider a simultaneous, square-root based conduction during an initial given time substep τ . We choose (3.8), since the approximation $L/2\sqrt{\kappa_w \tau} \gg 1$ is easily fulfilled in practice. The routine can be formulated as follows:

- Determine the stationary wall surface temperature T_{surf} in **Sec. 3.1.3** by solving (3.8) for ε .
- Determine the heat flux q_{surf} and the transferred heat energy E_{surf} (per m^2) between the metal and the solid melt:

$$q_{surf} = q_{surf} \cdot \sqrt{\frac{\lambda_w \rho_w c_{p,w}}{\pi \cdot \tau}}, \quad E_{surf} := \int_0^\tau q_{surf}(\tau') d\tau' = 2T_{surf} \cdot \sqrt{\frac{\lambda_w \rho_w c_{p,w} \cdot \tau}{\pi}}.$$

- Let q_{surf} replace the wall series solution at the end of the substep τ and correct the front temperatures close to the wall surface in such a way that E_{surf} is matched.
- Apply the usual wall series solution for the rest of the front time step $\Delta t_k - \tau$, starting from the analytical solution (describing excess temperatures above the cooling temperature T_E , see [Carslaw & Jaeger], p.288).

Let us consider the materials in **Ch. 4**. According to the square-root model the wall temperature is 1% of the difference $T_{surf} - T_E$ above T_E at the distance $z = 1.0 \text{ mm}$ from the wall surface after $\tau = 0.01 \text{ s}$, and at $z = 3.3 \text{ mm}$ after $\tau = 0.1 \text{ s}$, and the frozen layer expands to $\delta = 0.02 \text{ mm}$ and $\delta = 0.065 \text{ mm}$, respectively. In the liquid melt the temperature is 1% of the difference $T_l - T_M$ below T_l at the distances 0.1 mm and 0.3 mm , respectively, from the layer surface. These are the essentially affected mould and cavity parts that should be temperature corrected in an initial time substep at the front.

Appendix 3 Solid melt: a series solution

For both the active-flow set $A(t)$ and the passive-flow set $B(t)$, defined in **Sec. 3.2.1**, the heat balance of the frozen layer $z \in (h(\mathbf{r}, t), H]$ is controlled by one and the same conduction PDE. The interaction with the metallic mould (cavity wall) is two-way: the heat flux q_w through the wall surface is a result of the wall series solution in **Sec. 3.2.5**, and the surface temperature – to be determined here – is an input to the wall PDE. The frozen layer IBVP has BCs $T = T_M$ at $z = h(\mathbf{r}, t)$ and $\lambda_s \frac{\partial T}{\partial z} = q_w$ at $z = H$, and no IC, since the frozen region is an empty set at $t = 0$, and the local activation time t_{act} satisfies $h(\mathbf{r}, t_{act}(\mathbf{r})) = H$ for all cavity positions \mathbf{r} .

For semi-crystalline polymers with $\rho_s, c_{p,s}, \lambda_s$ approximately independent of temperature, the PDE becomes linear and a series solution exists. For all amorphous materials below T_G , the conductivity $\lambda_s = \lambda_0 + \lambda_1 \cdot T$ is nearly proportional to $c_{p,s} = c_0 + c_1 \cdot T$, i.e. $\alpha := \frac{\lambda_1}{\lambda_0} \approx \frac{c_1}{c_0} > 0$. In this case, use $U := T + \frac{\alpha}{2} \cdot T^2$, $\kappa := \frac{\lambda_0}{\rho c_0}$, to get the linear PDE $\frac{\partial U}{\partial t'} = \kappa \frac{\partial^2 U}{\partial z'^2}$. Thus U can be treated as T above, with corresponding IC and BCs. The solution U determines $T = \frac{2U}{1 + \sqrt{1 + 2\alpha U}}$.

Since the solution routine of the liquid phase in subregion $A(t)$ takes small time steps Δt_k , it is reasonable to assume an approximately linear evolution of the heat flux q_w during a time step. For a trial layer position $h(\mathbf{r}, t_k)$ it is now possible to determine both the solid melt and the wall solutions simultaneously, and deliver an estimated heat flux through $z = h$ as an output. The series solution is derived as in **Sec. 3.2.5**. Let $z' := z - h$, i.e. the wall surface is written $z' = H'$, $H' := H - h$, and use local time $t' := t - t_{k-1}$, where t_{k-1} , i.e. $t' = 0$, denotes the initial time of step k . The temperature profile $f(z')$ is given at $t' = 0$. See **Figure A3.1** for the interactions.

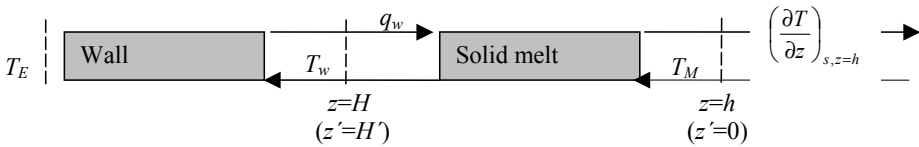


Figure A3.1 Input/output data at series solution of wall and solid melt PDEs. Fixed h , time step k .

Put $T = U + V$, where U takes care of the BCs and V handles the IC $T(z', 0) = f(z')$ of time step k . Let $\mu_n := \frac{(n + \frac{1}{2})\pi}{H'}$ and take

$$U(z', t') = T_M + \left(u_0 - \frac{u_1 H'^2}{2\kappa} \right) \cdot z' + u_1 z' t' + \frac{u_1 z'^3}{6\kappa},$$

$$V(z', t') = \sum_{n=0}^{\infty} V_n \cdot \sin(\mu_n z') \exp(-\kappa \mu_n^2 t'), \quad V_n := \frac{2}{H'} \cdot \int_0^{H'} [f(z') - U(z', 0)] \cdot \sin(\mu_n z') dz'.$$

If $f(z')$ has Fourier sine series expansion $f(z') = \sum_{n=0}^{\infty} f_n \cdot \sin(\mu_n z')$, then

$$V_n = f_n - \frac{2T_M}{\mu_n H'} - \frac{2(-1)^n u_0}{\mu_n^2 H'} + \frac{2(-1)^n u_1}{\mu_n^4 \kappa H'}.$$

At the wall surface

$$\begin{aligned} T(H', t') &= T_M + \left(u_0 - \frac{u_1 H'^2}{2\kappa} \right) \cdot H' + u_1 H' t' + \frac{u_1 H'^3}{6\kappa} + \sum_{n=0}^{\infty} V_n (-1)^n \exp(-\kappa \mu_n^2 t') \\ &= T_M \cdot \left[1 - \frac{2}{H'} \cdot \sum_{n=0}^{\infty} \frac{(-1)^n}{\mu_n} \exp(-\kappa \mu_n^2 t') \right] + u_0 \cdot \left(H' - \frac{2}{H'} \cdot \sum_{n=0}^{\infty} \frac{1}{\mu_n^2} \exp(-\kappa \mu_n^2 t') \right) \\ &\quad + \sum_{n=0}^{\infty} f_n (-1)^n \exp(-\kappa \mu_n^2 t') + u_1 \cdot \left[H' \cdot t' - \frac{H'^3}{3\kappa} + \frac{2}{\kappa H'} \cdot \sum_{n=0}^{\infty} \frac{1}{\mu_n^4} \exp(-\kappa \mu_n^2 t') \right] \\ &=: T_A + T_B \cdot u_1 \end{aligned}$$

Here $u_0 = \left(\frac{df}{dz'} \right)_{z'=H'}$ (given) and $t' = \Delta t_k$ is of our interest; thus T_A, T_B are fixed in time step k

(for given h). The $T(H', \Delta t_k)$ -expression is used as an input to the wall model in **Sec. 3.2.5**:

$$T_s(H', \Delta t_k) = T_A + T_B \cdot u_1 \equiv T_0 + T_1 \cdot \Delta t_k;$$

where $T_0 = f(H')$ (given) determines

$$T_1 = (T_A - T_0 + T_B \cdot u_1) / \Delta t_k.$$

In **Sec. 3.2.5** the heat flux through the wall surface is

$$\lambda_w \frac{\partial T_w}{\partial z'}(L, \Delta t_k) = \lambda_w \cdot (u_A + u_B \cdot T_1).$$

This expression is an input to the solid melt model as prescribed heat flux

$$\lambda_w \cdot (u_A + u_B \cdot T_1) \equiv \lambda_s \cdot (u_0 + u_1 \cdot \Delta t_k).$$

Once the fixed values $T_A, T_B, T_0, u_B, u_A, u_0$ are computed, the parameters T_1, u_1 become

$$\begin{aligned} u_1 &= \frac{(\lambda_w u_A - \lambda_s u_0) \Delta t_k + (T_A - T_0) \lambda_w u_B}{\lambda_s \Delta t_k^2 - \lambda_w T_B u_B}, \\ T_1 &= \frac{(\lambda_w u_A - \lambda_s u_0) T_B + (T_A - T_0) \lambda_s \Delta t_k}{\lambda_s \Delta t_k^2 - \lambda_w T_B u_B}. \end{aligned}$$

Now both the series solutions – of wall and solid melt – are determined. For the outer h -iteration, an estimated heat flux through h is needed. Let $\tau := \kappa \cdot \Delta t_k$ and compute

$$\begin{aligned} \frac{\partial T}{\partial z'}(0, \Delta t_k) &= u_0 - \frac{u_1 H'^2}{2\kappa} + u_1 \cdot \Delta t_k + \sum_{n=0}^{\infty} V_n \mu_n \exp(-\mu_n^2 \tau) \\ &= \sum_{n=0}^{\infty} f_n \mu_n \exp(-\mu_n^2 \tau) - \frac{2T_M}{H'} \cdot \sum_{n=0}^{\infty} \exp(-\mu_n^2 \tau) + u_0 \cdot \left[1 - \frac{2}{H'} \cdot \sum_{n=0}^{\infty} \frac{(-1)^n}{\mu_n} \exp(-\mu_n^2 \tau) \right] \\ &\quad + u_1 \cdot \left[\Delta t_k - \frac{H'^2}{2\kappa} + \frac{2}{\kappa H'} \cdot \sum_{n=0}^{\infty} \frac{(-1)^n}{\mu_n^3} \exp(-\mu_n^2 \tau) \right] \end{aligned}$$

Also for the liquid phase in the passive-flow region $B(t)$, a series solution is an alternative to the FD scheme, provided that the material parameters $\rho_\ell, c_{P,\ell}, \lambda_\ell$ are approximately constant.

Appendix 4 Comments on the PDE and its well-posedness

Well-posedness is an important concept when studying the existence, uniqueness and stability of solutions of PDEs. For nonlinear problems in general only local results are to be expected ([Gustafsson et al.], p.153). Often the nonlinear PDE and its solution can be considered as the limit of a sequence of linearized problems and their solutions ([ibid.], p.154); the linearized problems then ought to be well posed. We will consider (3.14) for a given surface evolution $h = h(\mathbf{r}, t) (> 0)$. (In reality h and T interact two-way.) Now $v_r, v_z, \dot{\gamma}$ depend only upon (\mathbf{x}, t) , but the non-linearity of the PDE through κ, η remains. The viscous-energy term $G := \eta \dot{\gamma}^2$ is linearized as $G = G_0 + c \cdot T$. Here the sign of the Arrhenius parameter B in the η -factor $e^{B/(T-T_B)}$ of (2.4) determines the sign of $c := \partial G / \partial T = -\frac{B}{(T-T_B)^2} \cdot G$, evaluated at a relevant temperature. For realistic materials models (and $G \uparrow \infty$ as $T \downarrow T_B$) $c < 0$ is to be expected.

Well-posedness is related to the properties of both the equation and the BCs. To study the former we will first treat an initial-value problem (IVP) for the homogeneous (without G_0), linearized PDE, PDEL, with an IC that is periodic in each dimension r, z , but has arbitrary periods (cf. [Straughan], p.4). If the domain is static and its boundary smooth, well-posedness of the PDEL is guaranteed by the well-posedness of the PDEL with frozen (constant) coefficients (e.g., [Strikwerda], p.235). By considering simple wave solutions of the frozen PDEL, introducing w_r, w_z as arbitrary real wave numbers, we identify the PDE symbol (i.e. its Fourier transform, [Gustafsson et al.], p.127)

$$\hat{P}(i\mathbf{w}) := -\kappa w_z^2 - i \cdot (v_r w_r + v_z w_z) + c.$$

Since \hat{P} and its complex conjugate \hat{P}^* for real materials fulfil

$$\hat{P} + \hat{P}^* = -2\kappa w_z^2 + 2c \leq 0,$$

any such homogeneous IVP is well-posed ([ibid.], p.129). By Duhamel's principle ([ibid.], p.149) also the (constant) inhomogeneous IVP is well-posed.

As for the influence of the BCs upon well-posedness, we will next study an idealization of the linearized IBVP (3.14) (cf. [ibid.], p.385, for 1D). We assume an expanding flow radius $R = R(t)$ and a 3D family of domains

$$X_t := \{(r \cos \varphi, r \sin \varphi, z) \mid r \in [\varepsilon, R(t)], \varphi \in [0, \varphi_{act}(t)], z \in [0, h(r, t)]\},$$

where $0 < \varepsilon < R(0)$. Let $U := T - T_M$, assume angularly independent solutions $U = U(r, z, t)$ and, as a description of the temperature levelling fountain flow at the front, take $\partial U / \partial z = 0$ as BC at $r = R(t)$. The IC in $(r, z) \in [\varepsilon, R(0)] \times [0, H]$ is $U \equiv T_I - T_M$. This is also the BC at $r = \varepsilon$, $z \in [0, H]$. For fixed t , $z = h(r, t)$ is assumed to vary slowly with r and, since $v_r \equiv 0$ at h , the normal component fulfils $v_\perp \approx v_z$. Assume smooth, real coefficients $\kappa, v_r, v_z, c : \kappa(r, z, t) > 0$, $v_r(r, z, t) > 0$ for $z \in [0, h(r, t))$, $v_z(r, 0, t) = 0$ and $c(r, z, t) < 0$. Consider the PDE written as

$$\frac{\partial U}{\partial t} = PU + G_0, \quad P := \frac{\partial}{\partial z} \left(\kappa \frac{\partial}{\partial z} \right) - v_r \frac{\partial}{\partial r} - v_z \frac{\partial}{\partial z} + c,$$

and define the energy $E(t) := \frac{1}{2} \|U(\cdot, \cdot, t)\|^2 := \frac{1}{2} \int_{X_t} |U|^2 d\mathbf{x}$ (cf. [Straughan], p.4). Multiply the

homogeneous PDE by U and integrate. Integration by parts, identification of the front expansion rate $R'(t) = \bar{v}_r(R(t), t)$, and use of Gauss' theorem and the no-divergence condition yields

$$\begin{aligned}
\frac{dE}{dt} &= \frac{d}{dt} \left(\frac{1}{2} \int_{X_t} |U|^2 d\mathbf{x} \right) = \int_{X_t} U \frac{\partial U}{\partial t} d\mathbf{x} + \left[\frac{1}{2} \int_{z=0}^{h(r,t)} \int_{\varphi=0}^{\varphi_{act}(t)} |U|^2 r d\varphi dz \right]_{r=R(t)} \cdot R'(t) = \\
&= \int_{X_t} U \cdot P U d\mathbf{x} + \frac{1}{2} R(t) \varphi_{act}(t) \cdot \left[\int_{z=0}^{h(r,t)} U^2 dz \cdot \bar{v}_r(r,t) \right]_{r=R(t)} = \\
&= - \left\| \sqrt{\kappa} \frac{\partial U}{\partial z} \right\|^2 - \left\| \sqrt{|c|} U \right\|^2 + \varphi_{act}(t) \cdot \int_{r=\varepsilon}^{R(t)} \left[\kappa U \frac{\partial U}{\partial z} - \frac{1}{2} v_z U^2 \right]_{z=0}^{h(r,t)} r dr \\
&\quad + \frac{1}{2} R(t) \varphi_{act}(t) \cdot U^2(R(t), t) \cdot \left[\int_{z=0}^{h(r,t)} (\bar{v}_r(r,t) - v_r(r, z, t)) dz \right]_{r=R(t)} + \frac{1}{2} \varepsilon \varphi_{act}(t) \cdot \left[\int_{z=0}^{h(\varepsilon, t)} v_r U^2 dz \right]_{r=\varepsilon}
\end{aligned}$$

In the final expression, the first two terms are bounded above by some $\frac{1}{2} \alpha \|U\|^2 = \alpha E(t)$, $\alpha < 0$, where $\alpha < 0$ is used if κ or c is uniformly bounded below (and a Wirtinger type inequality, cf. [Straughan], p.207, is applied). The 1st integral (for r) vanishes, due to BCs, $U = 0$ at $z = h$ and $v_z \equiv 0$ plus $\partial U / \partial z = 0$ at $z = 0$. By the definition of the average $\bar{v}_r(r, t)$, the 2nd integral (for z) evaluates to 0. The 3rd integral (for z) takes the positive value $\frac{1}{2} \varepsilon \varphi_{act}(t) h(\varepsilon, t) \bar{v}_r(\varepsilon, t) (T_I - T_M)^2$ and since $(T_I - T_M)^2$ is the temperature dependent factor of $E(0)$ the integral value is of type $\beta(t)E(0)$; with β independent of U . Hence the energy fulfils

$$\frac{dE}{dt} \leq \alpha E(t) + \beta(t)E(0), \quad E(t) \leq E(0) \cdot \left[e^{\alpha t} + \int_0^t \beta(\tau) d\tau \right].$$

In terms of [Gustafsson et al.], p.383, the homogeneous linearized IBVP is strongly well posed, and P is maximally semi-bounded. As the source term G_0 is smooth, Duhamel's principle applies and the well-posedness can be extended to the inhomogeneous linearized problem.

Finally we will argue that the IBVP for the nonlinear PDE is locally well posed. We therefore consider a given solution T_0 and local variations $T = T_0 + u$. The viscous energy term is rewritten

$$G(T, \mathbf{x}, t) \approx G(T_0, \mathbf{x}, t) + c(T_0, \mathbf{x}, t) \cdot u,$$

a 1st order Taylor expansion at T_0 . Now $u \equiv 0$ (i.e. T_0) solves the corresponding inhomogeneous PDEL as well, and the remaining equation coincides with $\frac{\partial u}{\partial t} = Pu$ above. Any initial value perturbation $u(r, z, 0) = u_0(r, z)$ can be evaluated as above, by the energy method, but now all BCs are homogeneous. Therefore the $\beta(t)E(0)$ -term disappears and only the $\alpha E(t)$ -term remains. If α is assumed negative in a fixed time interval, then we will have local nonlinear stability of the basic solution T_0 (cf. [Straughan], p.9).

A global well-posedness of the general problem (3.11) would require that h is allowed to vary by T – cf. **Section 3.2.3** – to satisfy (3.13). No such well-posedness can exist, since we know from practice that close to a total freezing situation $h \downarrow 0$, the imposed $v_r, \dot{\gamma}$ and η (through $\dot{\gamma}$ and pressure) have no a priori bounds.

Appendix 5 Stability of linearized FD scheme

Linear schemes with constant coefficients, obtained by freezing the coefficients in a variable coefficient scheme in every possible way, can be used to prove stability of general linearized schemes in simplified geometries ([Strikwerda], p.51, and [Gustafsson et al.], p.183). Initially we look at a frozen-coefficient formulation. Let r -index i be exchanged for m to clarify the intended Fourier transformation, i.e. von Neumann analysis (e.g., [Smith], p.67, and [Strikwerda], p.40). We make a transformation to the uniform ζ -grid (cf. **Sec. 3.3.1**), and consider the transformed PDEL, the linearization of PDE (3.12), where we assume v_z and κ constant, $\partial(rv_r)/\partial r \approx 0$ (reasonable in radial flow situations), and (cf. **App. 4**) $\eta\dot{\gamma}^2 \approx g_0 + g_1 U$:

$$\frac{\partial U}{\partial t} + v_r \frac{\partial U}{\partial r} + v_z \frac{\partial U}{\partial \zeta} \zeta'(z) = \kappa \left(\zeta''(z) \frac{\partial U}{\partial \zeta} + [\zeta'(z)]^2 \frac{\partial^2 U}{\partial \zeta^2} \right) + (g_0 + g_1 U).$$

Here we assume periodic FD-solutions (U_{mj}^k) , from initial values (U_{mj}^0) on a grid of, say, $M+1$ equidistant r -levels $r_m = m \cdot \Delta r$ and $J+1$ equidistant ζ -levels $\zeta_j = j \cdot \Delta \zeta$:

$$U_{mj}^0 = \sum_{n_1=0}^M \sum_{n_2=0}^J A_{n_1 n_2} e^{in_1 \pi \frac{m}{M} + in_2 \pi \frac{j}{J}} = \sum_{n_1=0}^M \sum_{n_2=0}^J A_{n_1 n_2} e^{i w_{n_1} r_m + i w_{n_2} \zeta_j} \quad m = 0, \dots, M \quad j = 0, \dots, J$$

where $w_{n_1} := \frac{n_1 \pi}{M \Delta r}$, $w_{n_2} := \frac{n_2 \pi}{J \Delta \zeta}$.

These initial value equations determine the complex coefficients $(A_{n_1 n_2})$ uniquely. By linearity it is sufficient to study the propagation of some initial wave $U_{mj}^0 = e^{i(w_1 r_m + w_2 \zeta_j)}$ from initial time $t_0 = 0$, with constant growth rate α , to $U_{mj}^k = e^{i(w_1 r_m + w_2 \zeta_j)} \cdot e^{\alpha t_k}$ at time t_k . In the corresponding FD equation (cf. (3.16) for the untransformed nonlinear case), let

$$a_N := \frac{\Delta t_k}{\Delta \zeta} \left[\kappa \cdot \left(\frac{[\zeta''(z)]^2}{\Delta \zeta} + \frac{\zeta''(z)}{2} \right) - v_z \frac{\zeta'(z)}{2} \right],$$

$$a_S := \frac{\Delta t_k}{\Delta \zeta} \left[\kappa \cdot \left(\frac{[\zeta''(z)]^2}{\Delta \zeta} - \frac{\zeta''(z)}{2} \right) + v_z \frac{\zeta'(z)}{2} \right], \quad b_1 := \frac{\Delta t_k v_r}{\Delta r}, \quad c := \Delta t_k g_1.$$

Here we assume $a_N, a_S > 0$, i.e. the conduction term exceeds the vertical convection term. This is a restriction upon the grid density $\Delta \zeta$, and can always be accomplished since (see **Sec. 3.3.1**) $\zeta''(z) \downarrow 1/(H \cdot \ln B \cdot \beta) > 0$ (and $\zeta''(z) \downarrow 0$) as $z \downarrow 0$. Moreover, $v_r > 0$, i.e. $b_1 > 0$, and $c < 0$ (cf. **App.4**). Substitution into the FD equation, neglecting the inhomogeneous viscous energy term g_0 , yields

$$e^{\alpha \Delta t_k} = [1 - c + b_1 \cdot (1 - e^{-i w_1 \Delta r}) + a_N \cdot (1 - e^{i w_2 \Delta \zeta}) + a_S \cdot (1 - e^{-i w_2 \Delta \zeta})]^{-1}.$$

This is the amplification factor, usually denoted by g , $g(w_1, w_2) := e^{\alpha \Delta t_k}$. In order to investigate the stability condition $|g(w_1, w_2)| \leq 1$ ([Strikwerda], p.42), we look for the minimum value of the g -denominator. We may consider the last three terms of the denominator as the sum of a fixed point $(b_1 + a_N + a_S, 0)$ and, as w_1, w_2 vary, three rotating vectors in the complex plane. The smallest denominator magnitude, $1 - c$, is attained at $w_1 = w_2 = 0$, i.e.

$|g(w_1, w_2)| \leq g(0, 0) = 1/(1 - c)$, and since $c < 0$ the FD-scheme is unconditionally stable.

From now on, we will consider the non-frozen FD-scheme. In order to linearize the FD-equation (3.16), replace the diffusivity coefficients and the viscous energy term by local values – simply marked by the exclusion of their upper (time step) index k in (3.16).

We consider the corresponding homogeneous scheme, which means ignoring the source term g_0 . Moreover, we consider the FD-equation as matrix-valued, each entry corresponding to one node (i, j) of radial level i and vertical level j , for fixed k . Introduce the operator symbols \mathbf{I} (identity op.) and \mathbf{Q} . As we will see below, the linearized equation has the form (backward Euler)

$$[\mathbf{I} - \Delta t_k \mathbf{Q}] \mathbf{U}^k = \mathbf{U}^{k-1}, \quad \mathbf{U}^k \in \mathbf{C}^{(M+1) \times (J+1)}.$$

According to [Gustafsson et al.], p.186, backward Euler schemes are unconditionally stable, if \mathbf{Q} is semi-bounded, i.e. fulfils

$$\operatorname{Re} \langle \mathbf{V}, \mathbf{QV} \rangle \leq \alpha \|\mathbf{V}\|^2 \quad \text{for all } \mathbf{V} \in \mathbf{C}^{(M+1) \times (J+1)}.$$

Here $\langle \mathbf{A}, \mathbf{B} \rangle$ is any inner product for the matrices \mathbf{A}, \mathbf{B} such that $\|\mathbf{A}\| := \sqrt{\langle \mathbf{A}, \mathbf{A} \rangle}$ is an operator norm. However, [ibid.] implicitly assume $\Delta t_k < 1/\alpha$ in their stability proof.

Since (cf. **Sec. 3.3.1**) control volume (i, j) has measure $\mu_V = \varphi_{act}(t) \cdot r_i \Delta r \Delta z_j$, we introduce the weight matrices $\mathbf{E}_x = \operatorname{diag}(\mathbf{e}_x)$ for $\mathbf{x} \equiv \mathbf{r}, \mathbf{z}$, with positive diagonal elements $e_{r,i} := \sqrt{\varphi_{act}(t) \cdot r_i \Delta r}$, $e_{z,j} := \sqrt{\Delta z_j}$, and (cf. **Sec. 2.3.1**) define inner products and norms on a fixed (r_i, z_j) -grid in $(r, z) \in [\varepsilon, R] \times [0, H]$ as (c denotes complex conjugate):

$$\begin{aligned} \langle \mathbf{A}, \mathbf{B} \rangle_{\mathbf{r}\mathbf{z}} &:= \operatorname{tr}[(\mathbf{E}_r \mathbf{A} \mathbf{E}_z)^* (\mathbf{E}_r \mathbf{B} \mathbf{E}_z)] = \sum_i \sum_j A_{ij}^c B_{ij} |e_{r,i}|^2 |e_{z,j}|^2, \quad \|\mathbf{A}\|_{\mathbf{r}\mathbf{z}}^2 = \langle \mathbf{A}, \mathbf{A} \rangle_{\mathbf{r}\mathbf{z}}, \\ \langle \mathbf{a}, \mathbf{b} \rangle_{\mathbf{x}} &:= \operatorname{tr}[(\mathbf{E}_x \mathbf{a})^* (\mathbf{E}_x \mathbf{b})] = \sum_m a_m^c b_m |e_{x,m}|^2, \quad (\mathbf{x}, m) \equiv (\mathbf{r}, i), (\mathbf{z}, j), \quad \mathbf{a} = (a_m), \mathbf{b} = (b_m), \end{aligned}$$

i.e. the 2D and the 1D row and column norms are related by (cf. [ibid.], p.487)

$$\langle \mathbf{A}, \mathbf{B} \rangle_{\mathbf{r}\mathbf{z}} = \sum_i \langle \mathbf{a}_{i\bullet}, \mathbf{b}_{i\bullet} \rangle_{\mathbf{z}} |e_{r,i}|^2 = \sum_j \langle \mathbf{a}_{\bullet j}, \mathbf{b}_{\bullet j} \rangle_{\mathbf{r}} |e_{z,j}|^2.$$

In order to treat the dynamic BCs at the frozen surface $z = h(r, t) \leq H$ and at the front $r = k \cdot \Delta r \leq R$, we define $U_{ij}^k := 0$ outside the liquid part of subregion $A(t)$. At the front we either start from $U_{kj}^{k-1} = 0$ and derive U_{kj}^k by radial marching from $U_{k-1,j}^{k-1}$ or we use a special (unspecified) form of \mathbf{Q} , subject to the same semi-bound α , to derive U_{kj}^{k-1} from $U_{k-1,j}^{k-1}$ (with $U_{kj}^{k-2} = 0$).

To show stability of the linearized FD-scheme (3.16) we follow [Gustafsson et al.], p.182, and describe the scheme using linear 1D difference operators \mathbf{D}_+ (forward), \mathbf{D}_0 (central) and \mathbf{D}_- (backward), for the set of nodes \mathbf{O} in **Fig. 3.2**, at (r_i, z_j) , and for $(\mathbf{x}, m) \equiv (\mathbf{r}, i), (\mathbf{z}, j)$ written

$$(\mathbf{D}_{0\mathbf{xO}} \mathbf{a})_m := \frac{a_{m+1} - a_{m-1}}{x_{m+1} - x_{m-1}}, \quad (\mathbf{D}_{+\mathbf{xO}} \mathbf{a})_m := \frac{a_{m+1} - a_m}{x_{m+1} - x_m}, \quad (\mathbf{D}_{-\mathbf{xO}} \mathbf{a})_m := \frac{a_m - a_{m-1}}{x_m - x_{m-1}}.$$

By use of the Hadamard product \circ , $(\mathbf{A} \circ \mathbf{B})_{ij} := A_{ij} B_{ij}$, the linearization of scheme (3.16) in time step k at node \mathbf{O} can be written

$$\begin{aligned} [\mathbf{I} - \Delta t_k \cdot \mathbf{Q}] \mathbf{U}^k &= \mathbf{U}^{k-1} + \Delta t_k \cdot \mathbf{G}_0, \quad \mathbf{Q} := \mathbf{Q}_r + \mathbf{Q}_z + \mathbf{G}_1, \quad G_{n,ij} := g_n(r_i, z_j, t_k), \quad n \equiv 1, 2, \\ \mathbf{Q}_r \mathbf{U} &:= -\mathbf{F}_r \mathbf{D}_{-r\mathbf{O}} (\mathbf{W}_r \circ \mathbf{U}), \quad W_{r,ij} := r_i v_r(r_i, z_j, t_k), \quad \mathbf{F}_r := \operatorname{diag}((1/r_i)_i), \\ \mathbf{Q}_z \mathbf{U} &:= -\mathbf{D}_{0z\mathbf{O}} (\mathbf{W}_z \circ \mathbf{U}) + \mathbf{D}_{-zn} \mathbf{K} \mathbf{D}_{+z\mathbf{O}} \mathbf{U}, \quad W_{z,ij} := v_z(r_i, z_j, t_k) \quad K_{ij} := \kappa(r_i, z_{j+1/2}, t_k). \end{aligned}$$

Consider the homogeneous – backward Euler – scheme. Stability is guaranteed if \mathbf{Q} is semi-bounded. Since the operators $\mathbf{Q}_r, \mathbf{Q}_z$ are essentially 1D, \mathbf{Q}_r for fixed j of type $\mathbf{AD}_{-x0}(\mathbf{Bu})$ with $\mathbf{A} := \mathbf{diag}(\mathbf{a}), \mathbf{B} := \mathbf{diag}(\mathbf{b})$ depending on the space variable (general notation \mathbf{x}), we will initially derive a general result for such operators. Consider an \mathbf{E}_x -weighted 1D grid inner product, assume \mathbf{a}, \mathbf{b} real, $\mathbf{a} \geq \mathbf{0}, \mathbf{b} > \mathbf{0}$ and let

$$\mathbf{F}_x = \mathbf{diag}(\mathbf{f}_x), \quad f_{x,m} := \sqrt{\frac{a_m \Delta x_m}{b_m}}, \quad \delta_m := \left(\frac{a_{m+1} b_m}{b_{m+1}} \frac{|e_{x,m+1}|^2}{\Delta x_{m+1}} - a_m \frac{|e_{x,m}|^2}{\Delta x_m} \right) b_m.$$

By using $2 \operatorname{Re} \langle \mathbf{V}, \mathbf{QW} \rangle = \langle \mathbf{V}, \mathbf{QW} \rangle + \langle \mathbf{QW}, \mathbf{V} \rangle$ we derive (cf. [Gustafsson et al.], p.446):

$$\begin{aligned} & \langle \mathbf{AD}_{-x0}(\mathbf{Bv}), \mathbf{w} \rangle_\ell^u + \langle \mathbf{v}, \mathbf{AD}_{-x0}(\mathbf{Bw}) \rangle_\ell^u = \\ & = \sum_{m=\ell}^u \frac{|e_{x,m}|^2}{\Delta x_m} a_m (b_m v_m - b_{m-1} v_{m-1})^c w_m + \sum_{m=\ell}^u \frac{|e_{x,m}|^2}{\Delta x_m} v_m^c a_m (b_m w_m - b_{m-1} w_{m-1}) = \\ & = \langle \mathbf{F}_x \mathbf{D}_{-x0}(\mathbf{Bv}), \mathbf{F}_x \mathbf{D}_{-x0}(\mathbf{Bw}) \rangle_\ell^u - \sum_{m=\ell}^u \delta_m v_m^c w_m + \frac{a_{m+1} b_m^2}{b_{m+1}} \frac{|e_{x,m+1}|^2}{\Delta x_{m+1}} v_m^c w_m \Big|_{\ell-1}^u \end{aligned} \quad (\text{A5.1})$$

Analogously, with $\delta'_m := \left(\frac{a_{m-1} b_m}{b_{m-1}} \frac{|e_{x,m-1}|^2}{\Delta x_{m-1}} - a_m \frac{|e_{x,m}|^2}{\Delta x_m} \right) b_m$, we obtain

$$\begin{aligned} & \langle \mathbf{AD}_{+x0}(\mathbf{Bv}), \mathbf{w} \rangle_\ell^u + \langle \mathbf{v}, \mathbf{AD}_{+x0}(\mathbf{Bw}) \rangle_\ell^u = \\ & = \sum_{m=\ell}^u \frac{|e_{x,m}|^2}{\Delta x_m} a_m (b_{m+1} v_{m+1} - b_m v_m)^c w_m + \sum_{m=\ell}^u \frac{|e_{x,m}|^2}{\Delta x_m} v_m^c a_m (b_{m+1} w_{m+1} - b_m w_m) = \\ & = -\langle \mathbf{F}_x \mathbf{D}_{+x0}(\mathbf{Bv}), \mathbf{F}_x \mathbf{D}_{+x0}(\mathbf{Bw}) \rangle_\ell^u + \sum_{m=\ell}^u \delta'_m v_m^c w_m + \frac{a_{m-1} b_m^2}{b_{m-1}} \frac{|e_{x,m-1}|^2}{\Delta x_{m-1}} v_m^c w_m \Big|_\ell^{u+1} \end{aligned} \quad (\text{A5.2})$$

To allow $\mathbf{b} \geq \mathbf{0}$ in (A5.1) we need an alternative. Let

$$\mathbf{F}_x'' = \mathbf{diag}(\mathbf{f}_x''), \quad f_{x,m}'' := \sqrt{a_m b_{m-1} \Delta x_m}, \quad \delta_m'' := a_{m+1} b_m \frac{|e_{x,m+1}|^2}{\Delta x_{m+1}} - a_m (b_{m-1} - 2b_m) \frac{|e_{x,m}|^2}{\Delta x_m}.$$

The wanted result is

$$\begin{aligned} & \langle \mathbf{AD}_{-x0}(\mathbf{Bv}), \mathbf{w} \rangle_\ell^u + \langle \mathbf{v}, \mathbf{AD}_{-x0}(\mathbf{Bw}) \rangle_\ell^u = \\ & = \langle \mathbf{F}_x'' \mathbf{D}_{-x0} \mathbf{v}, \mathbf{F}_x'' \mathbf{D}_{-x0} \mathbf{w} \rangle_\ell^u - \sum_{m=\ell}^u \delta_m'' v_m^c w_m + a_{m+1} b_m \frac{|e_{x,m+1}|^2}{\Delta x_{m+1}} v_m^c w_m \Big|_{\ell-1}^u \end{aligned} \quad (\text{A5.3})$$

We will now investigate whether \mathbf{Q}_r is semi-bounded (for fixed $z = z_j$, implicit below). Since $\bar{v}_r(r, t)$ is generated by a finite radial inflow rate at each time t , and $r \geq \varepsilon (> 0)$ is assumed, $r \bar{v}_r$ is approximately constant so it is reasonable to assume that the radial velocity $v_r(r, t)$ is non-negative and fulfils a Lipschitz-type condition

$$|r_1 v_r(r_1, t) - r_2 v_r(r_2, t)| \leq A_1(t) \cdot \max[r_1, r_2] \cdot |r_1 - r_2|.$$

Consider the domain $r \in [r_0, R]$, $r_0 := \varepsilon$, with BC $U(r_0, t) = g_r(t)$ and IC $U(r, 0) = f(r)$. In time step k we use the active grid $r_i = r_0 + i \cdot \Delta r$, $i = 0, 1, \dots, k''$, where $k'' = k$ or $k + 1$, $k'' \leq K$,

$R = K \cdot \Delta r$. Due to the BC at $r = r_0$, every FD-solution U must have $U_0(t) = g_r(t)$ at r_0 ; which

can be excluded from the grid norm. Using (A5.3) with $\mathbf{A} := \mathbf{F}_r$, $\mathbf{B} := \text{diag}(W_{r,\bullet})$ and $\mathbf{u} := (\mathbf{U})_\bullet$, we get

$$\begin{aligned} 2 \text{Re} \langle \mathbf{u}, \mathbf{Q}_r \mathbf{u} \rangle_1^K &= 2 \text{Re} \langle \mathbf{u}, \mathbf{Q}_r \mathbf{u} \rangle_1^{k''} = \\ &= - \left[\left\| \mathbf{F}_r^* \mathbf{D}_{-r0} (\mathbf{B} \mathbf{u}) \right\|_1^{k''} \right]^2 - \sum_{i=1}^{k''} \delta_i'' |u_i|^2 + \varphi_{act}(t) r_k v_{r,k''} |u_{k''}|^2 - \varphi_{act}(t) r_0 v_{r,0} |g_r(t)|^2 \\ &\leq A_1(t) \cdot \left\| \mathbf{u} \right\|_1^{k''} + \varphi_{act}(t) r_0 v_{r,0} |g_r(t)|^2 \leq A_1(t) \cdot \left\| \mathbf{u} \right\|_1^K + \varphi_{act}(t) r_0 v_{r,0} |g_r(t)|^2. \end{aligned}$$

The semi-boundedness of \mathbf{Q}_r can be deduced from a homogeneous BC instead of the more general BC $U_0 = g_r$, by the variable transformation

$$\tilde{U}(r, t) := U(r, t) - g_r(t) \cdot \frac{k'' \cdot \Delta r - r}{k'' \cdot \Delta r - r_0};$$

which also has an influence upon IC

$$\tilde{f}(r) := \tilde{U}(r, 0) = f(r) - g_r(0) \cdot \frac{k'' \cdot \Delta r - r}{k'' \cdot \Delta r - r_0}$$

and upon the generation term of the corresponding inhomogeneous PDE. Now \mathbf{Q}_r is semi-bounded with a bound $\alpha = \alpha_r$, if there exists an upper bound $\alpha_r := \frac{1}{2} \cdot \sup_{t \in [0, t_{fill}]} A_r(t)$, i.e. similar to a uniform Lipschitz condition for the whole filling process. This condition is reasonable – however impossible to fulfil for any case that develops to complete freezing ($v_r \uparrow \infty$ in a narrow cavity gap), when the solution procedure should collapse as well.

Next consider \mathbf{Q}_z . Let $a_{N,j} := \frac{1}{2} \left(\frac{\kappa_{j+1/2}}{n_j} - v_{z,j+1} \right)$, $a_{S,j} := \frac{1}{2} \left(\frac{\kappa_{j-1/2}}{|s_j|} + v_{z,j-1} \right)$ and assume that

conduction predominates over vertical convection in the sense that $a_N, a_S \geq \varepsilon_a(t) > 0$ (cf. **Sec. 3.3.2**). Moreover, assume that the vertical velocity fulfils a Lipschitz condition ($r = r_i$ is fixed)

$|v_z(z_1, t) - v_z(z_2, t)| \leq A_2(t) \cdot |z_1 - z_2|$. Consider the domain $z \in [0, h]$ with BCs $\frac{\partial T}{\partial z}(0, t) = 0$,

$T(h, t) = g_z(t) (= T_M)$ and IC $T(z, 0) = f(z)$. Assume that $z = h(r_i, t)$ corresponds to z_{jh} , with

$jh \leq J$, $H = z_j$. By using the variable transformation $\tilde{U}(z, t) := U(z, t) - g_z(t) \cdot z/h$ we get a

homogeneous BC at z_{jh} , not affecting the semi-boundedness of \mathbf{Q}_z . Let $\mathbf{u} := (\tilde{\mathbf{U}})_\bullet$, with

$\tilde{U}_j(t) = 0$ for $j \geq jh$, and use the active grid norm $(z_j)_{j=0}^{jh-1}$. To derive a semi-bound, let

$\mathbf{K}_z := \text{diag}(K_{i,\bullet})$, $\mathbf{V}_z := \text{diag}(W_{z,\bullet})$, use $|e_{z,j}|^2 / \Delta z_j = 1$, $\Delta z_j = n_j + |s_j|$ and consider

$$\begin{aligned} 2 \text{Re} \langle \mathbf{u}, \mathbf{Q}_z \mathbf{u} \rangle &= -2 \text{Re} \langle \mathbf{u}, \mathbf{D}_{0z0} \mathbf{V}_z \mathbf{u} \rangle + 2 \text{Re} \langle \mathbf{u}, \mathbf{D}_{-zn} \mathbf{K}_z \mathbf{D}_{+z0} \mathbf{u} \rangle = \\ &= 2 \text{Re} \sum_j u_j^c \left[\frac{1}{2} (-v_{z,j+1} u_{j+1} + v_{z,j-1} u_{j-1}) + \kappa_{j+1/2} \frac{u_{j+1} - u_j}{2n_j} - \kappa_{j-1/2} \frac{u_j - u_{j-1}}{2|s_j|} \right] = \\ &= 2 \cdot \sum_j \text{Re} \left(u_j^c [a_{N,j} (u_{j+1} - u_j)] \right) - 2 \cdot \sum_j \text{Re} \left(u_j^c [a_{S,j} (u_j - u_{j-1})] \right) - \sum_j (v_{z,j+1} - v_{z,j-1}) |u_j|^2. \end{aligned}$$

Identification of the first two terms in the final expression with the middle-expressions in (A5.2) and (A5.1), for $\mathbf{b} \equiv \mathbf{1}$, $\mathbf{v} = \mathbf{w} \equiv \mathbf{u}$, $\mathbf{a} \equiv \mathbf{a}_N$ and $\mathbf{a} \equiv \mathbf{a}_S$, respectively, yields

$$\begin{aligned}
2 \operatorname{Re} \langle \mathbf{u}, \mathbf{Q}_z \mathbf{u} \rangle_0^{J-1} &= 2 \operatorname{Re} \langle \mathbf{u}, \mathbf{Q}_z \mathbf{u} \rangle_0^{jh-1} = - \left(\left\| \mathbf{F}_x \mathbf{D}_{+zO} \mathbf{u} \right\|_0^{jh-1} \right)^2 - \left(\left\| \mathbf{F}_x \mathbf{D}_{-zO} \mathbf{u} \right\|_0^{jh-1} \right)^2 \\
&+ \sum_{j=0}^{jh-1} \left(\delta_j + \delta'_j - v_{z,j+1} + v_{z,j-1} \right) |u_j|^2 + a_{N,j-1} |u_j|^2 \Big|_0^{jh} - a_{S,j+1} |u_j|^2 \Big|_{-1}^{jh-1} = \\
&= - \left(\left\| \mathbf{F}_x \mathbf{D}_{+zO} \mathbf{u} \right\|_0^{jh-1} \right)^2 - \left(\left\| \mathbf{F}_x \mathbf{D}_{-zO} \mathbf{u} \right\|_0^{jh-1} \right)^2 - \frac{1}{2} \sum_{j=0}^{jh-1} \left(v_{z,j+1} - v_{z,j-1} \right) |u_j|^2 \\
&- a_{N,-1}(t) |U_0(t)|^2 - a_{S,jh}(t) |U_{jh-1}(t)|^2 + a_{S,0}(t) |U_{-1}(t)|^2. \tag{A5.4}
\end{aligned}$$

In the final expression (A5.4) positive contributions come from the last term in each of the two lines. The very last term can be bounded by a Sobolev inequality (e.g., [Gustafsson et al.], p.459): for every $\varepsilon = \varepsilon(t)$, $\varepsilon > 0$, we have

$$|U_{-1}(t)|^2 = |U_1(t)|^2 \leq \max_{j=0,1,\dots,jh-1} |U_j(t)|^2 \leq \varepsilon \cdot \left(\left\| \mathbf{D}_{-zO} \mathbf{u} \right\|_1^{jh-1} \right)^2 + (h^{-1} + \varepsilon^{-1}) \cdot \left(\left\| \mathbf{u} \right\|_0^{jh-1} \right)^2.$$

(A somewhat weaker bound is obtained if $\left\| \mathbf{D}_{+zO} \mathbf{u} \right\|$ is considered as well.) The grid density – cf.

Fig. 3.2 – fulfils $2n_j \leq \Delta z_j \leq 2|s_j|$. To accomplish semi-boundedness, we choose $\varepsilon > 0$ such

that $a_{S,0}(t) \cdot \varepsilon \cdot \left(\left\| \mathbf{D}_{-zO} \mathbf{u} \right\|_0^{jh-1} \right)^2 \leq \left(\left\| \mathbf{F}_x \mathbf{D}_{-zO} \mathbf{u} \right\|_0^{jh-1} \right)^2$, where $\left\| \mathbf{D}_{-zO} \mathbf{u} \right\|_0^{jh-1} \geq \left\| \mathbf{D}_{-zO} \mathbf{u} \right\|_1^{jh-1}$ and

$$\left(\left\| \mathbf{F}_x \mathbf{D}_{-zO} \mathbf{u} \right\|_0^{jh-1} \right)^2 \geq \varepsilon_a(t) \cdot 2|s_{jh-1}| \cdot \left(\left\| \mathbf{D}_{-zO} \mathbf{u} \right\|_0^{jh-1} \right)^2.$$

As for the last term in the first line of the final expression (A5.4), the Lipschitz condition implies

$$|v_{z,j+1} - v_{z,j-1}| \leq A_z(t) \cdot |z_{j+1} - z_{j-1}| = A_z(t) \cdot 2\Delta z_j,$$

$$2 \operatorname{Re} \langle \mathbf{u}, \mathbf{Q}_z \mathbf{u} \rangle_0^{J-1} \leq (A_z(t) + h^{-1} + \varepsilon^{-1}(t)) \cdot \left(\left\| \mathbf{u} \right\|_0^{jh-1} \right)^2 \leq (A_z(t) + h^{-1} + \varepsilon^{-1}(t)) \cdot \left(\left\| \mathbf{u} \right\|_0^{J-1} \right)^2.$$

Thus \mathbf{Q}_z is semi-bounded, if there exists an upper bound

$$\alpha_z := \frac{1}{2} \cdot \sup_{t \in [0, t_{full}]} (A_z(t) + h^{-1} + \varepsilon^{-1}(t)),$$

i.e. if the Lipschitz condition and the lower bounds of a_N, a_S are uniform for the filling process.

The last term of \mathbf{Q}, \mathbf{G}_1 , comes from the local temperature derivative of the viscous energy term (cf. **App. 4**), uniformly bounded, $|g_1| \leq A_g$, for $T \geq T_M (> T_B)$.

Now also the 2D operator $\mathbf{Q} = \mathbf{Q}_r + \mathbf{Q}_z + \mathbf{G}_1$ is semi-bounded ([Gustafsson et al.], p.485), and the stability of the linearized FD-scheme follows.